HIGH ENERGY PHOSPHATE METABOLISM MEASUREMENT BY PHOSPHORUS-31 MAGNETIC RESONANCE FINGERPRINTING

by

CHARLIE YI WANG

Submitted in partial fulfillment of the requirements

For the degree of Doctor of Philosophy

Department of Biomedical Engineering

CASE WESTERN RESERVE UNIVERSITY

Dissertation Adviser: Dr. Xin Yu

January, 2018

CASE WESTERN RESERVE UNIVERSITY SCHOOL OF GRADUATE STUDIES

We hereby approve the thesis/dissertation of

Charlie Y. Wang

candidate for the degree of Doctor of Philosophy*.

Committee Chair

Dominique Durand

Committee Member

Chris Flask

Committee Member

Mark A. Griswold

Committee Member

Charles Hoppel

Committee Member

Nicole Seiberlich

Committee Member

Xin Yu

Date of Defense

June 15, 2017

*We also certify that written approval has been obtained for any proprietary material contained therein.

Table of Contents

List of Tables

List of Figures

High Energy Phosphate Metabolism Measurement by Phosphorus-31 Magnetic Resonance Fingerprinting

Abstract

by

CHARLIE YI WANG

Adenosine Triphosphate (ATP) serves as the universal currency of energy in cellular systems. Hydrolysis of ATP thermodynamically drives the majority of cellular processes fundamental to life. The existence of a fast and robust method to observe ATP and its reactions *in vivo* would have profound applications both in the clinical diagnosis of metabolic abnormalities, and in the evaluation of therapies. Phosphorus-31 (^{31}P) spectroscopy is the only modality capable of non-invasive non-destructive *in vivo* detection of ATP and its reactions. However, ^{31}P spectroscopy methods are often challenging to perform due to two reasons. First, the instruments have an inherently low sensitivity to the biological signal. Second, conventional ^{31}P spectroscopy methods have emphasized mathematical tractability rather than optimal signal detection. Consequently, ^{31}P spectroscopy methods require long experiment times, and this has precluded their use in many applications. In this thesis, a new acquisition paradigm, the Magnetic Resonance Fingerprinting (MRF) framework, was applied to ^{31}P spectroscopy method design in order to shorten experiment times. By prioritizing signal detection over

mathematical tractability, the methods designed in this thesis sought to overcome the limitations imposed by instrument sensitivity and shorten experiment times. Success in this goal may enable new applications.

Three main projects are described in this thesis. First, the MRF framework based ^{31}P-MRF method was used to obtain efficient and simultaneous quantification of T_1 relaxation time and concentration of multiple metabolites. This method was tested in simulation and validated *ex-vivo*. Second, sensitivity to magnetization transfer (MT) effects between phosphocreatine (PCr) and ATP was added to the ^{31}P-MRF method to measure the *in vivo* chemical exchange rate of creatine kinase enzyme. This new method, the CK-MRF method, was assessed *in vivo* rat hindlimb. Finally, the ^{31}P-MRF method was further adapted to additionally incorporate measurements of ATP synthesis and hydrolysis. This third method, the MT-MRF method, was assessed in both simulation and *in vivo* experiments.

Chapter 1. Introduction

Every energetically unfavorable metabolic process necessary for life must be thermodynamically driven. In mammals, this is primarily done using the energy released from the cleavage of the high energy phosphate bond within adenosine triphosphate (ATP). The ATP consumed through this process must also be resynthesized from the metabolite products of this cleavage: adenosine diphosphate (ADP) and inorganic phosphate (P_i). In human cells, the rate of ATP utilization far surpasses the total ATP content stored; in order to supply ATP on demand, the ATP resynthesization rate must be closely coupled to the utilization rate. The balance between ATP utilization and resynthesis occupies a central role in metabolism, and underpins ATP's function as life's intermediary "currency of energy." The importance and ubiquity of ATP metabolism in human physiology underlies an extensive need for reliable ways to study it.

Magnetic resonance spectroscopy (MRS) is a valuable tool to study metabolism *in vivo*. Indeed, it is the only such tool that is non-invasive, non-ionizing, and non-destructive. MRS is also uniquely sensitive and versatile in its ability to directly observe and distinguish metabolites in living tissues. This combination of safety and versatility is responsible for an extensive body of scientific knowledge and clinical potential that has emerged from MRS studies over the decades.

Different MRS sensitive nuclei have different applications. *In vivo* carbon-13 (^{13}C) MRS has been used to track the metabolism of labeled pyruvate and lactate substrates, with many applications in cancer diagnosis, cancer grading, and therapy monitoring[1]. *In vivo* oxygen-17 (^{17}O) MRS has been used to measure oxygen consumption rates during cellular respiration[2]. Indeed, countless applications from these nuclei and others, including proton (^{1}H), sodium (^{23}Na) and fluorine (^{19}F) have been put forth. However, this thesis will focus on the use of phosphorus-31 (^{31}P) MRS for the direct detection of the phosphates associated with high energy metabolites. Through the direct detection of these metabolites and their interconversion rates, ^{31}P MRS can noninvasively detect ATP synthesis and utilization *in vivo*.

A general and straightforward process to measure metabolic rates using ^{31}P MRS has been recognized for decades. Typically, three steps, leveraging the phenomena of magnetization transfer (MT) that accompanies all chemical exchange processes, are repeated to perform phosphate metabolism measurements by conventional ^{31}P MRS methods. First, a magnetic tag is applied to a phosphorus containing moiety within the substrate metabolite of interest. Most commonly, this will be the γ phosphate group of ATP. Next, a waiting period is performed to allow the chemical reactions of metabolism to occur. As these reactions occur, the tagged phosphate moieties are transferred from the substrate to the product metabolite. Finally, using a “pulse-and-acquire” MR methodology, the amount of tag accumulated in the product metabolite is measured. By

comparing the amount of tag accumulated against the waiting time allowed, the rate of the tag's accumulation within the product metabolite, proportional to the chemical exchange rate between metabolites, can be assessed. ^{31}P MRS methods, using this process, are used to measure the metabolic conversion rates between phosphocreatine (PCr) with ATP, mediated through the creatine kinase enzymes, and inorganic phosphate (P_i) with ATP, mediated through various ATPase enzymes. A substantial body of scientific work has resulted from the successful applications of MT based ^{31}P MRS (MT-MRS) methods to measure these processes.

However, many applications utilizing ^{31}P MT-MRS methods have proven to be challenging. First and foremost, all MR methods are inherently low in sensitivity; they require at least millimolar (mM) range concentrations of detectable nuclei in order to generate signals that are discernable from hardware noise. This sensitivity limit is several orders of magnitude worse than other imaging modalities such as PET, which is capable of detecting tracers with micromolar (μM) concentration. Rapid and reliable clinical MR imaging (MRI) is possible because of the high concentration of signal generating ^{1}H nuclei *in vivo* (~110 molar). Unfortunately with the typical *in vivo* concentration of ATP at ~10 mM, ^{31}P signals from ATP are near the detection limit of MR. Thus, all ^{31}P MRS measurements of ATP signals incur a degree of uncertainty due to hardware noise.

Several approaches currently exist to reduce the uncertainty, or the measurement robustness, of ^{31}P MRS methods. The pulse-and-acquire MR methodology used to obtain these measurements have many adjustable experimental parameters that may impact measurement certainty. However after decades of clinical and research practice, it is unlikely that additional tuning of these parameters will achieve substantial improvements to measurement robustness. Another approach is to simply repeat the measurements multiple times and statistically average the results to generate a single, more robust, measurement. This approach establishes a tradeoff between measurement reliability and the required experimental time, but can only be used within the limits of the available experiment time. Other approaches, such as increased sophistication of detector hardware, or increased system magnetic field strength, can also improve measurement certainty, but require substantial financial investment and resources. Generally, ^{31}P measurements, using the pulse-and-acquire methodology, must overcome MR detection limitations, as determined by the available experiment time and financial resources, to generate reliable and meaningful measurements.

Due to time or resource constraints, many potential applications find current ^{31}P MT-MRS methods impractical or unreliable, despite the ubiquity and importance of ATP metabolism. Thus there is need to establish a new methodology that may improve the reliability of ^{31}P MRS measurements within available experiment time and resources.

Overview of Thesis

The work presented in this thesis seeks to adapt a novel methodology, the Magnetic Resonance Fingerprinting (MRF) framework, to ^{31}P MRS. **By leveraging the flexibility of the MRF framework, we hypothesized that novel ^{31}P MRF methods could be designed to surpass that limitations of existing pulse-and-acquire based methods, leading to faster and more reliable measurements of metabolism.** Since the MRF framework adopts the same existing MR hardware and underlying physics to perform measurements, the measurements obtained using any developed MRF methods should theoretically agree with measurements obtained using conventional ^{31}P MRS methods within the same experiment. However, the increased reliability of measurements obtained using the MRF framework should lead to increased measurement reproducibility given equal experiment time as conventional methods, or decreased experiment time for an equivalent measurement reproducibility.

First, a brief review is presented on the theory of ^{31}P MRS, existing MT-MRS methods to measure metabolism, and the MRF framework, in Chapter 2. **We hypothesized that an MRF approach would be able to accurately and more efficiently measure both T_1 relaxation time and relative concentration of multiple ^{31}P metabolites, in the absence of active metabolism, compared to conventional methods.** To this end, a novel method, the ^{31}P-MRF method, was developed within the MRF framework. This method was assessed for both measurement agreement and increased measurement reproducibility per unit

acquisition time against conventional ^{31}P MRS methods *in vitro*. The designed method, and the experiments to assess its performance, are presented in Chapter 3. After that, the ^{31}P-MRF method was adapted to measure the rate of creatine kinase enzyme mediated ATP metabolism. **We hypothesized that this approach would lead to accurate and more time efficient measurements of CK metabolism as compared to conventional methods.** This method, the CK-MRF method, is presented in Chapter 4. It was assessed for measurement agreement against conventional ^{31}P MRS methods in rat skeletal muscle under both resting baseline and post ischemia/reperfusion conditions. It was also assessed for increased measurement reproducibility *in vivo* during stable physiological conditions as compared to conventional ^{31}P MRS methods. Finally, the ^{31}P-MRF method was expanded to also measure ATPase mediated metabolism of ATP. **We hypothesized that this would enable accurate and more efficient quantification of tissue properties related to ATPase mediated metabolism.** This method, the MT-MRF method, is presented in Chapter 5. It was assessed for accuracy and reproducibility of measurements for ATPase mediated metabolism against conventional ^{31}P MRS methods in both simulation and in resting rat skeletal muscle. *In vivo* accuracy was assessed in all using paired t-tests for equivalent mean of measurements, and Bland-Altman analysis for limits of agreement. *In vivo* reproducibility was assessed through comparisons of measurement variability.

Chapter 2. Background

In this chapter, the background and theory of the concepts described in Chapter 1 are discussed in greater detail.

Theory of MR Spectroscopy

The fundamental basis for MR spectroscopy is the interaction of nuclei with external magnetic fields. These nuclei can be conceptualized as a spinning electrical charge, with an orientation in space. When placed within an external magnetic field, the orientation of these nuclei will attempt to align with the external field. While doing so, they will precess about the axis of the external field with an angular frequency, ω_0, known as the Larmor frequency, given by:

$$\omega_0 = \gamma B_0 \qquad [2.1]$$

where B_0 is the strength of the external magnetic field, and γ is the proportionality constant known as the gyromagnetic ratio, which is specific for each nuclei. Typically, the primary external magnetic field in an MR spectroscopy experiment is generated by a large magnet, engineered for high field strength and homogeneity, which the subject of interest is placed within. Nuclei within the subject will precess with a frequency ω_0 due to the external magnetic field. As they precess, the field generated by these nuclei will also vary through time. Through Faraday's law of induction, the net sum of these fields across nuclei, or

the bulk magnetization, can be strong enough to induce a voltage signal within detectors placed near the subject.

However, in additional to this primary field, each nuclei will also be affected by the local secondary magnetic fields associated with nearby electrons. These secondary fields will act to shield or deshield nuclei from the primary field, causing nuclei to be affected by a slightly lower or higher B_0 than the main field. These variations of effective B_0 translate into variations in ω_0 of precession the subsequent signal detected. The ω_0 of a nuclei in the presence of sheilding can be expressed as:

$$\omega_0 = \gamma B_0(1 - \sigma) \qquad [2.2]$$

where σ is the shielding constant that arises from the local environment surrounded the nuclei. σ is typically on the order of 10^{-6}, and expressed in parts per million (ppm). When the shielding constant of different nuclei is sufficiently unique, signals from these nuclei can be distinguished by their unique Larmor frequencies. For ^{31}P MRS, the phosphorus nuclei associated with the phosphate groups of phosphocreatine (PCr), inorganic phosphate (P_i), and the three phosphate moieties of ATP each have a distinct local environment, resulting in unique σ and corresponding ω_0 values for each phosphate moiety. As a result, all five of these moieties generate a signal that can be distinguished from the others.

Assuming a sample, containing only a single metabolite, and thus a single σ, is placed in a primary external field with strength B_0, the bulk magnetization from this sample will be the sum of the magnetic moments of all the nuclei in the sample. This bulk magnetization can be modeled as a single magnetization vector in reference to the direction of the B_0 field. The behavior of this magnetization vector will be described by the Bloch equation:

$$\frac{d\vec{M}}{dt} = \gamma\vec{M} \times \left(\vec{B}_{ext}(1-\sigma)\right) + \frac{1}{T_1}(M_0 - M_z)\hat{z} - \frac{1}{T_2}\vec{M}_\perp \qquad [2.3]$$

Here, $\vec{M}$ is the bulk magnetization from all nuclei in the sample. $\vec{B}_{ext}$ is the net external magnetic field. M_0 represents the maximum net magnetization of the sample. $\hat{z}$ and M_z are, respectively, the unit vector aligned with the primary field, B_0, and the longitudinal magnetization component of $\vec{M}$ aligned with B_0 (i.e. $M_z = \vec{M}\hat{z}$). $\vec{M}_\perp$is the transverse component of $\vec{M}$ that is orthogonal to B_0, also known as the transverse magnetization. T_1 and T_2 are time constants that describe, respectively, the rate of magnetization regrowth towards M_0 and the rate of magnetization decay of $\vec{M}_\perp$. Typically, an arbitrary reference axis, orthogonal to $\hat{z}$ and defined by $\hat{x}$ and $\hat{y}$, is selected to decompose $\vec{M}_\perp$ such that $\vec{M}_\perp = \vec{M}\hat{x} + \vec{M}\hat{y}$. From this, $\vec{M}\hat{x}$ and $\vec{M}\hat{y}$ can be expressed as M_x and M_y, respectively. In the case of a static external field, such that $\vec{B}_{ext}$ = B_0, the Bloch equation can be simplified. Decomposing $\vec{M}$ into orthogonal components M_x, M_y, and M_z, such that $\vec{M} = M_x\hat{x} + M_y\hat{y} + M_z\hat{z}$, and substituting in Equation 2.2, the Bloch equation can be expressed as:

$$\frac{dM_z}{dt} = \frac{M_0 - M_z}{T_1} \quad [2.4]$$

$$\frac{dM_x}{dt} = \omega_0 M_y - \frac{M_x}{T_2} \quad [2.5]$$

$$\frac{dM_z}{dt} = -\omega_0 M_x - \frac{M_y}{T_2} \quad [2.6]$$

Faraday's law dictates that in nearby conductive coils, voltage signals will be induced with a strength proportional to $\frac{d\vec{M}}{dt}$. Since $\omega_0 \gg \frac{1}{T_2}, \frac{1}{T_2}$, it can be seen from Equations 2.4-6 that only $\frac{dM_x}{dt}$ and $\frac{dM_y}{dt}$ will contribute measurably to signal generation. In other words, given a bulk magnetization $\vec{M}$ within a static external field, only the transverse magnetization component will generate signal. Furthermore, the steady state solution, given at time $t = \infty$ for Equations 2.4-6, can be derived as $M_z = M_0$, $M_x = M_y = 0$. This implies that after enough time, transverse magnetization, $\vec{M}_\perp$, or the detectable MR signal, always decays to zero, while M_z eventually regrows to M_0. When this occurs, the magnetization, M_z, must be 'tipped' back into the $\vec{M}_\perp$ before signal may again be detected. This 'tipping' process is performed by applying time varied $\vec{B}_{ext}$ fields, through the use of radiofrequency (RF) pulses. The details of this process are beyond the scope of this background. However, these RF pulses are ideally assumed to be capable of rotating $\vec{M}$ by any desired amount and in any desired direction.

With this background, a simple MR experiment can be described. Assuming a sample initially in the equilibrium, $\vec{M} = M_0$, state, an appropriate RF pulse,

designed to rotate $\vec{M}$ by 90° about $\hat{y}$, will 'tip' $\vec{M}$ completely into the tranverse plane and aligned along $\hat{x}$ ($\vec{M} = M_x$). The resulting nonzero $\vec{M}_\perp$ will induce a time dependent voltage in nearby coils that will fluctuate with a frequency, ω_0, until $\vec{M}_\perp$ decays to zero. If additional measurements are required, for instance because the signal voltage was not sufficiently discernable above hardware noise, then the experiment can be repeated. However, waiting time must be allotted for $\vec{M}$ to regrow towards M_0.

The description thus far, based on the Bloch equation, can be extended to multiple metabolites, each with their own σ value. Doing so will model the bulk magnetization, $\vec{M}$, from each metabolite separately. The composite bulk magnetization detected will be the sum of $\vec{M}$ across all metabolites.

Applying the previously outlined MR experiment to a sample with multiple metabolites, each with their own chemical shifts $\sigma = \sigma^1, \sigma^2, \ldots \sigma^n$, will similarly generate signal voltage. However, this voltage will now fluctuate with multiple frequency components: $\omega_0^1 = \gamma B_0(1-\sigma^1)$, $\omega_0^2 = \gamma B_0(1-\sigma^2)$, $\ldots$ $\omega_0^n = \gamma B_0(1-\sigma^n)$. Applying the Fourier Transform to this signal will generate a frequency spectrum with peaks at the frequencies corresponding to $\omega_0^1, \omega_0^2, \ldots \omega_0^n$. The area of each peak will be proportional to the concentration of the corresponding metabolite. This, combined with *a priori* knowledge of the σ corresponding to each

metabolite, allows MR spectroscopy to specifically detect, identify, and quantity different metabolites in vivo.

In Vivo ^{31}P MRS Measurement of Metabolism

An example ^{31}P spectra acquired from *in vivo* rat leg is shown in Figure 2.1. The different spectral peaks that can be discerned are associated with the phosphorus containing moieties of phosphocreatine (σ^{PCr} = 0 ppm), the γ phosphate group of ATP ($\sigma^{\gamma ATP}$=-2.4 ppm), the α phosphate group of ATP ($\sigma^{\alpha ATP}$=-8 ppm), the β phosphate group of ATP ($\sigma^{\beta ATP}$=-16 ppm), and inorganic phosphate (σ^{Pi} = 4.8 ppm). The relative concentrations of these metabolites can be determined from the area of each spectral peak. As a result, ^{31}P MRS can noninvasively characterize the metabolic profile of high energy phosphates in a vast array of pathologies. Formidable insight of *in vivo* metabolism, particularly in skeletal muscle[3] and heart[4,5] has been gained merely by measuring these concentrations.

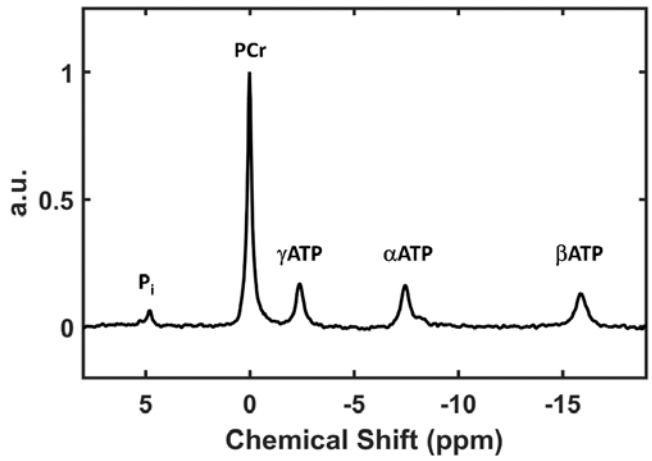

Figure 2.1. Example 31P spectra. An example ^{31}P Spectra acquired from *in vivo* rat leg. Spectral peaks, corresponding to inorganic phosphate (P_i), phosphocreatine (PCr), and the three phosphate moieties of ATP, (γATP, αATP, βATP) are labeled.

The theory of ^{31}P MRS signals provided thus far has been restricted from the chemical reactions involving these ^{31}P metabolites. Incorporation of these reactions within the MR theory requires a brief background on the nature of these reactions. Broadly, these reactions can be categorized broadly by their function: ATP utilization, ATP synthesis, and ATP buffering (and transport). Figure 2.2 shows the major reactions and the enzyme catalyzing them within muscle myocytes. Utilization is shown on the right side, where ATP is hydrolyzed by muscle myosin to drive downstream reactions related to muscle contraction. The end products of ATP hydrolysis, ADP and the cleaved inorganic P_i, are transported to the inner mitochondrial membrane. Here, the reactions of oxidative

phosphorylation occur for ATP synthesis, through the ATP synthase enzyme. This re-synthesized ATP can then be transported out of the mitochondria to regenerate the depleted ATP. ATP depletion will also be buffered by phosphocreatine, allowing the ATP supply to meet rapid fluctuations in demand. This buffering is performed by the isoforms of the creatine kinase enzyme. Many other reactions were omitted for simplicity, but also contribute significantly to ATP synthesis and ATP utilization. Examples of these include anaerobic glycolysis in the cytoplasm and Na^+/K^+ ATPase in the plasma membrane.

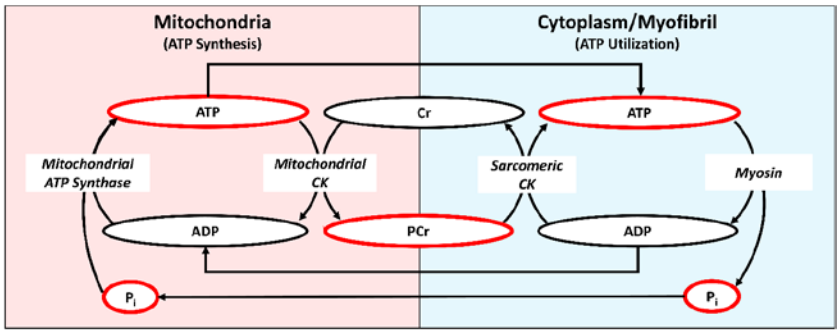

Figure 2.2. High energy phosphate metabolism in skeletal muscle. Simplified model of the site, enzymes and substrates of the major ATP reactions in skeletal muscle. The metabolites with observable ^{31}P signals, corresponding to spectral peaks shown in Figure 2.1, are highlighted in red.

^{31}P MRS can only directly detect the metabolites outlined in red in Figure 2.2. Furthermore, metabolite σ is largely insensitive to the different physical compartments. As a result, signals from the same metabolite but originating from

different cellular compartments cannot be distinguished using ^{31}P MRS. The compartment model describing ^{31}P signals can therefore be further simplified to:

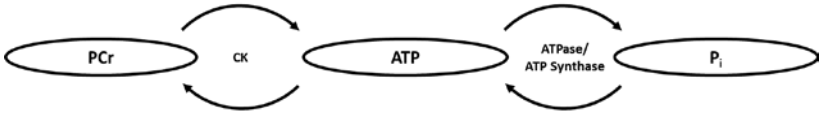

Figure 2.3. Simplified compartment model of exchange assumed during ^{31}P MRS

Absent from Figure 2.3 are creatine and ADP components because creatine lacks a phosphorus nuclei, and ADP concentration is too low to be directly discerned. Based off this simplified three pool model, the following equations of mass balance can be derived:

$$\frac{dPCr}{dt} = -k_f^{CK} PCr + k_r^{CK} ATP \quad [2.7]$$

$$\frac{dATP}{dt} = k_f^{CK} PCr + k_f^{ATP} Pi - (k_r^{CK} + k_r^{ATP}) ATP \quad [2.8]$$

$$\frac{dPi}{dt} = -k_f^{ATP} Pi + k_r^{ATP} ATP \quad [2.9]$$

Here, k_f^{CK} and k_r^{CK} are the PCr-to-ATP and ATP-to-PCr rate constant of creatine kinase, respectively. k_f^{ATP} and k_r^{ATP} are the rate constants of ATP synthase and ATPase, respectively. The effects of these reactions on the ^{31}P MRS signal can be predicted by combining these equations with the previously described Bloch equations:

$$\frac{d\vec{M}^{PCr}}{dt} = \gamma\, \vec{M}^{PCr} \times \left(\vec{B}_{ext}(1 - \sigma^{PCr})\right) + \frac{1}{T_1}(M_0^{PCr} - M_z^{PCr})\hat{z} - \frac{1}{T_2}\vec{M}_{\perp}^{PCr} - k_f^{CK}\, \vec{M}^{PCr} + k_r^{CK}\, \vec{M}^{\gamma ATP} \quad [2.10]$$

$$\frac{d\vec{M}^{\gamma ATP}}{dt} = \gamma\, \vec{M}^{\gamma ATP} \times \left(\vec{B}_{ext}(1-\sigma^{\gamma ATP})\right) + \frac{1}{T_1}\left(M_0^{\gamma ATP} - M_z^{\gamma ATP}\right)\hat{z} - \frac{1}{T_2}\vec{M}_{\perp}^{\gamma ATP} + k_f^{CK}\, \vec{M}^{PCr} + k_f^{\gamma ATP}\, \vec{M}^{Pi} - (k_r^{CK} + k_r^{ATP})\, \vec{M}^{\gamma ATP} \quad [2.11]$$

$$\frac{d\vec{M}^{Pi}}{dt} = \gamma\, \vec{M}^{Pi} \times \left(\vec{B}_{ext}(1-\sigma^{Pi}+\right) + \frac{1}{T_1}\left(M_0^{Pi} - M_z^{Pi}\right)\hat{z} - \frac{1}{T_2}\vec{M}_{\perp}^{Pi} - k_f^{ATP}\, \vec{M}^{Pi} + k_r^{ATP}\, \vec{M}^{\gamma \mathrm{ATP}} \quad [2.12]$$

Here, magnetization vectors $\vec{M}^{PCr}$, $\vec{M}^{\gamma ATP}$, and $\vec{M}^{Pi}$ refer to the bulk magnetization vectors originating from the phosphorus nuclei of PCr, γATP, and P_i, respectively. Knowledge of all time constants, concentrations, and enzyme rates allows for a complete description of magnetization evolution and the signal generated under any theoretical conditions.

Of course, this is the reverse paradigm faced during the typical ^{31}P MRS experiment. The goal of generating signals in ^{31}P MRS detect a signal capable of estimating the unknown tissue properties related to the tissue time constants, metabolite concentrations, and enzyme reaction rates. In order to do this, MR methods are designed with acquisition parameters that force the MR signal to evolve in a useful manner according to simplified signal models. These models, typically derived from the Bloch-McConnell equations, can then be used to perform parameter estimation, and therefore quantification of metabolism rates.

Metabolism Measurement by Magnetization Transfer encoded MRS

The most common method to quantify metabolism rates, particularly the CK rate constant, is the magnetization transfer method (MT-MRS). MT-MRS uses a long duration frequency selective RF pulse to "tag" ATP magnetization. The specific tag used in this case seeks to force $\vec{M}^{\gamma ATP}$ to zero. This choice is appealing because in doing so, the magnetizations, $\vec{M}^{PCr}$, $\vec{M}^{\gamma ATP}$, and $\vec{M}^{Pi}$, are mathematically decoupled. A solution for the expected signal, S(*t*), generated from $\vec{M}^{PCr}$ after a known duration of tagging, *t*, can be derived from Equation 2.10 that will be proportional to:

$$S(t) \cong \kappa M_0^{PCr}\left(1 - e^{\frac{-t}{\kappa T_1^{PCr}}}\right) + M_0^{PCr} e^{\frac{-t}{\kappa T_1^{PCr}}},\ \kappa = \frac{1}{1+k_f^{CK} T_1^{PCr}} \qquad [2.13]$$

Here, time $t = 0$ is the time at which tagging was initiated. Notably, this signal now only depends on the three tissue properties k_f^{CK}, T_1^{PCr}, and M_0^{PCr}. Figure 2.4 shows example *in vivo* data that corresponds to Equation 2.13 from a typical MT-MRS experiment.

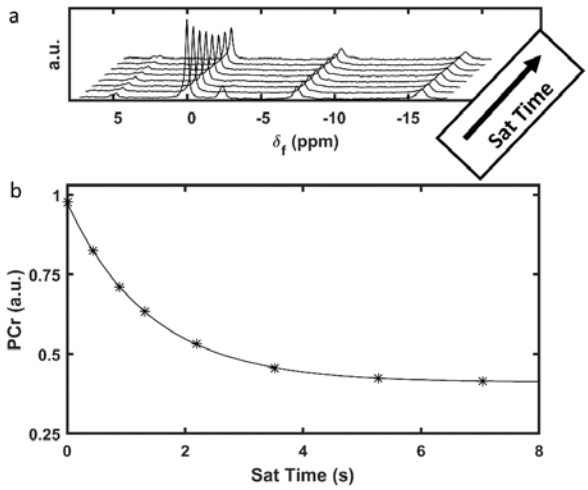

Figure 2.4. Example data and quantification of an MT-MRS Experiment. Multiple spectra (a) are acquired under conditions of variable saturation time. Signal (stars) plotted against saturation time (b), than can be fit against signal model (solid line) to estimate tissue parameters.

Figure 2.4a shows a stack of ^{31}P MRS spectra stacked in order of increasing saturation times, *t*. The first spectra, with *t* = 0, has no selective γATP saturation applied, similar to a conventional ^{31}P spectra. The subsequent spectra, which are tagged by the selective RF saturation pulse, lack signal from γATP. As the time duration of this tag is increased, a decrease of PCr signal can be observed. Plotting the PCr signal as a function of saturation (tagging) time, shown in Figure 2.4b, shows that the PCr signal will generate a monoexponential signal shape, as predicted by Equation 2.13. Given sufficient measurements of $S(t)$, using different durations of t, curve fitting of the PCr signal to the equation, shown overlaid, can be performed to estimate the three unknown tissue property constants, M_0^{PCr}, T_1^{PCr},

and k_f^{CK} of Equation 2.13. Indeed, the limited number in unknown tissue properties, as well as the simple exponential form for the signal model, of Equation 2.13 is extremely attractive compared to the direct use of Equations 2.10-2.12. Additionally, M_0^{Pi}, T_1^{Pi}, and k_f^{ATP} can theoretically be determined from the same experiment and process using the P_i signal. This, theoretically, allows for ATPase/ATP synthase reaction rates to be quantified using the same acquired dataset.

However, several assumptions were required to derive the signal model of Equation 2.13 from the Bloch-McConnell equations (Equations 2.10-12). This constrains the pulse sequence acquisition choices that can be used. These assumptions include: $S(t) \cong M_z^{PCr}(t)$, $\vec{B}_{ext}(t) = B_0$, $k_f^{CK} M_0^{PCr} = k_r^{CK} M_0^{\gamma\mathrm{ATP}}$, $M_z^{ATP}(t) = 0$, and $M_z^{PCr}(0) = M_0^{PCr}$. Of these, the assumption $M_z^{PCr}(0) = M_0^{PCr}$ requires long waiting periods between consecutive measurements that are on the order of ~4x T_1^{PCr}. Combined with the low inherent sensitivity of MR, which often forces several repeated measurements of $S(t)$ to obtain reliable results, the MT-MRS method is a time intensive experiment.

This lengthy time requirement of the MT-MRS method leaves room for innovation to develop alternative approaches for enzyme rate quantification. For any MR method to be useful, the method must fulfill three criteria: 1) it must generate sufficient signal, 2) its signal must be uniquely related to the tissue properties of

interest, and 3) there must be a way to extract the value of the properties of interest from the signal measured. MT-MRS's long history of use is due to the robustness with which it addresses the second criteria, and the simplicity with which it addresses the third criteria. However, the MT-MRS does not optimally address the first criteria; its lengthy waiting periods limit the rate of signal generation. Alternative methods to MT-MRS have been proposed over the years with varying degrees of success. Unfortunately these methods, sharing the pulse-and-acquire signal acquisition paradigm, struggle to sufficiently address all three criteria. Thus a new method, developed within a fundamentally different signal acquisition paradigm, should be investigated.

The Magnetic Resonance Fingerprinting Framework

The Magnetic Resonance Fingerprinting (MRF) framework is an innovative paradigm for MR experiment and method design. Fundamentally, the MRF framework allows for greater flexibility in MR experiment design by providing a general template for extracting tissue property values from any MR signal, regardless of the complexity of the signal model. By removing the restrictions on the underlying signal model, the full Bloch equation can be used rather than any restricted intermediate signal model. As such, acquisition parameter choices can be made to maximize method speed and robustness, without the sacrifice pulse-and-acquire methods make for the sake of mathematical tractability.

As described previously, knowledge of all time constants, concentrations, and enzyme rates would allow for a complete description of the signal generated during an MR experiment. Only the reverse process, extraction of underlying tissue properties from a given signal, can be mathematically difficult. Previous MRF methods, designed within the MRF framework, used the *a priori* knowledge of the Bloch equations to build an exhaustive database of all possible signals observed in an MR experiment, and linked each possible signal with the set of tissue properties underlying it. After signal measurement, tissue parameters were successfully extracted through the lookup of each observed signal against the database.

By circumventing the previous requirements imposed by parameter estimation, the MRF framework allows for the pulse sequence design of MR experiments to prioritize the other desirable qualities of an MR experiment: robustness to errors, shorter experiment times, and high signal and information density. To this effect, a large and growing body of ^{1}H methods have been established to more quickly and more robustly measure an ever increasing set of tissue parameters. While a detailed description of these methods is outside of the scope of this dissertation, the MRF framework's flexibility has been leveraged to great success for efficient quantification of proton (^{1}H) relaxation times in the brain[6,7], abdomen[8], and heart[9].

Chapter 3. Efficient Quantification of ^{31}P Metabolite Concentration and T_1 Relaxation by Spectroscopic Magnetic Resonance Fingerprinting in the Absence of Metabolism

Introduction

Magnetic Resonance Spectroscopy (MRS) offers unique opportunity to noninvasively characterize metabolic profiles in a vast array of pathologies due to its chemical specificity. Phosphorus-31 (^{31}P) MRS has been used extensively to assess the energetics of living tissues[10–13]. Furthermore, ^{31}P Magnetization Transfer encoded MRS (MT-MRS) methods are able to measure enzymatic chemical exchange reaction rates of phosphocreatine and ATPase/synthase. However, ^{31}P MT-MRS are limited by long data acquisition time[14]. Although higher field strength and greater field homogeneity can partially ameliorate this problem, the fundamental approach to MRS, i.e., the pulse-and-acquire approach to sampling a steady-state spin system, may not be the most time efficient approach.

The Magnetic Resonance Fingerprinting (MRF) framework has achieved dramatic success in reducing the time necessary to quantify a variety tissue parameters in proton (^{1}H) imaging. MRF's success is rooted, rather than through requiring any specific pulse sequence structure or signal model, in its flexibility of method design such that the most effective designs are enabled. The purpose of this chapter is

to explore the potential of the MRF framework, through translation of existing ^{1}H imaging MRF methods, to accurate and time efficient quantitative ^{31}P MRS methods.

However, fundamental differences between imaging and spectroscopy cause challenges in the translation, implementation, and signal processing of existing ^{1}H MRF imaging methods. First, while MR imaging methods use applied hardware gradients to differentiate the spatial position of nuclei, MRS applies no spatial encoding gradients and instead relies on the inherent shielding/de-shielding of nuclei to differentiate between metabolites. Simply, the encoding magnetic field is actively applied in MRI but passively observed in MRS. This results in fewer degrees of freedom in method design as compared to imaging applications. Previous ^{1}H MRF imaging methods heavily relied upon intentional transient violations of Nyquist sampling limits to decrease experiment time. Spectroscopic chemical shift encoding cannot be performed in a similar manner. The utility of a pulse sequence designed in the MRF framework to increase robustness to hardware noise, and without the presence of Nyquist sampling violations has not been previously established. Developed ^{31}P spectroscopic MRF methods must also be relatively robust to the large B_0 and B_1 inhomogeneity typically encountered in spectroscopy experiments[15,16]. Due to these differences, even without chemical exchange considerations, effective approaches for quantitative ^{31}P spectroscopy methods within the MRF framework have not yet been established.

As a first step towards fast and robust quantification of metabolism *in vivo*, a preliminary end point, the fast and robust quantification of T_1 relaxation time and relative concentrations of *in vitro* metabolites, was used in this study. This choice made because ^{1}H quantification of T_1 using the MRF framework is well established, and T_1 is analogous to the apparent T_1 relaxation time (T_{1app}) crucial for ^{31}P MT-MRS metabolism measurements. We hypothesized that an MRF approach would be able to accurately and more efficiently measure both T_1 relaxation time and relative concentration of multiple metabolites as compared to conventional methods. To this end, components of the balanced Steady State Free Precession based MRF method[6] (bSSFP-MRF), including its associated signal processing and parameter estimation techniques, were translated into several candidate ^{31}P spectroscopic MRF methods. The developed methods were assessed for their utility in quantitative MRS. The sensitivity and robustness of parameter estimation of these candidate ^{31}P spectroscopic MRF designs was evaluated in simulations. One of these options, the ^{31}P-MRF method, was then implemented on a Bruker 9.4T vertical bore scanner. This method was then evaluated for its potential in T_1 and relative M_0 measurement of non-exchanging phosphate metabolites in solution phantom. Post-processing methods to perform parameter quantification of the ^{31}P-MRF data were developed. The accuracy and sensitivity of the ^{31}P-MRF method were compared against conventional inversion-recovery method[15].

Methods

Simulation Study

Monte Carlo simulation was used to examine the effectiveness of several pulse sequence design options. Five candidates MRF pulse sequences, each with 512 bSSFP-type acquisitions following an inversion preparation, were examined in simulation. Each variant used a different combination of flip angle (FA) pattern, and repetition time (TR) pattern. The flip angle patterns consisted of: constant 12° FA, ramped flip angle (see *Pulse Sequence Design*), randomly varied flip angle, and a random flip angle superimposed on the ramped flip angle design. All flip angle patterns shared a mean FA of 12°. Random flip angle patterns were drawn from a normal distribution with standard deviation of 1°. The TR patterns consisted of either a constant 11.2 ms TR, or a random TR drawn from a normal distribution with a mean of 11.2 ms and a standard deviation of 3 ms.

Signal evolution "fingerprints" were generated for each candidate pulse sequence variant. All test fingerprints were generated for Monte Carlo analysis used a T_1 value of 3.6 s and a T_2 value of 0.1 s. Normally distributed noise, with a standard deviation of 3% of M_0, was added to simulated signal evolutions. The accuracy and precision of parameter estimation for each pulse sequence variant was examined under different conditions. A total of 2000 simulations were performed for each analysis.

^{31}P-MRF Pulse Sequence Design

Of the candidate methods investigated in simulation, one of them, the ^{31}P-MRF method, was further investigated in *in vitro* phantom. Following a nonselective hyperbolic secant inversion pulse, 512 RF excitations, each followed by a data acquisition period, were performed in the ^{31}P-MRF method. Excitations were organized into 16 repeated blocks with linearly ramped up and ramped down flip angle between 1.5° to 22.5°. Excitation phase was alternated between consecutive RF pulses. A constant repetition time (TR) was used for all the acquisitions. This constant TR led to an off-resonance frequency-dependent modulation of signal evolution[17] that was TR dependent. Similar to conventional bSSFP and bSSFP-MRF methods, nuclei which accumulated a relative phase equal to an odd multiple of π between consecutive RF excitations exhibited different behavior from nuclei that accumulated a phase equal to an even multiple of π. In bSSFP imaging, this results in the well characterized 'pass-band' and 'null-band' signal regimes. In the current study, while bSSFP based ^{1}H MRF and the ^{31}P spectroscopic MRF do not qualitatively exhibit signal nulling behavior for nuclei with odd multiples of π phase accumulation, the nomenclature was nevertheless preserved.

Data Processing and Parameter Estimation

During data acquisition periods in both simulation and phantom experiments, a time domain FID signal consisting of 544 data points was recorded with a dwell time of 11 μs. A symmetric Gaussian apodization filter was applied to each FID to

reduce spectral leakage. Each FID was Fourier transformed to the spectral domain and the time course of the signals within the spectral bins specific to metabolites of interest were extracted into a single time course signal. This signal fingerprint specifically consisted of the vectorized time course signals pertaining to the central and two adjacent spectral bins closest to the expected resonance frequency of each metabolite.

All fingerprints were quantified using a dictionary template matching approach. To create the dictionaries necessary for this process, code was developed that accepted the four input parameters T_1, T_2, relative chemical shift (δ_f), and linewidth, and generated the corresponding Bloch equation predicted fingerprint given the spectroscopic MRF pulse sequence. Linewidth here describes the chemical shift dispersion amongst nuclei of the same metabolite due to spatial B_0 inhomogeneity. The modeling of linewidth was done by generating the composite signal evolution fingerprint, assuming a Lorentzian distribution of nuclei with a mean and a full-width half-max of relative chemical shifts equal to δ_f and linewidth, respectively, and sharing the input T_1 and T_2 parameters. Scalar coupling between the phosphate moieties of ATP was similarly accounted for by modeling each ATP moiety's fingerprint as the sum of two distinct chemical shift frequencies during Bloch simulation. For each simulation and phantom experiment, a metabolite specific dictionary was created, which varied T_1 value at a 10 ms increment and with fixed values for T_2, relative chemical shift, and linewidth. Dictionary simulation

was performed by in-house developed Matlab software (The MathWorks, Natick, MA).

Parameter quantification for T_1 was performed by selection of the best matching dictionary entry with each measured fingerprint. Quality of match was determined by the inner product metric, which was calculated as the magnitude of the vector dot product between experimental fingerprint and each dictionary entry following l_2 normalization. The T_1 value of the dictionary entry that generated the highest inner product metric was returned as the matched T_1. M_0 was subsequently determined by minimizing the error term $\sum|S - M_0 D|$, where *S* is the measured/simulated signal and D is the matched fingerprint.

Error Analysis

The ^{31}P-MRF dictionary matching method for T_1 quantification was assessed for measurement robustness to potential error sources. The response of the inner product metric used in the presence of errors to fixed parameter discrepancies during dictionary generation was investigated. For a given potential error source, a set of test fingerprints was generated with a fixed T_1, while the error source parameter was varied. The error, assessed as 1 - |inner product metric|, for all test fingerprints was calculated against a dictionary that varied only in T_1 values. A total of five potential error sources were examined: T_2, chemical shift, linewidth, applied B_1 power, and spectral phasing value. Each error source was examined for off-

resonance values under both the null-band and the pass-band regimes. Reference parameters for T_1, T_2, and linewidth parameters used in the simulation were 3.4 s, 0.1 s, and 10 Hz, respectively, to reflect the expected values of PCr in *in vivo* rat heart.

Phantom Studies

Solution phantom experiments were performed to test T_1 and M_0 quantification accuracy of ^{31}P spectroscopic MRF pulse sequence under off resonance values falling within a variety of pass-band and null-band signal regimes. The solution phantom comprised of physiological concentrations of major phosphate metabolites (15 mM PCr, 10 mM ATP, and 3 mM P_i) at 7.1 pH. All data acquisitions were performed on a 9.4T vertical bore system (Bruker Biospin Co., Billerica, MA, USA). 11 separate measurements were made using different carrier frequencies, but with a constant TR of 11.2 ms. The carrier frequencies used ranged from -8.3 to 5.7 ppm at 1 ppm increments.

Ground truth values for T_1 of P_i, PCr, γATP and αATP metabolites were established using conventional Inversion Recovery (IR). For IR, a hyperbolic secant inversion pulse was applied followed by 6 different inversion times that ranged from 0.1 to 15 s. A 40 s inter-scan delay was used to reestablish longitudinal magnetization. Standard processing for conventional spectra was performed, including a 10 Hz line broadening, followed by Fourier transform and peak area integration. T_1 and

M_0 measurements for each species were determined by fitting the data to the 2-parameter exponential model.

The measurement efficiency of three specific variants of the spectroscopic MRF pulse sequence was also assessed, each using a different combination of pulse sequence carrier frequency and TR duration to place metabolite resonances precisely within either a pass-band or a null-band regime. The first sequence, Variant A (TR, 12.21 ms TR; carrier frequency, 400 Hz to the left of PCr), placed PCr and P_i within pass-band regimes and γATP within a null-band regime. The second sequence, Variant B (TR, 13.48 ms; carrier frequency, 445 Hz to the left of PCr), placed all 3 resonances within pass-band regimes. The third sequence, Variant C (TR, 12.35 ms; carrier frequency, 445 Hz to the left of PCr), placed PCr and P_i within null-band regimes and γATP within a pass-band regime. A total of 120 datasets with 1 signal average were acquired for each sequence. Measurement efficiency for all measurements was calculated as:

$$\text{Efficiency} = \frac{\text{Precision}}{\sqrt{\text{Acquisition Time}}}$$

where precision was determined as the mean to standard deviation ratio [6]. Acquisition time included inter-scan delay time for both MRF and conventional IR methods. For all MRF variants, total acquisition time of one fingerprint was ~7 s followed by an 8 s inter-scan delay. For conventional IR, calculation of the efficiency assumed an inter-scan delay of 5 times of the T_1 of the corresponding metabolite.

RESULTS

Simulation and Error Analysis

Figure 3.1 shows the results of Monte Carlo analysis of the five variants of ^{31}P spectroscopic MRF pulse sequences under each of the six test conditions with simulated noise. The three constant TR variants showed accurate and robust measurement to all tested conditions. Measurement precision for the sequence variant using a constant flip angle was found to be 5-9% lower than the two sequence variants that used either ramped flip angles or ramped flip angles with added randomness. Sequence variants which used a random TR showed worse T_1 matching precision for the test conditions with metabolite resonance at 7.2 ppm (1.2 kHz) from the carrier frequency. For the test conditions with a 7.2 ppm metabolite resonance as well as a chemical shift miscalibration or a B_1 error, random TR sequence variant observed a strong bias in both T_1 and M_0 measurements.

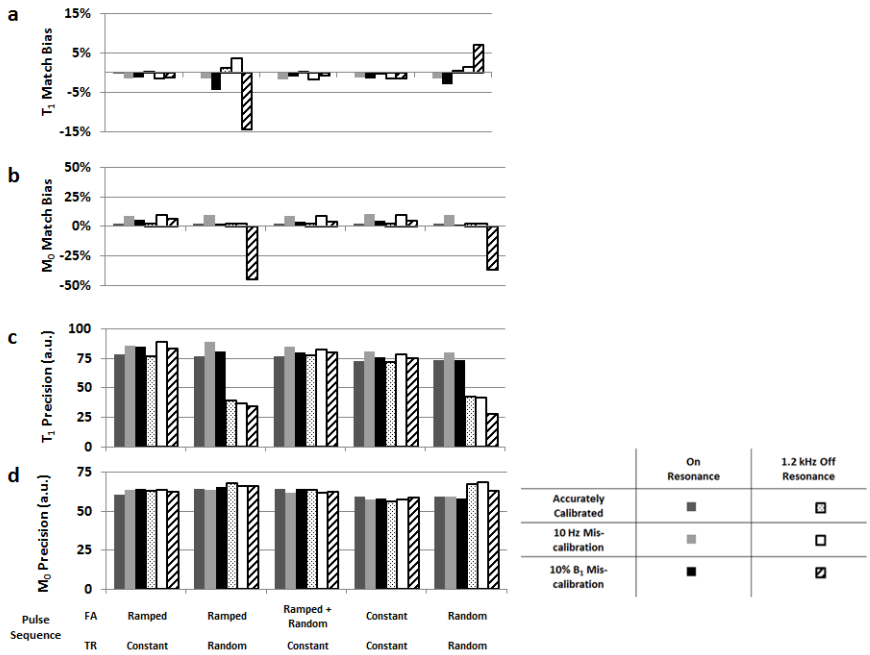

Figure 3.1. Monte Carlo simulation derived matching bias and precision for different sequence design options. Matching bias is shown for T_1 (a) and M_0 (b) in shown, as well as the matching precision in T_1 (c) and M_0 (d). Conditions evaluated in simulation included the permutations of either an on-resonance metabolite or a 7.2 ppm off resonance metabolite, under the conditions of: accurate calibration, with 10 Hz chemical shift miscalibration, or a 10% B_1 power miscalibration.

Figure 3.2 shows the behavior of the inner product metric of the ^{31}P-MRF method for T_1 dictionary matching in the presence of potential error sources. A dictionary, constructed using a varied T_1 value and a fixed potential error source parameter, was matched against test fingerprints, generated using a fixed 3.4 s T_1 value and a varied potential error source parameter. This analysis was repeated separately for metabolites with off-resonance values within either the pass-band regime or the

null-band regime. The errors in the inner product metric are shown as intensity maps across T_1 and one potential error source parameter: T_2, chemical shift, linewidth, B_1 power, and spectral phasing. For resonances with off-resonance values in a pass-band regime (Figure 3.2a-e), the horizontal error minima response to all error source parameters suggests that T_1 matching is relatively insensitive to these parameters, and that errors in these parameters are tolerable for accurate T_1 matching.

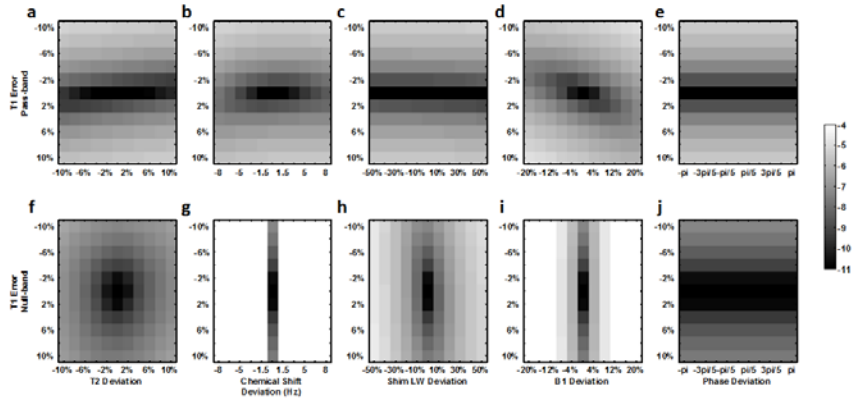

Figure 3.2. Sensitivity of T_1 matching to parameters used in dictionary construction. Each map represents the log of the magnitude of the matching error (i.e. distance from one, where one is a perfect match) of the inner product metric used in matching. Matching errors were assessed between a dictionary varying only in T_1 (y-axis) against data of a fixed T_1 but varied in one of several potential confounding parameters (x-axis). Assessment was performed for metabolite off-resonance values in both the pass-band regime (a-e) and the null-band regime (f-j), respectively.

In contrast, resonances with off-resonance values located in a null-band regime showed relatively vertical error minima responses with respect to chemical shift, shim linewidth, and B_1 power. This result suggests that T_1 cannot be reliably matched without an accurate dictionary value for these parameters (Figure 3.2g-

i). Additionally, signals with off-resonance values located in a null-band also showed decreased sensitivity to T_1 as compared to pass-band signals, exhibited by decreased steepness in gradient across the different T_1 entries.

Phantom Study

A representative acquired MRF dataset, using 64 signal averages, is shown in Figure 3.3. Signal evolution of each metabolite can be resolved from the changes in peak magnitude of the 512 acquired spectra (Figure 3.3a-b), albeit at low spectral resolution (167 Hz) due to the extremely short acquisition window (Figure 3.3c). The fingerprints for P_i, PCr, and γATP showed unique signal evolution patterns due to the encoding of T_1 and chemical shift (Figure 3.3d).

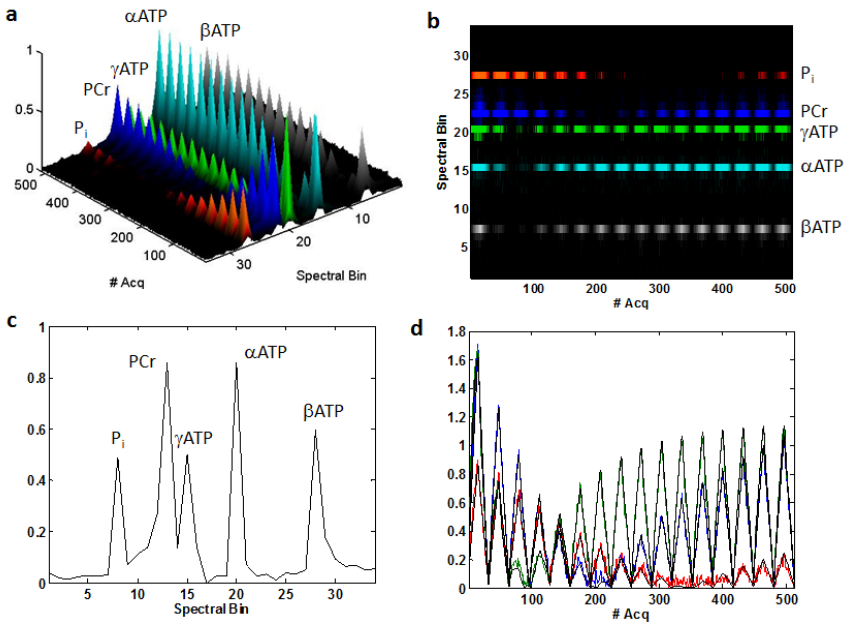

Figure 3.3. MRF signal from a phantom. a. A representative fingerprint with 512 ^{31}P spectra. **b.** The magnitude map of a fingerprint. **c.** A representative spectrum out of the 512 acquisitions of a fingerprint. **d.** The signal evolution from spectral bins corresponding to PCr (blue), γATP (green) and P_i (red) signal superimposed with matched dictionary entries (black).

T_1 measurements by both IR and MRF are shown in Figure 3.4. T_1 values measured by conventional IR method were 7.80, 3.60, 1.76, and 1.32 s for P_i, PCr, γATP, and αATP, respectively (Figure 3.4a). For all the 11 carrier frequencies used, MRF-matched T_1 values showed strong agreement with values measured by the conventional IR method (Figure 3.2b). The mean and standard deviation for P_i, PCr, γATP, and αATP were 7.40±0.54, 3.48±0.06, 1.74±0.05, and 1.26±0.11 s, respectively.

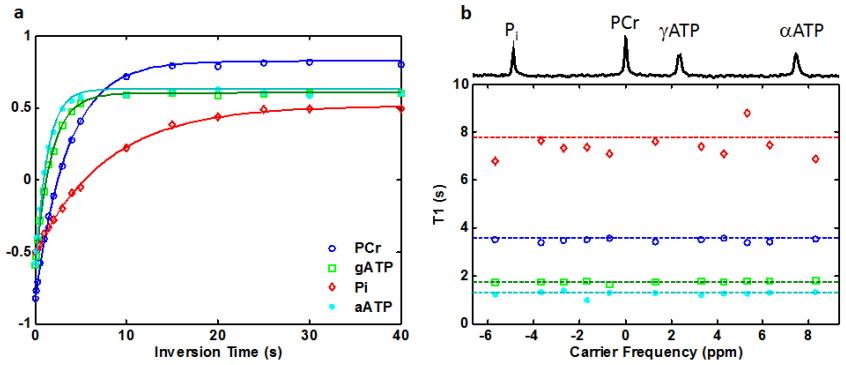

Figure 3.4. Comparison of T_1 measurement by ^{31}P MRF and conventional IR. a. T_1 measurement by conventional IR method. **b**. Values for T_1 matched with MRF data acquired at different carrier frequencies. The locations of the carrier frequencies relative to each resonance peaks are indicated in the spectrum shown at the top. Dotted lines indicate fitted T_1 from conventional IR method.

Figure 3.5 shows measurement accuracy and efficiency of 120 MRF acquisitions acquired using a single signal average for each acquisition. Measurements of both

T_1 and M_0 showed strong agreement between MRF and conventional IR methods when the off-resonance frequencies for resonance peaks were located within a pass-band regime (Figure 3.5a-b). T_1 and M_0 measurement of P_i and PCr using MRF variant C showed the largest discrepancy with the IR method as both resonance peaks were located in null-band regimes. However, MRF-measured T_1 and M_0 for γATP within a null-band regime in sequence A were still accurate. Measurement efficiency for PCr and γATP consistently outperformed IR by 46% to 146% for pass-band regime variants. Despite a non-physiological, long T_1 value for P_i, comparable efficiency was achieved for variants where P_i was placed within a pass-band regime. T_1 and M_0 measurements for γATP placed in a null-band regime showed comparable efficiency as the conventional IR method.

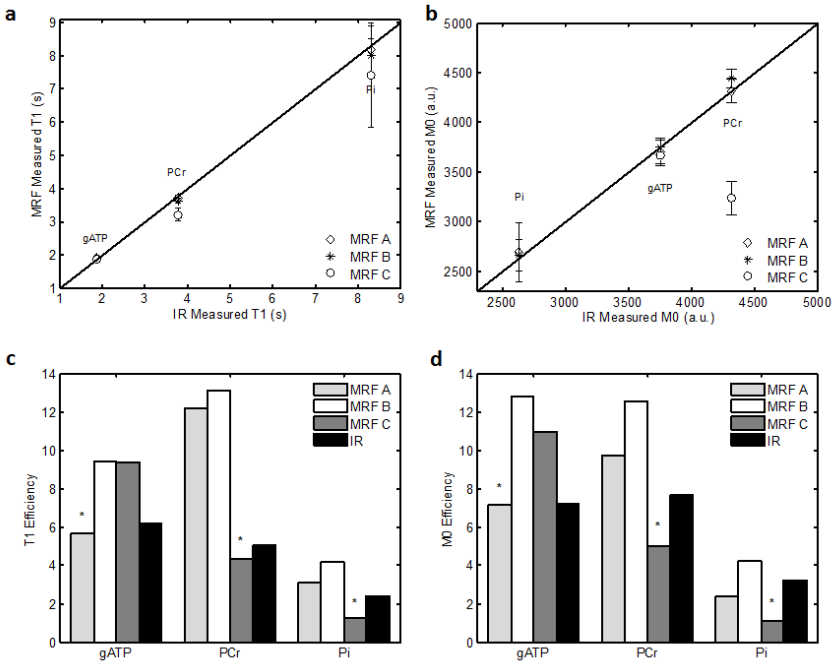

Figure 3.5. Accuracy and efficiency of MRF and IR. a-b. Comparison of 120 repeated MRF measurements of T_1 (a) and M_0 (b) with the classic IR method. Solid lines in represent the line of identity. **c-d.** The efficiency of MRF compared to classic IR for T_1 (c) and M_0 (d) measurements. Asterisks denote when a resonance was located in a null-band.

Discussion

In the current study, we demonstrated the feasibility, accuracy, and efficiency of a pulse sequence design using the MRF framework for quantitative ^{31}P spectroscopy measurements. The ^{31}P-MRF method, using short and constant TR with ramped flip angles combined with a dictionary-based template matching approach, was selected based from simulation experiment results. Measurements of solution phantom, without *a priori* placement metabolite off-resonances within pass-band

regimes showed relatively accurate T_1 measurements with some variations. T_1 quantification performance under specific TR and carry frequency combinations to place metabolite off-resonance values specifically within the pass-band and null-band regimes showed results that were consistent with simulation analysis. Pass-band metabolites measured *in vitro* by ^{31}P spectroscopic MRF were accurate, and more efficient compared to the conventional inversion recovery based method in metabolites with physiologically relevant T_1 values. Specifically, the measurement efficiency showed a 46% to 146% improvement for pass-band PCr and γATP metabolites.

Monte Carlo simulation experiments showed that randomness in pulse sequence design was not inherently optimal for the current ^{31}P spectroscopy application. Random TR patterns for pulse sequence design were susceptible to matching inaccuracies and decreased precision within pass-band regimes for far off-resonance metabolites as compared to constant TR pattern for pulse sequence design. Random flip angle variations superimposed on a ramped flip angle train also did not improve accuracy or precision for T_1 and M_0 measurements under the conditions examined (Figure 3.2). Based on these results, the implemented ^{31}P-MRF sequence used constant TR pattern with regular linearly ramped flip angle trains.

The simulation error analysis showed placement of metabolite off-resonance in null-band regimes was inferior compared to placement within pass-band off-resonance regimes. Pass-band regime metabolites were robust to the investigated potential error sources, including T_2, chemical shift, linewidth, B_1 power, and spectral phasing. In particular, due to the insensitivity to T_2 and chemical shift for resonances located in pass-band regimes, these two parameters were not necessary to include as matched parameters in dictionaries. This approach allowed for fewer dimensions in the dictionary. Null-band regime metabolites were sensitive to errors in parameters chemical shift, linewidth, and B_1 power, and also exhibited an overall inner product gradient to different T_1 values. Phantom results were consistent with these findings. Quantification of the null-band regime metabolites (P_i and PCr in variant C, γATP in variant A) parameters were more prone to bias and decreased efficiency. These results indicated that spectroscopic MRF pulse sequence design should seek to avoid null-band regimes.

The TR durations investigated in the current sequences were far shorter than the typical FID readout duration used in conventional spectroscopy experiments. This required several adjustments to the subsequent signal processing. Short TR durations caused truncation of each FID signal, leading to low spectral resolution (~167 Hz), and spectral leakage effects[18]. To reduce spectral leakage, a Gaussian filter was applied to each FID signal before applying the Fourier transform. This filtering reduced the tails of the spectral lineshape from each metabolite's spectral

peaks, but at the cost of increased full-width-half-max (FWHM) and reduced peak height (SNR). The resulting FWHM was on the same order as the spectral resolution. Because of these combined factors, conventional curve fitting methods would have been under-determined and inaccurate[19]. Instead, the current study incorporated the entire signal generation, detection, and processing steps within the dictionary generation model. Template matching using the generated dictionary, using the central three spectral bins of each spectral resonance should therefore theoretically appropriately incorporate all of these effects. One benefit to this approach was that operator-dependent processing steps such as curve fitting[20] or spectral phase and baseline distortion correction are avoided. The drawback of FID truncation and subsequent Gaussian filtering, however, was an SNR penalty. This may be mitigated in future methods by incorporating alternative post processing methods[21,22] or frequency selective RF pulses.

The improvements achieved during *in vitro* experiments was limited by the currently available system hardware. First, the required data writing time to system RAM after each acquisition (~5 ms for our current hardware) reduced the data acquisition window to only 6 ms within each TR (11 ms). Second, after the 7 s acquisition of each fingerprint, an inter-scan delay of 8 seconds was required for writing the acquired data to the hard disk. These hardware limitations reduced measurement SNR and increased measurement time, and lowered the efficiencies of the MRF method in the current study. Furthermore, the memory size of the system limited the maximum number of acquisitions frames for each fingerprint to

512, leading to the incomplete coverage of signal recovery for the long T_1 of P_i *in vitro*.

In conclusion, we present a first step in quantitative spectroscopic measurements using the MRF framework. This work sought to encode T_1 relaxation time and M_0 efficiently for multiple metabolites across a large spectral bandwidth. Despite a relatively simple pulse sequence and dictionary matching method, spectroscopic MRF was able to significantly increase measurement efficiency while retaining robustness to various measurement errors. With the incorporation of additional encoding, the MRF approach may enable the efficient quantification of other physiologically relevant spectroscopy tissue properties.

Chapter 4. Rapid *In Vivo* Quantification of Creatine Kinase Metabolism by ^{31}P Spectroscopic Magnetic Resonance Fingerprinting

Introduction

^{31}P magnetization transfer (MT) techniques have a long history of use in quantifying the phosphocreatine (PCr) synthesis rate via creatine kinase (CK) in heart, skeletal muscle, and brain[13,23–29]. The MT techniques, outlined in Chapter 2, are capable of accurate measurement of creatine kinase metabolism, but require a long data acquisition time, necessitated by the low metabolite concentrations.

Several methods have been proposed over the years that attempt to shorten the acquisition time by using a combination of two strategies. Conventional MT requires the acquisition of a large number of fully relaxed spectra, and the first strategy to reduce acquisition time is to acquire reduce the number of spectra and acquire them under only partially relaxed conditions. Methods using this strategy include the Four Angle Saturation Transfer (FAST) method[14], and the Triple Repetition Time Saturation Transfer (TRiST) method[30]. Reducing the number of acquired spectra is particularly useful in combination with CSI methods for spatially localized measurements. However, as the number of acquired spectra

approaches the number of parameters to be estimated, the spectra must be of high SNR to achieve satisfactory robustness. Hence, these methods are limited for inherently low SNR applications. The second strategy to shorten acquisition times is to reduce the number of parameters to estimate by assuming an intrinsic T_1 value for PCr. Methods using this strategy includes the Two Repetition Time Saturation Transfer (TwiST)[31] and the T_1 Nominal[16] methods. However, although several studies have reported no detectable changes in the T_1 of PCr under pathological conditions, this does not guarantee that the T_1 of PCr remains constant in all pathologies and thus fixing the T_1 value may lead to measurement errors. Thus, a new strategy should be explored.

The Magnetic Resonance Fingerprinting (MRF) framework allows for greater flexibility in pulse sequence design than conventional methods. This flexibility has been leveraged with great success in efficient quantification of proton (^{1}H) relaxation times in the brain[6,7], abdomen[8], and heart[9]. In Chapter 3, the MRF framework was adapted successfully to measure T_1 in ^{31}P metabolites *in vitro*. The framework achieved an increased measurement efficiency compared to the conventional spectroscopy IR method. However, due to the lack of specific MT specific to the pulse sequence, the previous ^{31}P spectroscopic MRF method must be modified before it can be used to measure MT encoded metabolism. In this chapter, the ^{31}P spectroscopic MRF pulse sequence was further adapted and refined to quantify MT encoded CK metabolism, in addition to other parameters. The robust pulse sequence design choices as evaluated in Chapter 3 were

combined with a frequency selective saturation pulse to develop the creatine kinase encoded ^{31}P spectroscopic MRF (CK-MRF) sequence with unique sensitivity to MT encoded CK metabolism.

Specifically, the CK-MRF followed the previously successful ^{31}P bSSFP-type design[32], using a ramped flip angle scheme[33] with constant TR to increase SNR efficiency. Selective saturation pulses and excitation pulses were rapidly alternated to simultaneously encode magnetization transfer and sample transient signal evolutions. Additionally, two challenges encountered by the previously proposed ^{31}P spectroscopic MRF method were circumvented. First, the low spectral resolution and subsequent spectral leakage effects related to using short TR were avoided by using spectrally selective pulses to excite only one metabolite during any given TR. Second, by adopting a sinusoidal flip angle modulation scheme, the interscan delay between consecutive fingerprint acquisitions, previously required to allow magnetization recovery between scans, were removed to further hasten the scan time. The modulation scheme, using low flip angles during the beginning and the end of the pulse sequence, allowed simultaneous continuous acquisition of signal while allowing partial magnetization recovery.

We hypothesized that this approach would lead to accurate and more time efficient measurements of CK metabolism as compared to conventional methods. The accuracy and robustness of this method was first evaluated in simulation studies

in which several potential error sources were assessed. *In vivo* studies on rat hindlimb were performed to validate the CK-MRF measurements against a conventional ^{31}P magnetization transfer (MT-MRS) method. Finally, a reproducibility comparison between the proposed CK-MRF method and the MT-MRS and FAST methods was performed.

Methods

Pulse Sequence Design

A schematic of the CK-MRF pulse sequence is shown in Figure 4.1a. Following an inversion preparation, a bSSFP-type acquisition scheme for ^{31}P spectroscopy was employed. The acquisition was made up of a total of 32 acquisition blocks. Two types of acquisition blocks, ACQ-PCr and ACQ-γATP, were used to acquire signals from PCr and γATP, respectively. A 490-ms selective saturation block was used between two acquisition blocks, with the saturation frequency set either at the resonance frequency of γATP (SAT-γATP) or at the frequency contralateral to γATP (SAT-CNTL). The entire acquisition is comprised of two modules that employed SAT-CNTL and SAT-γATP, respectively, with the two acquisition blocks for PCr and γATP alternated eight times in each module.

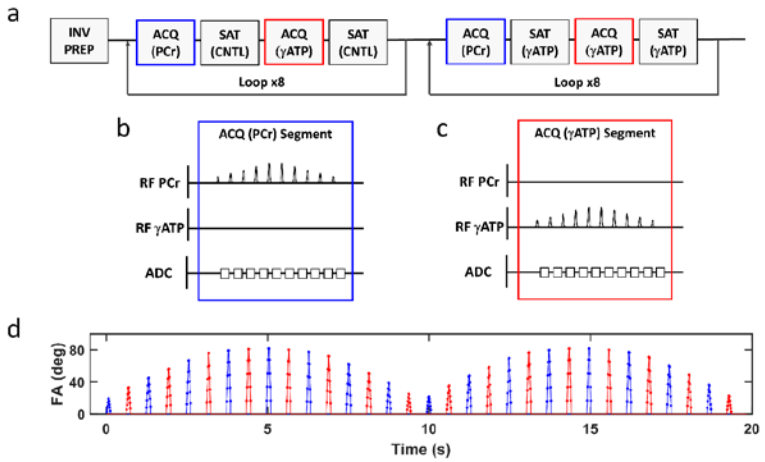

Figure 4.1. CK-MRF pulse sequence design. **a.** Schematic of the CK-MRF pulse sequence. ACQ (PCr) and ACQ (γATP) are acquisition blocks for PCr and γATP, respectively. SAT (CNTL) and SAT (γATP) are contralateral and γATP saturation blocks, respectively. **b** and **c.** Pulse sequence diagrams for one block of ACQ (PCr) (b) and ACQ (γATP) (c). **d.** Timing and nominal flip angles of all excitation pulses. Blue and red colors indicate PCr and γATP excitation, respectively.

Diagrams of acquisition blocks for ACQ-PCr and ACQ-γATP are shown in Figures 4.1b and 4.1c. Each block consisted of a train of 10 linearly ramped-up and ramped-down excitations with alternating phase and a constant TR of 12.8 ms. Selective excitation was performed with a 4 ms Gaussian pulse centered at the resonance frequency of PCr and γATP, respectively. Following each excitation, 7.9 ms of FID signal was collected.

The nominal flip angle, frequency, and timing of all 320 RF excitations for CK-MRF are shown in Figure 4.1d. The maximum flip angles in the 32 acquisition blocks

were modulated by a sinusoidal envelope. The total time for one complete CK-MRF acquisition was 20 s. Multiple repetitions were acquired with no delay, with a single dummy acquisition preceding each series of repetitions.

Fingerprint Simulation

Signal time courses, i.e. the fingerprints, were simulated by solving the modified Bloch-McConnell equations[14,34] with two exchanging pools, i.e., PCr, and γATP. Details of the simulation methods are described in the Appendix. Simulation of a fingerprint required a total of nine input parameters: the forward rate constant of ATP synthesis via CK (k_f^{CK}), the concentration ratio of PCr-to-ATP (M_R^{PCr}), the T_1 and T_2 relaxation times and the resonance frequencies (chemical shift) of PCr and γATP (T_1^{PCr}, T_1^{ATP}, T_2^{PCr}, T_2^{ATP}, ω^{PCr}, ω^{ATP}), as well as B_0 distribution characterized by a linewidth, LW. Given a set of input parameters, spin evolution was simulated in sequential time steps, starting from a fully relaxed initial condition. Excitation was simulated by discretizing the Gaussian shaped RF pulse into 41 instantaneous complex rotations (Equations A7-9), with the magnitude of the rotation following a Gaussian envelope, and the total rotation summing to the nominal FA. The phase of each rotation was determined by the excitation frequency. γATP saturation was simulated by instantaneous saturation of γATP magnetization with no direct effect on PCr magnetization. The pulse sequence was simulated sequentially twice to account for the dummy scan. For each simulation, all FID signals were recorded from the bulk transverse magnetization, described as $S(t)$ in Equation A12.

Dictionary Generation

The dictionary in the MRF framework is a set of fingerprints, or signal evolutions, for selected values of the tissue properties. Four tissue properties, namely k_f^{CK}, T_1^{PCr}, ω^{PCr}, and M_R^{PCr}, were varied over their physiologically expected range to generate a dictionary for template matching. Specifically, 51 values of k_f^{CK} ranging from 0.3 to 0.55 s^{-1} with a resolution of 0.005 s^{-1}, 20 values of T_1^{PCr} uniformly distributed from 2.8 to 4.7 s, 11 values for ω^{PCr} spanning from -15 to 15 Hz, and 49 values for M_R^{PCr} uniformly distributed from 3.0 to 5.4 were simulated. It is worth noting that these ranges of parameter variations reflect physiological variations expected in the current study and may need to be expanded for other studies. $\omega^{\gamma\mathrm{ATP}}$ for each entry was constrained to $(\omega^{\mathrm{PCr}} - 2.4)$ ppm. The remaining 5 parameters, T_2^{PCr}, $T_2^{\gamma\mathrm{ATP}}$, $T_1^{\gamma\mathrm{ATP}}$, and LW, were set at 120 ms, 16 ms, 0.8 s, and 15 Hz respectively based on pilot data. $T_1^{\gamma\mathrm{ATP}}$ value was corrected to compensate for NOE contributions[35,36] from αATP and βATP.

Parameter Matching

Matching was performed in the frequency domain to reduce memory load. Each of the 320 FIDs, for all acquired data and simulated dictionary entries, was Fourier transformed, and the complex-valued data points corresponding to PCr or γATP

resonances in these spectra were selected. This resulted in a time course signal, the fingerprint, showing the evolution of PCr and γATP peaks. The inner products between the normalized fingerprint and all entries of the normalized dictionary were computed. The dictionary entry that produced the largest magnitude of the inner product was considered to be the best match. From this match, the values of k_f^{CK}, T_1^{PCr}, ω^{PCr}, and M_R^{PCr} were derived. Subsequently, the spin density of γATP ($M_0^{\gamma\mathrm{ATP}}$) was computed as the scale factor between the fingerprint and its matched dictionary entry. All data processing and parameter estimation were fully automated.

Conventional MT-MRS

Conventional MT-MRS method was used for validation and comparison. MT-MRS acquisition consisted of 9 spectra: 7 spectra acquired after γATP saturation, with saturation times of 0.4, 0.9, 1.3, 2.2, 3.5, 5.3 and 7 s, respectively; a control spectrum with contralateral saturation; and a conventional spectrum without saturation[16]. All spectra were acquired using 90° excitation and a 16 s TR. Saturation was accomplished by applying continuous wave RF to the frequency of saturation. Post-processing consisted of 15 Hz line broadening, Fourier transform, and correction of spectral phase and baseline. For phase correction, zero- and first-order phase correction values were obtained manually from spectrum with 12 signal averages and no γATP saturation. These phase correction values were applied to all the spectra acquired from the same animal. The phase correction

was followed by automated baseline correction. The signal intensity from PCr was quantified by integration of the area under the PCr peak. Subsequently, k_f^{CK}, T_1^{PCr}, and M_0^{PCr} were determined by fitting the explicit solution of the Bloch-McConnell equation to the experimental data[37]. Effects of RF spillover were corrected using the method outlined by Kingsley et al.[38].

FAST Method

The reproducibility and efficiency of the CK-MRF measurements were also compared with the FAST method. The FAST acquisition consisted of 4 spectra acquired with either 15° or 60° FA, and with either γATP or control saturation[14]. A BIR-4 pulse was used for excitation. All the spectra were acquired after five dummy scans with a TR of 1 s. Parameter estimation of k_f^{CK}, T_1^{PCr}, and M_R^{PCr} for FAST data was performed using the established closed-form derivation.

Simulations Study

Performance of Parameter Quantification using Dictionary-Based Approach

Simulations were performed to assess the potential errors in parameter quantification caused by using a dictionary generated with a finite resolution. A total of 1000 sets of k_f^{CK}, T_1^{PCr}, ω^{PCr}, and M_R^{PCr} values were randomly generated with upper and lower bounds consistent with the dictionary's ranges. The

remaining 5 input parameters, i.e., $\omega^{\gamma\mathrm{ATP}}$, T_2^{PCr}, $T_2^{\gamma\mathrm{ATP}}$, $T_1^{\gamma\mathrm{ATP}}$, and LW were fixed, with $\omega^{\gamma\mathrm{ATP}}$ constrained to $(\omega^{\mathrm{PCr}} - 2.4)$ ppm. Test fingerprints were generated by simulation of the CK-MRF pulse sequence for each set of parameter values and were matched against the dictionary. The matching errors were calculated as the difference between the matched parameters and the parameters used in simulation.

Sensitivity of Parameter Quantification to Fixed Parameter Values

Since five parameters ($\omega^{\gamma\mathrm{ATP}}$, T_2^{PCr}, $T_2^{\gamma\mathrm{ATP}}$, $T_1^{\gamma\mathrm{ATP}}$, and LW) were either constrained or not varied in the dictionary, errors in their values may affect the accuracy of the matched parameters. Simulations were performed to assess how incorrect selection of the fixed parameters could influence the matched parameters. In addition to these five parameters, the impact of a constant B_1 scale error, resulting in a consistent error in flip angles, was also evaluated. First, a test parameter set (800, 3700, 16 and 120 ms for $T_1^{\gamma\mathrm{ATP}}$, T_1^{PCr}, $T_2^{\gamma\mathrm{ATP}}$, and T_2^{PCr}, -389 and 0 Hz for $\omega^{\gamma\mathrm{ATP}}$ and ω^{PCr}, 0.42 s^{-1} for k_f^{CK}, 4.1 for M_R^{PCr}, and 15 Hz LW, respectively) was chosen to evaluate how errors in the fixed parameters could alter dictionary matching results. To assess the impact on matching accuracy using fingerprints with different fixed parameter values, test fingerprints were generated for each fixed parameter where the fixed parameter value was varied. These test fingerprints were then matched to the dictionary. The potential impact of each fixed parameter was assessed by calculating the error between the matched

parameters and the true test parameter values. Error calculations for T_2^{PCr}, $T_2^{\gamma\mathrm{ATP}}$, $T_1^{\gamma\mathrm{ATP}}$ were performed by varying each of these fixed parameters between 50% and 150% of its test value. Error calculations for $\omega^{\gamma\mathrm{ATP}}$ used a range of -430 to -349 Hz. Error calculations for B_1 were performed by scaling all flip angles to between 50% and 150% of their nominal values.

In addition to error analyses, the effect of P_i-to-ATP exchange on parameter estimation, as well as the errors associated with using contralateral saturation to correct for the spillover effect of the γATP saturation on PCr, were also evaluated by simulation (See Supplemental Methods and Figures).

In Vivo Study

In vivo studies were performed to assess the accuracy of the CK-MRF measurements in rat hindlimb. Details of the experimental setup have been described previously[39]. Briefly, three-month-old Sprague-Dawley rats (n=17) were anesthetized and positioned laterally in a cradle. The hindlimb was secured within a 15-mm ^{31}P coil placed within a ^{1}H volume coil and positioned at the isocenter of a 9.4T MRI scanner (Bruker Biospin Co., Billerica, MA). An air pressure cuff was placed proximal to the coil. Body temperature was maintained at above 35°C via a feedback control system (SA Instruments, Stony Brook, New York, USA). The respiratory rate was maintained between 45 and 60 breaths per minute by

manually adjusting the anesthesia level. The animal protocol was approved by the Institutional Animal Care and Use Committee of Case Western Reserve University.

Following initial stabilization, shimming, and B_1 power calibrations, CK-MRF and MT-MRS data were acquired at baseline. Due to their substantially different acquisition times for a single-average dataset (20 s for CK-MRF versus 150 s for MT-MRS), 24 repetitions of CK-MRF data (8 min acquisition) and 4 repetitions of MT-MRS data (10 min acquisition) were acquired in an interleaved manner such that the total time allocated to each method was similar. A total of 96 repetitions of CK-MRF data and 12 repetitions of MT-MRS data were acquired. 14 rats subsequently underwent two rounds of ischemia/reperfusion (IR) before a second data collection session. Each round of ischemia was induced by inflating the cuff to above 200 mmHg for a duration of 17 min. Following each round of ischemia was a round of 17 minutes of reperfusion. At the end of the IR protocol, another session of data collection started, in which a total of 48 repetitions of CK-MRF data and 8 repetitions of MT-MRS data were acquired.

High SNR signals were obtained by averaging all repetitions from a data acquisition session in data analysis. For CK-MRF, this amounted to 96 and 48 averages for data acquired at baseline and post-IR, corresponding to a total acquisition time of 32 and 16 min, respectively. For MT-MRS, the number of signal

averages was 12 and 8 at baseline and post-IR, corresponding to 30- and 20-min acquisition, respectively.

The remaining three rats were used as the controls. They underwent the same data collection sessions, separated by a 70-min period, during which CK-MRF and FAST data were collected. Acquisition of 24 repetitions of CK-MRF data and 120 repetitions of FAST data were interleaved. A total of 96 and 480 repetitions were collected for the CK-MRF and FAST methods, respectively.

Statistical Analysis

All data processing, simulations, and statistical analysis were performed by custom-built software written in Matlab (Mathworks, Natick, MA). All results are presented as mean ± SD. High SNR signals were obtained by averaging all repetitions from a data collection session. Bland-Altman plot was used to compare CK-MRF and MT-MRS measurements with high SNR. The coefficient of variation (CV) of an estimated parameter, calculated as the ratio of the standard deviation to the mean, was used to assess the reproducibility. Two-tailed paired Student's *t*-test was used to determine the significance of any observed differences between the CK-MRF and MT-MRS or FAST methods, or before and after IR. Two-tailed unpaired Student's *t*-test were used to determine the significance of differences observed following IR compared to controls, as well as the differences between

coefficients of variation in reproducibility study. A *p* value less than 0.05 was considered significant.

Results

Simulation Results

Performance of Parameter Quantification using Dictionary Based Approach

Figure 4.2 shows the performance of the dictionary approach for parameter quantification. The average errors for matched parameters were 0.0014 s^{-1} for the forward rate constant of CK (k_f^{CK}), 0.03 s for T_1 of PCr (T_1^{PCr}), 0.74 Hz for chemical shift of PCr (ω^{PCr}), and 0.014 for the PCr-to-ATP ratio (M_R^{PCr}), The worst case error for each parameter was 0.006 s^{-1} for k_f^{CK}, 0.129 s for T_1^{PCr}, 1.55 Hz for ω^{PCr}, and 0.049 for M_R^{PCr}. With the exception of T_1^{PCr} errors, these errors were approximately one half of the dictionary step for each parameter.

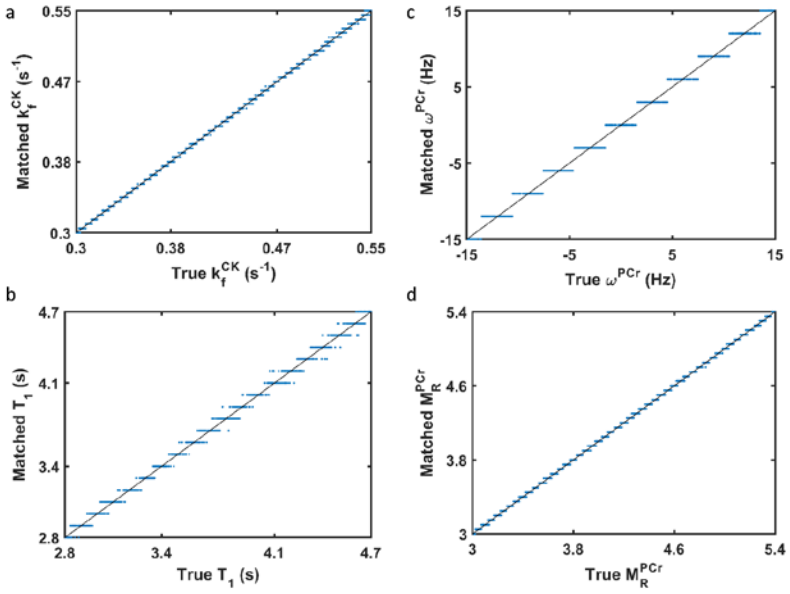

Figure 4.2. Comparison of dictionary matched values with the ground truth values. For each fingerprint generated using a random set of values for the four parameters to be determined, its dictionary matched parameter value for k_f^{CK} (a), T_1^{PCr} (b), ω^{PCr} (c), and M_R^{PCr} (d) is plotted against its corresponding true value. Lines of identity are included in each plot.

Sensitivity of Parameter Quantification to Fixed Parameter Values

Figure 4.3 shows the effects of discrepancies in fixed parameters on the accuracy of the estimation of T_1^{PCr}, k_f^{CK}, M_R^{PCr}, and $M_0^{\gamma\mathrm{ATP}}$. No errors in ω^{PCr} were observed in any of the tested ranges. Discrepancies in $T_1^{\gamma\mathrm{ATP}}$, $T_2^{\gamma\mathrm{ATP}}$, and B_1 resulted in significant errors in the matched parameters. Specifically, overestimation of $T_1^{\gamma\mathrm{ATP}}$ caused underestimation of k_f^{CK} and $M_0^{\gamma\mathrm{ATP}}$ and overestimation of M_R^{PCr} (Figure 4.3a). Errors in $T_2^{\gamma\mathrm{ATP}}$ led to less than 5% error in matched k_f^{CK} for the range

investigated but resulted in errors primarily in M_R^{PCr} and $M_0^{\gamma\mathrm{ATP}}$ (Figure 4.3b). A miscalibration in B_1 power resulted in significant errors in matched T_1^{PCr} and $M_0^{\gamma\mathrm{ATP}}$ but minimally affected k_f^{CK} and M_R^{PCr} (Figure 4.3c). Finally, errors in $\omega^{\gamma\mathrm{ATP}}$, T_2^{PCr} and LW caused relatively small errors in all matched parameters (Figure 4.3d-f).

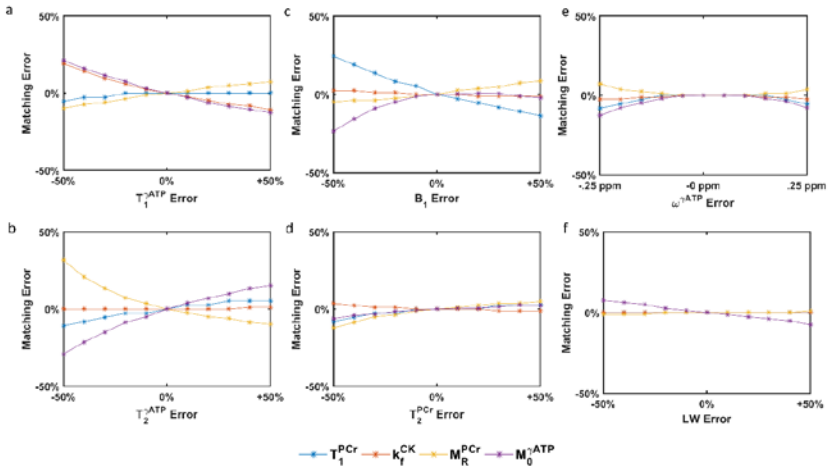

Figure 4.3. Errors in matched parameters k_f^{CK}, T_1^{PCr}, M_R^{PCr}, and $M_0^{\gamma\mathrm{ATP}}$ caused by using values for fixed parameters that differ from those assumed when generating the dictionary: $T_1^{\gamma\mathrm{ATP}}$ (a), $T_2^{\gamma\mathrm{ATP}}$ (b), B_1 (c), T_2^{PCr} (d), $\omega^{\gamma\mathrm{ATP}}$ (e), and LW (f).

Sensitivity of Parameters Quantification to P_i-to-ATP Exchange

Figure 4.4 shows the matching errors caused by using a two-pool exchange model. The effects of P_i-to-ATP exchange on the accuracy of the matched parameters were evaluated by increasing both the forward rate constant of P_i-to-ATP (k_f^{Pi}, Figure 4.4a) and the P_i-to-ATP concentration ratio (M_R^{Pi}, Figure 4.4b). At the current dictionary resolution, parameter matching using the two-pool exchange

model produced no detectable errors until k_f^{Pi} surpassed 0.17 s^{-1}. An increase in k_f^{Pi} from 0.17 to 0.4 s^{-1} resulted in errors in the estimation of k_f^{CK}, T_1^{PCr}, and M_R^{PCr} by -1.2, 1.2, and 2.7% respectively (i.e. one dictionary step). Similarly, increase in P_i-to-ATP ratio produced no detectable errors until its value surpassed 0.35. As M_R^{Pi} increased to 2.0, errors in k_f^{CK}, T_1^{PCr}, and M_R^{PCr} increased, but remained below 5%. No errors in ω^{PCr} were observed in any cases.

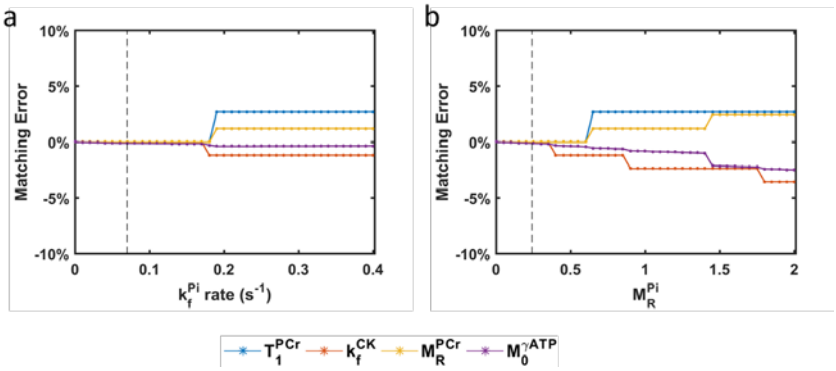

Figure 4.4. Matching error due to exchange between Pi and ATP. Simulations investigated the impact of Pi-to-ATP forward rate constant, k_f^{Pi} (a) and Pi-to-ATP pool size ratio, M_R^{Pi} (b) on the matching error of k_f^{CK}. Dotted lines indicate literature value for resting skeletal muscle from rats[40].

Sensitivity of k_f^{CK} Quantification to Selective Saturation Power

The errors introduced by not fully modeling the spillover effect of the saturation pulses are shown in Figure 4.5. Each investigated method showed a power-dependent error in k_f^{CK} quantification. For CK-MRF and MT-MRS, an "optimal" saturation power was available that could obtain error free quantification. Using a lower than "optimal" saturation power for both methods would lead to

underestimation of k_f^{CK}, due to incomplete saturation of γATP. Using a higher than "optimal" saturation power led to overestimation of k_f^{CK} due to incomplete correction of the spillover on PCr. Errors in k_f^{CK} estimation by CK-MRF was comparable to conventional MT-MRS, while the FAST method showed a ~6% underestimation of k_f^{CK} throughout the range of RF power investigated. MT-MRS using the Kingsley-Monahan correction method showed the least errors compared to the other methods.

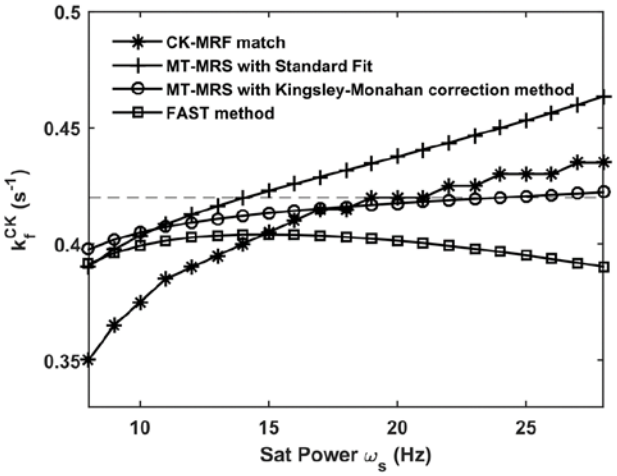

Figure 4.5. Comparison of impact of saturation pulse power choice between methods. Dotted line indicates the true value of k_f^{CK} used in simulation.

In Vivo Results

Figure 4.6 shows representative fingerprints acquired *in vivo* with either 96 averages (Figure 4.6a or single average (Figure 4.6b), with the corresponding

matched dictionary entries shown as solid lines. With 96 signal averages, the average inner product between an acquired fingerprint and its matching dictionary entry was 0.998 ± 0.001. The inner product between a single-averaged fingerprint and its matching dictionary entry was 0.981 ± 0.008.

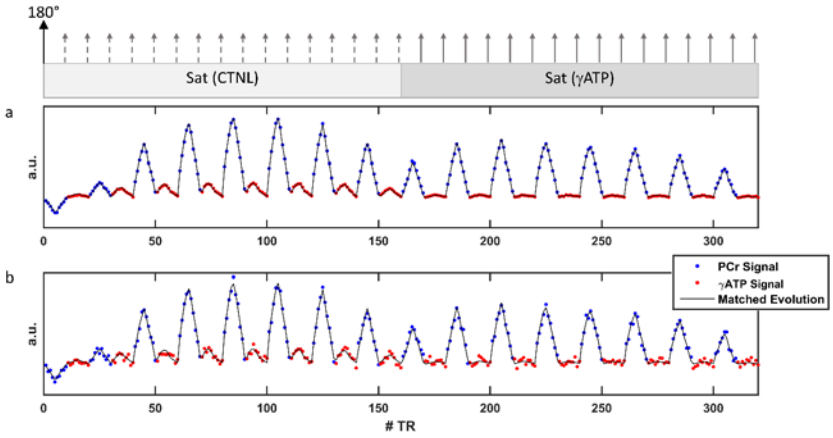

Figure 4.6. Representative in vivo CK-MRF fingerprints. Fingerprints and their corresponding dictionary matches from 96 signal averages (a) and single average (b) are shown. Blue and red data points represent PCr and γATP peaks, respectively. Relative timings for inversion and saturation pulses are indicated at the top. Dashed and solid arrows indicate contralateral and γATP saturation pulses, respectively.

Comparison of In Vivo CK-MRF

Group statistics for *in vivo* data are summarized in Table 4.1. Figure 4.7 shows the Bland-Altman comparison of k_f^{CK}, T_1^{PCr}, and M_R^{PCr} measurements obtained from high SNR data for both CK-MRF and MT-MRS. The use of CK-MRF led to a slight underestimation of k_f^{CK} with a difference of -3.6±4.8% ($p<0.05$). Difference

in T_1^{PCr} and M_R^{PCr} measurements were insignificant with values of 0.7±5.3% and -1.2±5.3%, respectively.

Table 4.1. Summary of Measured Parameter Values Pre-IR and Post-IR

		Signal Averages	k_f^{CK} (s^{-1})	T_1^{PCr} (s)	M_R^{PCr}
Pre-IR	**MT-MRS**	12	0.39 ± 0.03	3.49 ± 0.11	4.22 ± 0.20
	CK-MRF	96	0.38 ± 0.02*	3.54 ± 0.11	4.16 ± 0.19
Post-IR	**MT-MRS**	8	0.44 ± 0.04†	3.48 ± 0.19	4.11 ± 0.30
	CK-MRF	48	0.42 ± 0.03*†	3.49 ± 0.13	4.07 ± 0.19†

*p<0.05, MT-MRS versus CK-MRF

†p<0.05, Pre-IR versus Post IR

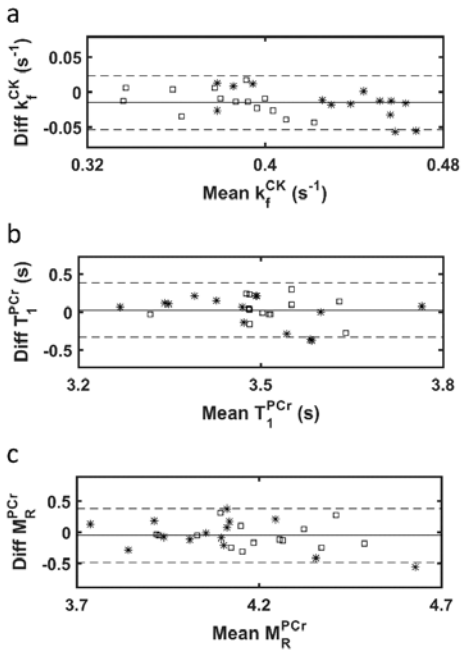

Figure 4.7. Comparison between parameter measurements by CK-MRF and MT-MRS. Bland-Altman plots are shown for k_f^{CK} (a), T_1^{PCr} (b), and M_R^{PCr} (c). Squares indicate pre-IR data and stars indicate post-IR data. Solid lines indicate mean differences and dashed lines indicate limits of agreement.

Compared to baseline values, both methods detected a significant post-IR increase in k_f^{CK} of ~13% ($p<0.05$). This increase was also significant compared to k_f^{CK} changes measured in control animals. Additionally, a decrease in M_R^{PCr} was observed in post-IR data from both CK-MRF and MT-MRS methods. However, only the differences measured by CK-MRF were found to be significant.

Reproducibility of In Vivo CK-MRF vs MT-MRS

Representative time courses of repeated parameter measurements by CK-MRF and MT-MRS during a data collection session at baseline are shown in Figure 4.8. The difference in measurement density for single-average data (Figures 4.8a-c) is due to the difference in acquisition time between the two methods (20 versus 150 s). Comparison between measurements made with approximately equal acquisition time (140 versus 150 s), i.e. seven averages for CK-MRF, are shown in Figures 4.8d-f. Mean parameter values obtained from 20, 140, and 150 s acquisition were similar and did not differ significantly from those obtained from ~30 min acquisition (Table 4.2).

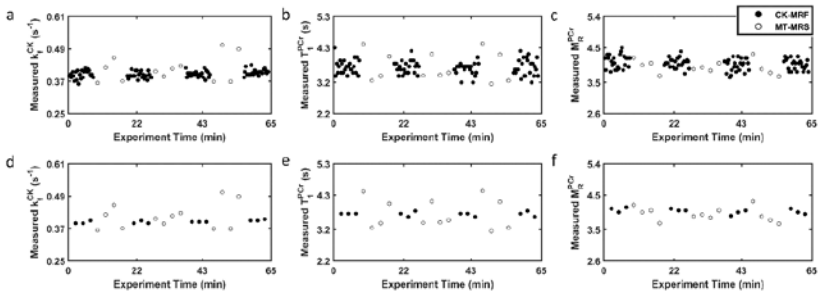

Figure 4.8. Repeated parameter measurements for reproducibility assessment. Sequentially acquired CK-MRF (filled circles) and MT-MRS (open circles) measurements during a data collection session are shown. **a-c.** k_f^{CK} (a), T_1^{PCr} (b), and M_R^{PCr} (c) estimation obtained from single-average data for both CK-MRF (20-s acquisition) and MT-MRS (150-s acquisition). **d-f.** k_f^{CK} (d), T_1^{PCr} (e), and M_R^{PCr} (f) estimation obtained from 7 signal averages for CK-MRF (140-s acquisition) and single average for MR-MRS (150-s acquisition).

Table 4.2 – Estimated Parameters in Reproducibility Study

		T_{acq} (s)	k_f^{CK} (s^{-1})	T_1^{PCr} (s)	M_R^{PCr}
CK-MRF versus MT-MRS	MT-MRS	150	0.40 ± 0.04	3.53 ± 0.44	4.22 ± 0.38
	CK-MRF (1 avg)	20	0.38 ± 0.03	3.57 ± 0.25	4.17 ± 0.25
	CK-MRF (7 avg)	140	0.38 ± 0.02	3.57 ± 0.13	4.16 ± 0.19
CK-MRF versus FAST	FAST	20	0.38 ± 0.11	2.72 ± 0.34	4.27 ± 0.34
	CK-MRF	20	0.39 ± 0.02	3.66 ± 0.21	4.13 ± 0.19

To separate the effects of inter-animal variations, the coefficient of variation (CV) for each parameter was calculated for each animal (Figure 4.9). Average CV of k_f^{CK} from 20-s CK-MRF acquisition was 42% of the size of the CV from 150-s MT-MRS acquisition ($p<0.05$, Figure 4.9a). With equal acquisition time, the CV of k_f^{CK} estimated by CK-MRF further reduced to 26% of the CV by MT-MRS. The CV of T_1^{PCr} and M_R^{PCr} measured by CK-MRF were also significantly smaller than by MT-MRS for both 20-s and 140-s acquisition (Figure 4.9b-c). Finally, the CV of parameters measured by FAST was 4 to 10 times larger than that generated using CK-MRF ($p<0.05$, Figure 4.9d-f).

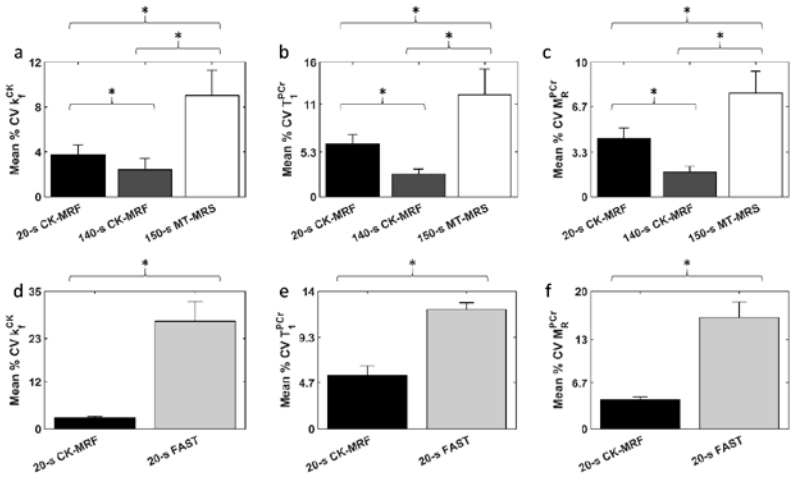

Figure 4.9. Reproducibility of parameter estimation. Coefficient of variation (CV, defined as SD divided by the mean of the measurements) was compared between CK-MRF and MT-MRS methods (a-c) and between CK-MRF and FAST methods (d-f), for parameters k_f^{CK} (a, b), T_1^{PCr} (c, d), and M_R^{PCr} (e, f). Acquisition times denoted represent time spent for a single measurement, including all signal averages but excluding dummy and control scans. Column height and error bars represent mean and SD of CV across animals. All comparisons are statistically significant ($p<0.05$).

Discussion

In this chapter, a novel ^{31}P CK-MRF method to measure CK metabolism based on the MRF framework has been proposed. Simulation studies were used to characterize the sensitivity of CK-MRF measurements to several potential sources of errors. The accuracy and reproducibility of the CK-MRF method was evaluated *in vivo* against conventional methods. Previously, it has been shown in ^{31}P spectroscopic imaging that bSSFP-based approach offers a high gain of SNR per unit time with preserved coherence of magnetization[32]. In the current study, a

bSSFP-type pulse sequence was used with a unique RF and acquisition scheme. With the flexibility of the MRF framework, an interleaved saturation and acquisition scheme was used to generate MT-modulated signal evolution, and the MT effect was further enhanced by the use of a bSSFP-like acquisition that allowed the history of signal evolution to be preserved throughout data acquisition. In addition, the combination of inversion recovery and saturation transfer also allowed greater separation between dictionary entries. As a result, the CK-MRF method showed improved acquisition time and reproducibility for quantification of CK rate, as demonstrated by in vivo experiments.

It is worth noting that acquisition time and reproducibility must be considered together when evaluating the efficiency of a method. In the current study, the CK-MRF method was able to measure k_f^{CK} in vivo in 20 s with a coefficient of variation of only 3.7%. Compared to the MT-MRS method, this demonstrated both an improvement in measurement reproducibility (CV for k_f^{CK} of 3.7 versus 9% for CK-MRF and MT-MRS, respectively), as well as a reduction in acquisition time (20 s versus 150 s for CK-MRF and MT-MRS, respectively). Although acquisition parameters for MT-MRS used in the current study were not optimized, it is unlikely that its acquisition time can be significantly reduced without compromising the reproducibility. The reproducibility of CK-MRF was also benchmarked in the context of equal acquisition time. CK-MRF also showed significantly reduced CV in k_f^{CK} quantification with the same acquisition time when compared to MT-MRS and FAST methods. Acquisition time for conventional MT methods can be further

reduced by using a fixed T_1^{PCr} value[16,31], which was not investigated in the current study. Future investigation comparing these approaches is warranted.

The increased acquisition efficiency of CK-MRF may also enable spatially localized CK measurement. Spatial localization is a long-standing challenge for conventional MT-MRS methods due to the additional SNR penalty for spatial encoding. Using CK-MRF, more signal averages can be achieved within the same acquisition time. Furthermore, unlike most conventional MT-MRS methods, CK-MRF data are acquired using spectrally selective excitation, which has the advantage of allowing spatial encoding to be performed using imaging methods rather than the more time-consuming CSI methods. A previous study using conventional MT-MRS method in combination with spectrally selective excitation has demonstrated feasibility of k_f^{CK} mapping on a 7T clinical system in less than 60 min[41]. CK-MRF combined with spatial encoding may allow further reduction of the acquisition time.

The baseline k_f^{CK} and PCr-to-ATP ratio (M_R^{PCr}) measured in this work are consistent with those reported previously[42]. The slight decrease in M_R^{PCr} after two rounds of IR is also consistent with a previous study in pig muscle subject to three rounds of IR[43]. In conjunction with the decrease in PCr, an increase in post-IR k_f^{CK} was detected by both MT-MRS and CK-MRF methods. While this increase has not been reported previously, it might be a result of the decreased PCr concentration

or concentration changes in other high-energy phosphate metabolites such as ADP. Previously, McFarland et al observed increased k_f^{CK} with decreased PCr content in stimulated perfused soleus muscle[44], which was attributed to the concurrent increase in ADP concentration based on the Michaelis-Menten kinetics[45,46]. However, studies using longer ischemic duration have observed decrease in both k_f^{CK} and PCr concentration[47,48]. The mechanisms and the relationship between ischemia duration and subsequent changes in creatine kinase kinetics need further investigation.

In the current study, several parameters, including $T_1^{\gamma\mathrm{ATP}}$, $T_2^{\gamma\mathrm{ATP}}$, T_2^{PCr}, $\omega^{\gamma\mathrm{ATP}}$, linewidth, and B_1, used fixed values instead of being matched to reduce computation time and memory requirements. Insensitivity to these error sources is an important quality for pulse sequence design for two reasons. First, it allows accurate measurement of the matched parameters without precise pilot measurements of the fixed parameters. Second, it requires only a single dictionary to be computed for a particular study, despite minor inter-subject and inter-measurement variations such as in metabolite T_2 values[49]. Robustness to B_1 errors is of particular importance as many ^{31}P MRS studies are performed using surface coils with significant B_1 inhomogeneity. Our simulation results show that errors in k_f^{CK} measurement was less than 3% in the presence of ±50% error in B_1 flip angle. Further, in vivo measurements of k_f^{CK} also showed strong agreement with both MT-MRS and FAST measurements. However, our current study was

Commented [cw1]: R4.10

performed using a saddle coil. Whether this robustness to B_1 miscalibration is sufficient for measurements using surface coils needs further investigation.

Commented [cw2]: R3.4, R3.11, R3.15, R3.16

CK-MRF also showed tolerance to physiological variations such as P_i exchange rate with γATP. Simulations using values associated with resting rat skeletal muscle[40] showed no detectable errors. While P_i exchange rates with ATP may be higher in other organs or physiological conditions, simulations showed less than 5% error in k_f^{CK} measurement even with over a fivefold increase in either the rate of P_i to ATP or the concentration of P_i, compared to that of resting skeletal muscle.

However, errors in fixed parameter $T_1^{\gamma ATP}$ do have the potential to cause significant errors in k_f^{CK} measurement, and this error is approximately 30% the size of the $T_1^{\gamma ATP}$ error. Moreover, in vivo measurement of $T_1^{\gamma ATP}$ is nontrivial, especially for the current CK-RF method. This is because the magnetization of αATP and βATP is never disturbed in the current method, hence, $T_1^{\gamma ATP}$ must also include the effects of NOE couplings. While this may be addressed by expanding the Bloch-McConnell equation to include these effects through additional exchanging pools[36], substantial validation of such an approach would be needed to evaluate its potential accuracy and robustness.

Another limitation of the proposed CK-MRF method is that the data acquisition scheme using selective RF excitation only samples PCr and γATP magnetization.

As result, other information that are typically available in conventional ^{31}P spectra, such as pH and PDE and ADP concentrations, cannot be obtained from CK-MRF data. Hence, if such information is desired, the acquisition of a conventional ^{31}P spectrum should also be included.

Commented [cw3]: R4.23, R4.25

Continuous wave RF pulses were used in the CK-MRF method to perform selective saturation. The spillover effect on PCr was partially accounted for by applying contralateral saturation pulses. Simulations show that the errors introduced by such an approach were power dependent, and the errors were comparable to those observed in conventional MT-MRS method. The observed 3.6% underestimation in k_f^{CK} by CK-MRF is consistent with the bias expected between the two methods for a saturation power between 11 to 14 Hz. With improved mapping of the B_1 field, these errors may be correctable by using explicit methods[50], or by building saturation power into the dictionary as an additional fixed or matched parameter. Alternatively, continuous wave RF may be replaced by another saturation pulse such as BISTRO[51] with reduced spillover effect.

To reduce computation time and memory requirements, the current dictionary choice of matched parameters and parameter resolution was selected as an acceptable tradeoff between potential errors size and dictionary computation and memory size. Simulation results showed that the current dictionary resolution resulted in the nearest-neighbor match for matched parameters, with the exception

of T_1^{PCr}, where the next-nearest-neighbor may also be matched. This result implies that the accuracy of parameter match may be further improved by using a dictionary with a finer resolution.

In conclusion, the MRF framework was able to accurately and quickly measure creatine kinase metabolism *in vivo*. CK-MRF was able to significantly increase measurement reproducibility compared to the conventional ^{31}P MT-MRS method while exhibiting robustness to several error sources. The improvement in measurement efficiency may be leveraged in several ways, such as more accurate measurements made in equivalent experimental time, or reduced experimental time with equivalent measurement accuracy, allowing for new applications of ^{31}P studies on tissue metabolism.

Chapter 5. Quantification of ATPase Metabolism by ^{31}P Spectroscopic Magnetic Resonance Fingerprinting

Introduction

The reactions of ATP utilization and regeneration are central components of cellular metabolism. While creatine kinase (CK) plays a large role in buffering ATP during transient mismatches between supply and demand, mitochondrial ATP synthase is the key actor that supplies the majority of ATP to drive the rest of the reactions fundamental to life in humans. The existence of a fast, robust, and sensitive method capable of measuring this central component of metabolism would be of great benefit as a clinical diagnostic, in the evaluation of therapeutics, and in the study of physiology and pathophysiology.

Several phosphorus-31 magnetic resonance spectroscopy (^{31}P MRS) methods, using magnetization transfer (MT-MRS) techniques, have been previously proposed that are sensitive to ATPase metabolism[13,23–30,52,53]. The use of ^{31}P MT-MRS for the measurement of adenosine triphosphate (ATP) turnover has been explored *in vitro* in cells[54,55] and perfused organs[56–58], and *in vivo* in laboratory animals[27,59–63] and humans[64–70]. Results of these methods indicate that P_i to ATP flux in skeletal muscle is modulated in clinical disease states such as diabetes that may reflect alterations in metabolism[24]. However, due to the inherent low sensitivity of ^{31}P MRS combined with the low concentration of inorganic phosphate (P_i), measurement of ATP synthesis rate typically requires prohibitively long

acquisition time to achieve satisfactory signal-to-noise ratio (SNR) and adequate accuracy. Traditionally, measurements of ATPase ~60 min on a human with a high field clinical system, and 4-6 hours on small animal ultrahigh field systems[24]. To address this, significant research effort has been dedicated towards optimization of acquisition parameters to maximize signal sensitivity and reduce scan time[14,16,31,36,71]. Despite these efforts, a combination of disparate inter-study results and concerns of the interpretability of these results have raised serious concerns about the utility of the method[24,52,72]. These concerns stem fundamentally from the limitations in speed, robustness, and sensitivity of the available ^{31}P MT-MRS methods. Thus, a new approach is warranted.

In contrast to the confined and restricted steady-state sampling pulse sequence design of the MT-MRS methods, the magnetic resonance fingerprinting (MRF) framework provides flexibility in pulse sequence design. This freedom can be leveraged to design novel pulse sequences that favor speed, robustness, and sensitivity. The MRF framework has been used to great success in this regard in ^{1}H magnetic resonance imaging methods. In Chapter 3, the MRF framework was successfully adapted to ^{31}P MRS to map T_1 relaxation time of phosphorus metabolites. Then, in Chapter 4, the ^{31}P spectroscopic MRF method was extended into the CK-MRF method to sensitively, rapidly, and robustly quantify CK metabolism compared to MT-MRS methods. However, the CK-MRF method was not sensitive to other physiological information that may be obtained in ^{31}P signals. The goal of this chapter is to expand upon the previously developed methods to

measure not only CK metabolism, but also ATPase metabolism and pH. This new method, the MT-MRF method, while sensitive to all of these phenomena, seeks to improve the robustness of measurements associated with ATPase metabolism.

While the principles underlying ^{31}P based measurement of CK metabolism and ATPase metabolism are similar, under baseline physiology conditions, ATPase metabolism is 1-2 orders of magnitude slower than CK metabolism. Since both CK and ATPase modulate ATP supply, the signals measured to quantify CK and ATPase can potentially become interdependent. In Chapter 4, it was shown that including the effects ATPase metabolism resulted in negligible errors during quantification (Figure 4.4) because CK's higher flux rate dominates ATPase's potential effect. Unfortunately, the reverse is true for ATPase metabolism quantification; in order to accurately measure ATPase metabolism, CK metabolism must be simultaneously quantified. As a result, the number of tissue parameters that must be simultaneously quantified is greatly increased. The simulation generated dictionary template matching method that was used in Chapters 3 and 4, while applicable in theory to MT-MRF quantification, were untenable in practice due to the dimensionality of the problem. To illustrate this, the dictionary generated for CK-MRF quantification consisted of the predicted time course signal evolution fingerprint for every permutation of four specific tissue properties. Each tissue property was simulated at ~30 possible dictionary values, resulting in a dictionary with $6x10^5$ entries, occupying 3 GB of computer memory. By extension to the minimum eight tissue properties necessary to describe the unique MR signal time

courses sensitive to both CK and ATPase metabolism, a dictionary for ATPase quantification would be exponentially larger. A dictionary with similarly resolution to quantify the ATPase would require $4x10^{11}$ entries, occupy two petabytes of memory and require $6x10^{5}$ fold longer computation time to generate. For these reasons, an iterative parameter estimation approach was implemented in lieu of the established dictionary approaches.

In this chapter, we present the novel MT-MRF for ATPase metabolism, based from the MRF framework. The method takes advantage of the flexibility of pulse sequence design to uniquely encode tissue properties related to metabolite exchange among ATP, P_i, and PCr. This encoding scheme, combined with a novel data sampling strategy, we hypothesized would enable accurate and more efficient quantification of tissue properties related to ATPase mediated metabolism, including rates of chemical exchange, metabolite concentrations, and T_1 relaxation time. Robustness of the MT-MRF method to potential error sources was examined *in vivo*. Accuracy and precision of the MT-MRF method was examined *in vivo*. Due to limited conclusiveness of *in vivo* accuracy and precision studies due to inherent low SNR, these studies were supplemented by Monte Carlo simulation studies.

Methods

Pulse Sequence Design

The MT-MRF pulse sequence, shown in Figure 5.1a, was designed to encode metabolism related magnetization transfer between phosphate metabolites among γATP, PCr, and P_i (inset in Figure 5.1b). The pulse sequence comprised of three modules. The first module was designed to primarily encode MT from γATP to P_i. This was achieved by a selective inversion pulse on P_i resonance, followed by data acquisition after a 1.0 s delay. The second module followed the first, and was designed to encode MT from P_i to γATP. This was achieved by applying a selective inversion of both PCr and γATP resonances prior to data acquisitions. The third module provided further encoding of MT via ATP synthase, as well as encoding of MT via creatine kinase, through selective γATP saturation.

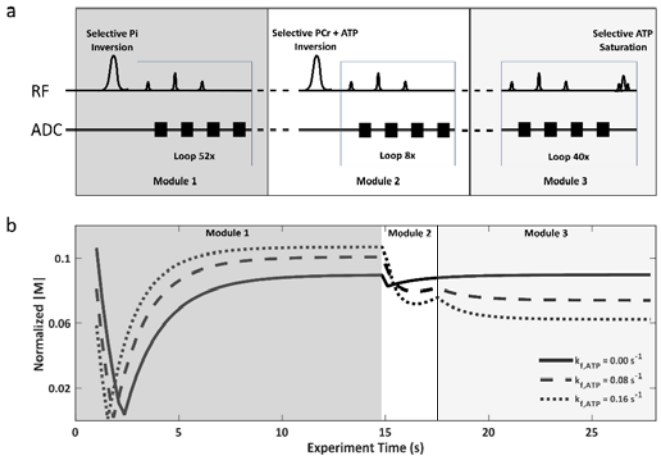

Figure 5.1. Sequence design. **a**. Schematics of the 3 modules used during MT-MRF pulse sequence; **b**. the simulated P_i signal evolution using three different values of rate constant k_f^{ATP}.

Similar to the previous ^{31}P spectroscopic MRF pulse sequences, the pulse sequence for MT-MRF used a bSSFP-type pulse sequence structure[32] with ramped flip angles[33] for high SNR efficiency. However, several changes were made to compensate for the ~4 fold shorter T_2 value of P_i as compared to PCr. Specifically, to reduce the magnetization lost to T_2 relaxation, the repeated blocks used for data acquisition consisted of only four RF excitations followed by a data acquisition (ACQ), with respective repetition times (TR) of 7.7, 7.7, 7.7, and 250 ms. This reduced the fraction of experiment time dedicated to sampling from ~20% in the CK-MRF method to only ~10% in the current MT-MRF method. Furthermore, to shorten the required TR duration while maintaining an acceptable sampling window per ACQ, RF excitations used 1.11 ms duration Gaussian-shaped pulses centered at P_i resonance rather than the 4 ms pulse durations used for the CK-MRF method. As a result, each acquisition window could span 5.2 ms during which 70 data points were acquired. This acquisition scheme led to a spectral resolution of 192 Hz. Finally, the flip angle of each excitation per block was 15°, -30°, 15°, and 0°, respectively. This reduced the 35° average FA for excitation used in the CK-MRF method to only 15° in the current method.

Three modules of acquisition blocks were used to encode sensitivity to both CK and ATPase metabolism. Module 1 consisted of 52 blocks, acquiring a total of 208 FID signals. Module 2 consisted of 8 blocks, acquiring a total of 32 FID signals. Finally, module 3 consisted of 40 blocks with 160 FID signals. Finally, 6 seconds

was allowed for partial magnetization recovery before beginning the next signal average. Including all delays, a total of 34 s was required for one signal average. γATP saturation in module 3 was achieved using low power continuous wave saturation pulse centered on γATP resonance. Saturation pulses were applied after the fourth ACQ was acquired in each block. To control for possible spillover on P_i, the saturation pulses was applied symmetrically downfield of P_i resonance during modules 1 and 2.

Figure 5.1b shows the simulated magnitude signal of P_i using three different rate constant (k_f^{ATP}) values. For visual clarity, only the signal from the second FID signal measured from each acquisition block is shown. The signal evolution across the three sections of data acquisition showed a biphasic change that reflected the impact of control vs selective saturation of γATP on P_i magnetization. In module 1, magnetization transfer from γATP to P_i caused P_i signal to recover more quickly than T_1 relaxation alone. A faster rate constant led to faster P_i recovery. In modules 2 and 3, the P_i to γATP flux caused P_i signal to decrease, and the decrease occurred more quickly with a faster rate constant. Compared to conventional T_{1app}-based MT methods with a monophasic signal evolution, this biphasic signal evolution allowed the estimation of the rate constants to be more robust to T_1 estimation errors.

Fingerprint Simulation

Signal time courses, i.e. fingerprints, were simulated by solving the modified Bloch-McConnell equations for three exchanging phosphate metabolites (inset in Figure 5.1b). Details of the spin exchange model are described in Appendix D. A total of 14 tissue properties were accepted as input parameters for simulation. These parameters included the forward rate constants of ATP metabolism via creatine kinase and from ATPase (k_f^{CK} and k_f^{ATP}), the T_1, T_2, and ω (chemical shift) values for PCr, γATP, and P_i (T_1^{PCr}, $T_1^{\gamma\mathrm{ATP}}$, T_1^{Pi}, T_2^{PCr}, $T_2^{\gamma\mathrm{ATP}}$, T_2^{Pi}, ω^{PCr}, $\omega^{\gamma\mathrm{ATP}}$, ω^{Pi}), and the concentration ratios of PCr-to-ATP and P_i-to-ATP (M_R^{PCr} and M_R^{Pi}). Finally, B_0 inhomogeneity was accounted for by a linewidth parameter (LW) as described in Chapter 4.

MRF Data Processing

MRF data, from both simulation and experimental studies, was processed using in-house developed MATLAB code. First, a Gaussian apodization function was applied to each FID signal to reduce spectral leakage. Following Fourier transform, the spectra were phase corrected and the time courses of the signals from the 3 spectral bins corresponding to P_i, PCr, and γATP resonances were used in the parameter matching process described below.

Parameter Estimation

To estimate the set of tissue properties associated with each measured fingerprints, an iterative parameter optimization scheme was used. The scheme

used the Nelder-Mead simplex approach to find the set of simulation input parameters that generated the highest consistency between each measured fingerprint and simulation predicted fingerprint. The objective function for iterative estimation was the magnitude of the l_2-normalized inner product between the measured and simulated fingerprints. Of the 14 input parameters required for fingerprint simulation, a total of nine parameters were estimated by the algorithm, while the remaining 5 were fixed. Estimated parameters included the two forward rate constants (k_f^{CK} and k_f^{ATP}), the two concentration ratios (M_R^{PCr} and M_R^{Pi}), the T_1 relaxation time of PCr and P_i (T_1^{PCr} and T_1^{Pi}), and the chemical shift of PCr, γATP, and P_i (ω^{PCr}, $\omega^{\gamma\mathrm{ATP}}$, ω^{Pi}).

To reduce computation time, the iterative parameter estimation process was performed in five steps. At each step, a subset of the nine estimated parameters were optimized, while the remaining estimated parameters were held fixed. First, the subset of tissue parameters associated with the resonance frequencies for the three metabolites (ω^{PCr}, $\omega^{\gamma\mathrm{ATP}}$, ω^{Pi}) were optimized. Next, the subset of parameters associated with CK metabolism (k_f^{CK}, M_R^{PCr}, and T_1^{PCr}) were optimized. This was followed by the estimation of the subset of parameters associated with ATPase metabolism (k_f^{ATP}, M_R^{Pi}, and T_1^{Pi}). Following that, the subset of CK metabolism parameters and the subset of ATPase metabolism parameters were both refined by separately repeating the optimization of both parameter subsets.

For each measured fingerprint, parameter estimation was performed twice, using two different sets of algorithm initial values. The output of the parameter estimation process for each set of initial values was a complete set of estimated tissue properties, as well as the corresponding most consistent "matched" fingerprint evolution. Between the two sets of returned tissue properties, the set with greater inner product metric judged consistency with measured fingerprint was returned as the final match. Initial values for tissue metabolite resonance frequencies and linewidth parameters were taken from an initial calibration spectrum. Initial values for the remaining estimated parameters were randomly drawn. The remaining fixed parameters: T_2 relaxation time of P_i, γATP, and PCr (T_2^{PCr}, $T_2^{\gamma\mathrm{ATP}}$, T_2^{Pi}) were assumed using values measured from pilot experiments.

Conventional Inversion-Recovery Method

The conventional inversion-recovery MT (MT-IR) method was used for all comparison studies. The same set of MT-IR acquisition parameters was used for both simulation studies and experimental validations. Specifically, after the inversion pulse, data acquisition was performed after one of seven variable durations of selective γATP saturation (0.1, 0.6, 1.2, 2.5, 5, 10, and 18 s) was applied. An inter-scan delay of 18 s was used to allow complete magnetization recovery. Each conventional time domain FID consisted of 2148 data points acquired with a 74 μs dwell time. Control saturation spectra was acquired using contralateral selective saturation to γATP relative to P_i resonance.

Simulation Studies

To evaluate the robustness of parameter estimation to experimental noise, Monte Carlo simulation studies were performed. Multiple noisy fingerprint signal evolutions were generated by adding random complex Gaussian noise to simulated time domain FID signals associated with a set of test estimation parameters. Measurement precision was assessed by the distribution of estimated parameters across noisy fingerprints. For comparison, equivalent noise was added to the simulated time domain conventional MT-IR data. Simulated noisy MT-IR data was quantified by conventional means, and the distribution of estimated parameters were similarly assessed. Two sets of Monte Carlo comparisons were performed, using different noise levels. A low level and a high level of SNR were selected to be representative of *in vivo* experiments using total data acquisition times equivalent to 30 and 100 min, which resulted in SNR levels of 7 and 12, respectively, for P_i signal within a conventional spectra. Each set of Monte Carlo comparisons between MT-MRF and MT-IR methods used 72 and 2000 simulations, respectively.

The impact of errors in fixed simulation parameter values on parameter estimation was evaluated in a simulation study. For each of the five fixed parameters used in the simulation, a study was performed to evaluate its impact on the quantification of the nine estimated parameters. In each study, a series of simulated fingerprints was generated where one fixed parameter was varied and the remaining 13 simulation input parameters were held constant. The fixed parameter examined

in each study was varied through a range of 10 to 200% of its expected value. The result of parameter estimation for each parameter was then assessed against the true input value. The impact of consistent B_1 scale error was similarly investigated. Simulated evolutions were generated using a range of 10-200% of nominal B_1. Following parameter matching of the simulated evolutions, the effect of B_1 on each of the matched parameters was quantified.

In Vitro Study

Due to the low SNR and large number of potential confounders inherent to *in vivo* experiments, an *in vitro* study, using a stable, non-exchanging phantom, was performed to assess consistency between simulation and measured data. MT-MRF and MT-IR data was acquired on a solution phantom composed of 150 mM PCr, 100 mM ATP, and 60 mM K_2HPO_4 using acquired with 20 signal averages. The agreement between estimated parameters from both methods was assessed. All experimental studies were performed on a horizontal 9.4T Bruker Biospec scanner (Bruker Biospin Co., Billerica, MA, USA).

In Vivo Study

Four-month old male Sprague-Dawley rats (n=7) were anesthetized with 1.5-2.5% isoflurane and positioned laterally in a cradle. The left hindlimb was secured within an in-house built 20-mm ^{31}P saddle coil placed within a ^{1}H volume coil and at the isocenter of the magnet. Body temperature was maintained above 35°C by blowing warm air into the scanner via a feedback control system (SA Instruments,

Stony Brook, NY). The respiratory rate was maintained at 30 breaths per minute by adjusting the anesthesia level. The animal protocol was approved by the Institutional Animal Care and Use Committee of Case Western Reserve University.

After standard MRS calibrations, MT-MRF and MT-IR data were acquired in an interleaved fashion. Calibration steps included PRESS localized shimming performed and the acquisition of a conventional ^{31}P spectra to determine the linewidth and metabolite resonance frequencies used during MT-MRF parameter estimation method. Data for MT-MRF and MT-IR methods were both acquired for 100 minutes. This resulted in a total of 180 and 30 acquired repetitions of MT-MRF and MT-IR methods, respectively.

Acquired MT-MRF and MT-IR data were averaged in post-processing to yield the equivalent of 30-min and 100-min data acquisitions. The measurement agreement between MT-MRF and MR-IR methods across animals was assessed for 100-min data acquisitions. Measurement precision was compared between methods for both 30-min and 100-min data acquisitions. Additionally, pH was assessed as

$$pH = 6.88 + \log\left(\frac{\Delta\omega^{PCr-Pi} - 3.55}{5.6 - \Delta\omega^{PCr-Pi}}\right)$$

where $\Delta\omega^{PCr-Pi}$ is the chemical shift difference between PCr and Pi resonance frequencies obtained by both MT-MRF and MT-IR methods.

Statistical Methods

Comparison of the mean values of the estimated parameters by MT-MRF and MT-IR used unpaired Student's t-test for simulation studies and paired Student's t-test for *in vivo* studies. Bland-Altman analysis was used to assess agreement between 100-min *in vivo* MT-MRF and MT-IR measurements. Comparison of the variations in the estimated parameters, i.e., precision, was performed using two-sample F-test for equal variance. $P<0.05$ was considered statistically significant. P_i-to-ATP flux was calculated by multiplying the estimated rate constant k_f^{ATP} with the estimated P_i-to-ATP ratio (M_R^{Pi}), assuming an ATP concentration of 25.1 μm/g dry weight[60]. Fixed parameter T_1 relaxation time of γATP ($T_1^{\gamma\mathrm{ATP}}$) accounted for NOE contributions from αATP and βATP[36].

Results

Simulation Studies

The results from the simulation study examining the sensitivity of the MT-MRF method to random noise is shown in Figure 5.2. Representative noisy P_i time course signal evolution fingerprints, corresponding to low and high SNR, are shown in Figures 5.2a and 5.2b, respectively. The estimation-process-derived noise-free fingerprints, corresponding to the set of returned estimated parameters, are shown overlaid atop the noisy fingerprints. For the sake of visual organization, the four ACQs from each block of acquisitions are shown in different colors. Substantial noise related fluctuations in time course signals were present within signal fingerprints. However, simulation derived present in simulation fingerprints.

The smoothness of the estimated fingerprint, across each of the four ACQs, increased signal redundancy such that the impact of an individual noisy time course data point.

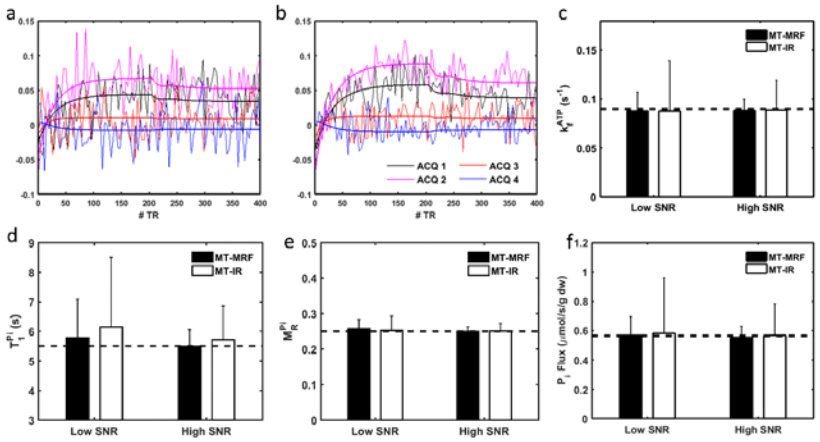

Figure 5.2. Monte Carlo simulation of the effects of measurement noise on parameter estimation. **a-b**. Representative fingerprint simulation at low (a) and high (b) SNR, with the matched, noise-free fingerprints overlaid. **c-e**. Parameter estimation of k_f^{ATP} (c), $\mathrm{T}_1^{\mathrm{Pi}}$ (d), M_R^{Pi} (e), and P_i-to-ATP flux (f) by MT-MRF and MT-IR. Dotted lines indicate the true parameter values used in simulation.

Figures 5.2c-2f summarizes the effects of measurement noise on the accuracy and robustness of parameter estimation of the MT-MRF compared to conventional MT-IR. The input parameters used to generate noise free time course data before the addition of complex noise are shown as dotted lines. At both low and high SNR levels, no significant differences were detected between MT-MRF and MT-IR

method measurement means for tissue properties k_f^{ATP}, T_1^{Pi}, M_R^{Pi}, or the calculated P_i-to-ATP flux. However, MT-MRF showed significantly improved precision, characterized by smaller error bars in comparison to the MT-IR method, for all three estimated tissue properties at both SNR levels ($p<0.0001$). Estimation of tissue properties associated with CK metabolism, i.e., k_f^{CK}, T_1^{PCr}, PCr-to-ATP ratio, and PCr-to-ATP flux, was also similar between the MT-MRF and MT-IR methods (Figure 5.3)

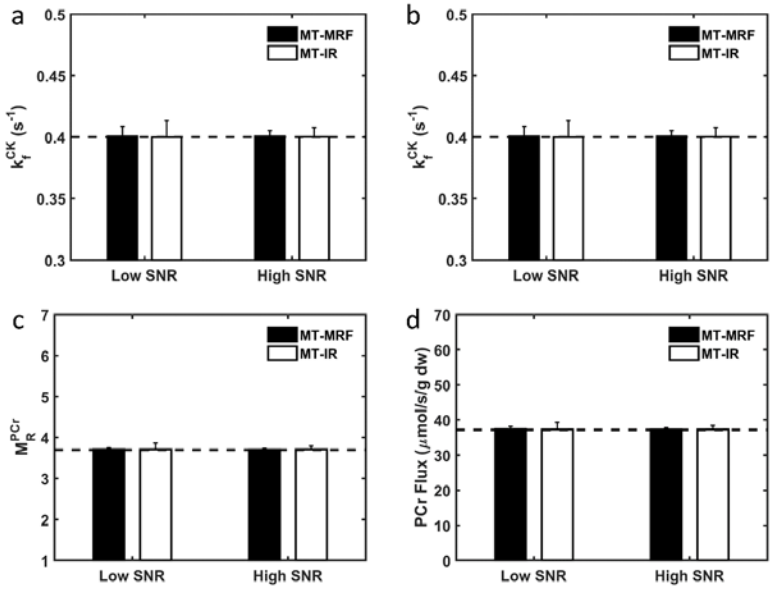

Figure 5.3. Results of Monte Carlo simulation comparing MT-MRF matching of k_f^{CK} (a), T_1^{PCr} (b), M_R^{PCr} (c), and PCr-to-ATP flux (d) against the conventional MT-IR method. Dotted lines indicate the true parameter values used in simulation.

Figure 5.4 shows the effects of variations in fixed input parameters on the accuracy of the estimated parameters. The fixed parameters included the T_1 of ATP ($T_1^{\gamma ATP}$), the T_2 of P_i, ATP, and PCr (T_2^{Pi}, $T_2^{\gamma ATP}$, and T_2^{PCr}), spectral linewidth (LW), and flip angle (B_1). Estimation of T_1^{Pi} was relatively robust to all the unmatched parameters (Figure 5.4b). The estimation of k_f^{ATP} (Figure 5.4a) and M_R^{Pi} (Figure 5.4c) was sensitive to B_1 scale errors. A >25% scale error in B_1 led to an estimation error of >20% for k_f^{ATP}, while a >30% error in B_1 calibration led to an estimation error of >20% for P_i-to-ATP ratio. For the rest of the fixed parameters, the estimation error of k_f^{ATP} was <20% if the simulation fixed parameter was within 40% of its experimental value. Estimation of M_R^{Pi} was sensitive to the T_2 of P_i when its value used in parameter matching was less than 60% of the true value. Calculated from the matched k_f^{ATP} and M_R^{Pi} values, the estimated P_i-to-ATP flux was robust to most errors in the unmatched parameters (Figure 5.4d). The flux measurement was most sensitive to errors in linewidth (LW) where a >30% measurement error led to an estimation error of >20%.

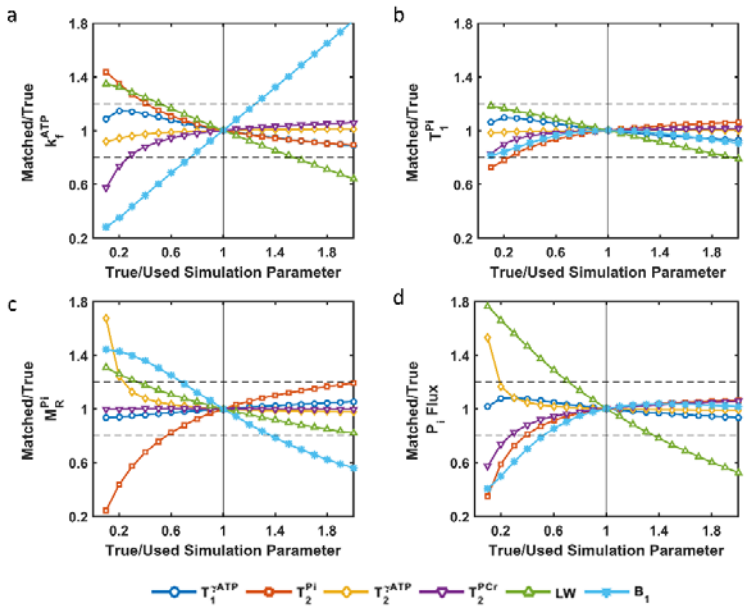

Figure 5.4. Effect of variations in unmatched parameters on the accuracy of parameter estimation of k_f^{ATP} (**a**), T_1^{Pi} (**b**), M_R^{Pi} (**c**), and P_i-to-ATP flux (**d**). Dotted lines indicate 20% error in the estimated parameters.

In Vitro Study

Data acquired from solution phantom are shown in Figure 5.5. Figure 5.5a shows one representative spectrum of the 400 acquired FIDs. Due to the short duration of data acquisition (5.2 ms), the spectral resolution was significantly lower than a conventionally acquired spectrum (top of Figure 5.5a). The L_2-normalized time course signal evolution of P_i, γATP, and PCr, overlaid by their parameter estimation derived match, are shown in Figures 5.5b-d, respectively. The same color scheme

from simulation studies were used to visually organize the signal from the four ACQs within each block.

The different behavior of metabolite time course signal evolution during the three pulse sequence modules can be observed. At the beginning of module 1, selective inversion of P_i resonance inverts P_i magnetization without affecting γATP and PCr magnetization. Prior to the 209th acquired FID signal, selective inversion is applied to γATP and PCr resonance, with no effect on P_i magnetization. Repeated selective saturation applied on γATP resonance, starting from before the 245th FID until the end of measurements, maintain γATP magnetization near zero for the duration of Module 3.

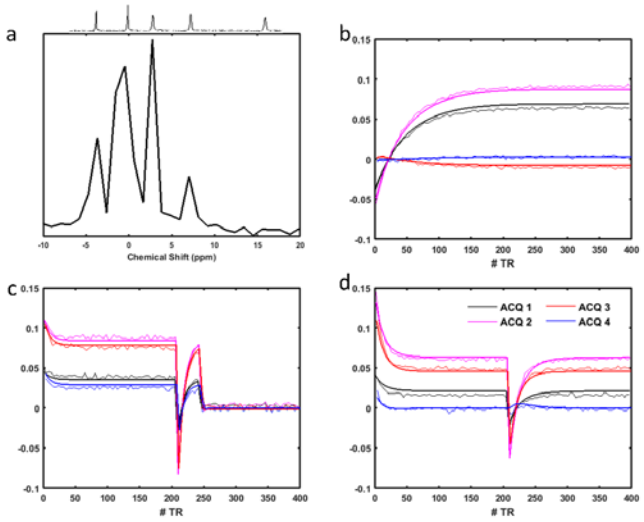

Figure 5.5. MRF signal from phantom study**. a**. Representative spectrum from an MRF acquisition. Top spectrum with high spectral resolution was acquired using conventional method. **b-d**. Measured signal evolutions and their corresponding simulation match for P_i (b), γATP (c), and PCr (d).

In vitro metabolite estimated parameters from the MT-MRF method were in good agreement with the measurements obtained using the conventional MT-IR method. Estimated T_1^{Pi} value was 3.86 s and 3.82 s, while estimated M_R^{Pi} value was 1.36 and 1.32 using MT-MRF and MT-IR, respectively. Both methods estimated the k_f^{ATP} value to be 0.00 s^{-1}, reflecting the absence of enzymes for ATP synthesis in the phantom. Similarly, estimated k_f^{CK} value of 0.00 s^{-1} was obtained by both methods, reflecting the absence of creatine kinase.

In Vivo Study

Figure 5.6 shows the *in vivo* MT-MRF and MT-IR parameter estimation results for ATPase metabolism related tissue properties requiring 100 min acquisition time. A representative time course signal from P_i resonance is shown, overlaid by its parameter estimation derived fingerprint. Figures 5.6b-e show the Bland-Altman plots comparing MT-MRF and MT-IR measurements from each animal for k_f^{ATP}, T_1^{Pi}, M_R^{Pi}, and P_i-to-ATP flux, respectively. The mean difference between the two methods was -0.008±0.02 s^{-1} for k_f^{ATP}, 0.16±0.74 s for T_1^{Pi}, -0.00±0.04 for M_R^{Pi}, and -0.05±0.10 μm/s/g dry weight for P_i-to-ATP flux, respectively. These differences were not found to be statistically significant.

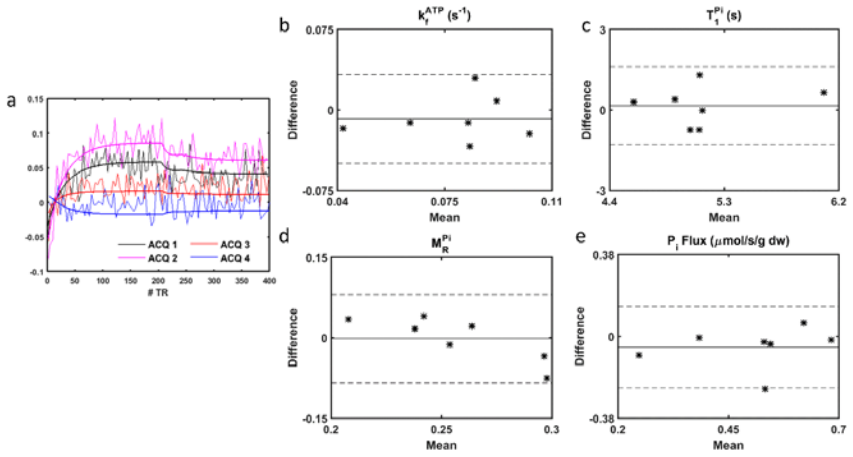

Figure 5.6. *In Vivo* results from 100-min signal averaging. **a.** Representative MRF acquisition with matched evolution overlaid. **b-e.** Bland-Altman plots comparing the matching of k_f^{ATP} (b), $\mathrm{T}_1^{\mathrm{Pi}}$ (c), M_R^{Pi} (d), and $\mathrm{P_i}$-to-ATP flux (e) by MT-MRF and conventional MT-IR methods.

Figure 5.7a shows a representative $\mathrm{P_i}$ fingerprint from 30-min signal averaging overlaid by its simulation matched fingerprint. Figures 5.7b-e show the results of parameter estimation from 30-min data acquisitions. The mean and standard deviation for all *in vivo* measurements are summarized in Table 5.1. These values were within the range of previously reported literature values for resting rat skeletal muscle measured by conventional ^{31}P-MRS methods[24,73]. MT-MRF and MT-IR yielded similar mean values for the estimation of k_f^{ATP}, T_1^{Pi}, and the M_R^{Pi}.

As a result, calculated $\mathrm{P_i}$-to-ATP flux was also similar. Compared to the MT-IR method, the MT-MRF method showed significantly smaller variation in the estimation of k_f^{ATP} and T_1^{Pi} ($p<0.05$), as well as the calculated $\mathrm{P_i}$-to-ATP flux ($p<0.05$).

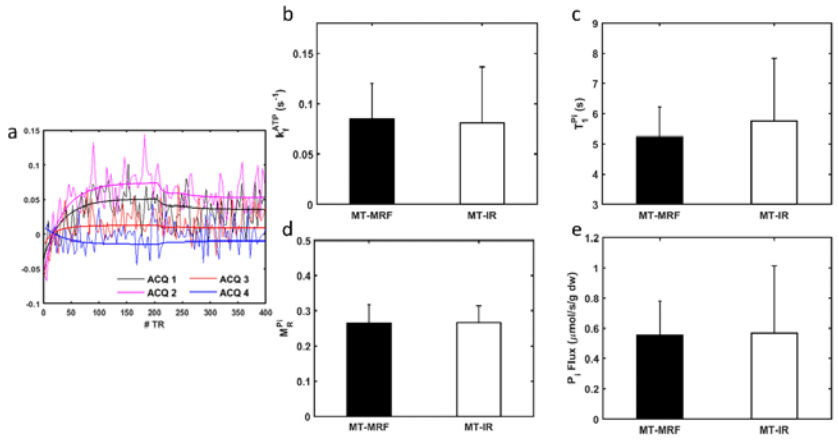

Figure 5.7. *In Vivo* results from 30-min signal averaging. **a.** Representative MRF acquisition with matched evolution overlaid. **b-e.** Comparison of the estimation of k_f^{ATP} (b), $T_1^{\mathrm{P}_i}$ (c), M_R^{Pi} (d), and P_i-to-ATP flux (e) by MT-MRF and MT-IR methods.

	Acq Time (min)	k_f^{ATP} (s^{-1})	T_1^{Pi} (s)	M_R^{Pi}	P_i-to-ATP Flux (μmol/s/g dw)	pH
MT-IR	30	0.081±0.056	5.77±2.07	0.27±0.05	0.57±0.45	7.07±0.09
	100	0.075±0.024	5.70±0.65	0.26±0.02	0.48±0.16	7.04±0.03
MT-MRF	30	0.085±0.035	5.23±1.00	0.26±0.05	0.55±0.23	7.01±0.04
	100	0.083±0.021	5.06±0.52	0.26±0.05	0.53±0.14	7.01±0.03

Table 5.1. Parameter estimation in rat hindlimb with 30-min and 100-min data acquisition.

Results of the estimation of creatine kinase metabolism related parameters are shown in Figure 5.8. Estimated k_f^{CK} was slightly higher than literature reported value for both MT-MRF and MT-IR[60]. Unlike the simulation studies (Figure 5.3), estimated T_1^{PCr} by MT-MRF was significantly higher than that by MT-IR, while

estimation of the $M_R^{\mathrm{PCr}}$and PCr-to-ATP flux by MT-MRF was lower than that by MT-IR.

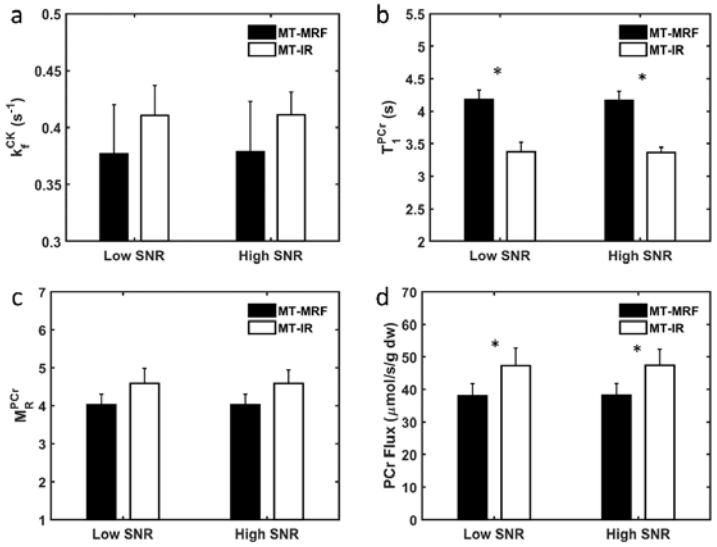

Figure 5.8. Results of in vivo experiments comparing MT-MRF matching for k_f^{CK} (a), T_1^{PCr} (b), M_R^{PCr} (c), and PCr to ATP flux (d) against the conventional MT-IR methods. * denotes P < 0.05.

Discussion

In the current study, we present a novel MT-MRF pulse sequence for the simultaneous measurement of both CK metabolism and ATPase metabolism *in vivo*. The method took advantage of the MRF framework's flexibility in pulse sequence design to encode enzymatic rates. By combining an efficient ATPase encoding scheme with a high SNR acquisition scheme, the MT-MRF method was

able to more precisely measure ATPase metabolism related parameters, k_f^{ATP} and M_R^{Pi}, compared to conventional MT-IR method in both simulation studies and *in vivo* experiments, while still remaining sensitive to CK mediated metabolism parameters, k_f^{CK} and M_R^{PCr}. Additionally, the MT-MRF method was also able to quantify the chemical shift frequencies of PCr, and P_i (ω^{PCr} and ω^{Pi}, respectively), which allowed determination of pH. A constant TR with a regular flip angle scheme was again used in the current study to preserve high SNR across multiple metabolites (Figure 3.2). This pulse sequence design showed improved measurement efficiency over the conventional MT-IR method. Further optimizations of the MT-MRF pulse sequence may yield further improvements.

Table 5.2 summarizes the percent coefficients of variation (CV) found for MT-MRF and CK-MRF studies (Chapter 4) compared to conventional methods. Both MT-MRF and CK-MRF were able to achieve smaller coefficients of variation given an equal amount of experiment time as their respective comparison method, for their respective k_f and T_1 measurements. Unfortunately, MT-MRF was not able to achieve as large of a relative reduction in CV over its respective conventional method as compared to CK-MRF, particularly during *in vivo* studies. One reason for this was because of the influence of physiological variation through the used study design. Due to the time duration of each measurement, the statistically powered reproducibility studies from the same experimental session were not possible. However, MT-MRF Monte Carlo studies, free of physiological variation, still did not achieve as large of an improvement as compared to *in vivo* 2.5 min CK-

MRF measurements. While further optimizations in both methods are likely possible, this difference in relative performance is consistent with the SNR efficiency related to bSSFP type sequences. The T_1 and T_2 times of PCr are ~40% shorter and ~300% longer, respectively, than those of P_i at 9.4 T. The effect of T_1 and T_2 times on SNR in bSSFP-type methods is well characterized in ^{1}H imaging, but has also been shown for ^{31}P CSI[32]. Thus, the potential for acceleration by switching to a bSSFP approach over a conventional pulse-and-acquire method is likely higher for the CK system measurement than the ATPase system. However, T_1 and T_2 times of ^{31}P metabolites are field strength dependent, with substantially longer T_2 relaxation times at lower fields[15,49]. Adaptation of the current methods to lower fields will need to address the smaller chemical shift dispersions at lower fields, but clinically relevant field strengths may allow for greater marginal improvements.

	Study Comparison		k_f (% CV)	T_1 (% CV)	M_R (% CV)	
***In Vivo* ATPase**	**100 min Inter-animal**	MT-IR	32	12	7	
		MT-MRF	26	10	20	
			26	19	-64	**% MRF Improvement**
	30 min Inter-animal	MT-IR	69	36	18	
		MT-MRF	42	19	20	
			65	88	-11	**% MRF Improvement**
***In Situ* Monte Carlo ATPase**	**Simulated noise with high SNR**	MT-IR	31	19	8	
		MT-MRF	12	10	5	
			147	82	62	**% MRF Improvement**
	Simulated noise with low SNR	MT-IR	56	37	16	
		MT-MRF	22	22	11	
			161	66	51	**% MRF Improvement**
***In Vivo* CK**	**30 min Inter-animal**	MT-MRS	6	3	5	
		CK-MRF	6	3	4	
			11	13	13	**% MRF Improvement**
	2.5 min	MT-MRS	9	12	8	
		CK-MRF	2	3	2	
			275	353	318	**% MRF Improvement**

Table 5.2. Summary of coefficients of variations (CV) comparison between conventional MT based methods and MRF framework based methods for metabolic tissue property measurement. CVs measured from equal acquisition time and conditions for both MRF framework method and conventional method are presented pairwise, along with the relative % CV improvement of the MRF method over the conventional method. k_f, T_1, and M_R represents k_f^{ATP} T_1^{Pi}, and M_R^{Pi}, respectively, for ATPase metabolism studies, and k_f^{CK} T_1^{PCr}, and M_R^{PCr}, respectively for CK metabolism studies.

Like the previously proposed MRF based methods, MT-MRF was also shown to be robust to many errors in fixed parameters during estimation process. Interestingly, compared to the CK-MRF method, the MT-MRF method was more robust to errors in fixed parameter $T_1^{\gamma\mathrm{ATP}}$. However, the MT-MRF method was also

found to be more sensitive to B_1 errors. This was acceptable for the non-localized *in vivo* experiments performed in this work, because volume coils with relatively homogenous B_1 profiles were used. However, sensitivity to B_1 may prove challenging for surface coil applications, where larger discrepancies in B_1 homogeneity can be expected. This is a problem shared with other fast quantitative methods[16,24,74]. Future development of this method may seek to either mitigate the B_1 sensitivity, or possibly include it as a matched parameter[75].

An iterative simplex optimization approach was used for parameter estimation. A total of 9 parameters quantified in the current study, which rendered the conventional dictionary-matching approach computationally formidable. The current approach was a compromise between robust parameter estimation and computational efficiency, and allowed the estimation of a set of tissue properties from a single fingerprint in ~20 minutes using single threaded MATLAB on a standard personal computer. However, a limitation of this approach was that it does not guarantee convergence to the global minima, and that two types of error might arise from this approach.

The first error is due to termination tolerances in the algorithm itself, set to $1x10^{-3}$ for all parameters. This tolerance was relatively small compared to the dictionary resolution used previously for the CK-MRF approach. However, similar to T_1^{PCr} quantification using the dictionary approach for CK-MRF (Figure 4.2), true estimation error size is not guaranteed to be bounded by absolute error tolerance

due to the propagation of error between parameters. Contributions of this type of error to the total error should have been captured within the Monte Carlo study.

The second kind of error that the iterative simplex approach may encounter is the possibility of convergence to a local minima rather than the global minima of the solution space. To capture the potential for both types of error, all simulation and experimental fingerprints were estimated using two unique randomly generated sets of algorithm initial values. During Monte Carlo study, estimated k_f^{ATP} differed on average of 0.5% between different initial conditions. However, *in vivo* estimated k_f^{ATP} differed on average of 3.9% between the different initial conditions. The cause of this difference between Monte Carlo and *in vivo* results is not clear. This error was still small compared to the measurement variability of 26% for k_f^{ATP} *in vivo* observed for 100 min measurements. However, future investigations should seek for alternative parameter estimation strategies that may improve robustness to both types of errors.

One limitation of the current study was the non-ideal characteristics of selective saturation pulses. This potentially caused discrepancies in CK metabolism measurements between MT-MRF and MT-IR methods. To improve the accuracy of k_f^{ATP} measurement, control saturation pulses were placed relative to P_i resonance, rather than PCr resonance, during both MT-MRF and MT-IR methods. As a result, spillover effects on PCr were not corrected. This may have led to estimation errors in CK metabolism tissue parameters (Figure 5.8). This spillover

effect is a well-studied source of error for conventional saturation transfer methods, which can result in overestimation of $k_f^{\mathrm{CK}_{76}}$. Compared to PCr-spillover-corrected conventional MT-MRS method measurements, performed in chapter 4, conventional MT-IR measurements in the current study overestimated k_f^{CK} by 9% (0.38±0.02 vs 0.41±0.02 s^{-1}). CK metabolism tissue parameters measured by MT-MRF in the current study showed a similar mean (0.38 ± 0.04 s^{-1}) compared to previous measurements, however they had a significantly larger variation. The reason for this is not clear. Simulation results for the expected effect of PCr spillover during the MT-MRF method are summarized in Figure 5.9.

Simulation results suggested that the MT-MRF method was sensitive to saturation performance for CK metabolism measurements (Figure 5.9a-d). The lack of a measurement bias, but significantly increased measurement variation compared to conventional methods of the *in vivo* experiments suggest that selective saturation performance does not fully explain the discrepancy between measurement methods. However, simulation results also showed that ATPase parameters, particularly P_i-to-ATP flux, were robust to direct PCr spillover effects (Figure 5.9e-h). Future investigation may seek to add additional spillover correction pulses, or directly model the saturation pulse performance during the parameter estimation process.

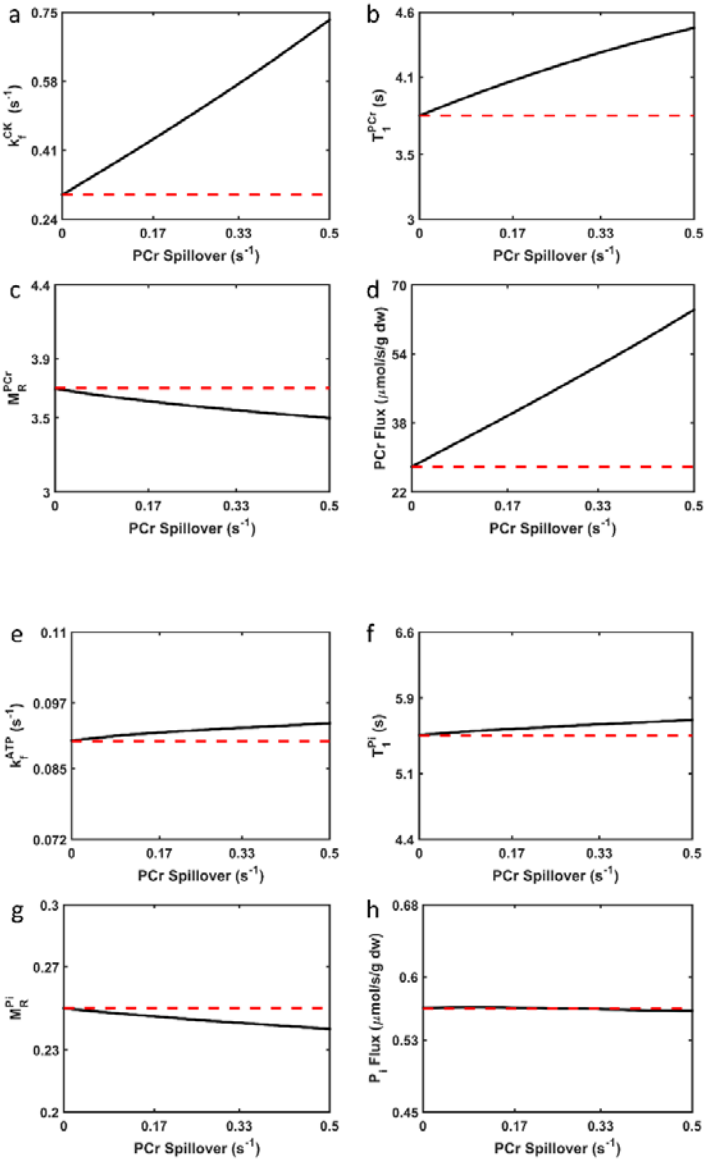
a
b
c
d
e
f
g
h
PCr Spillover (s-1)
PCr Flux (μmol/s/g dw)
Pi Flux (μmol/s/g dw)

Figure 5.9. Estimation of CK and ATPase metabolism related tissue parameters in the presence of uncorrected direct spillover saturation on PCr resonance spillover from the selective γATP saturation pulse. CK tissue parameter k_f^{CK} (a), T_1^{PCr} (b), M_R^{PCr} (c), PCr-to-ATP flux estimation (d) show spillover dependent error. Quantification of ATPase related tissue parameters k_f^{ATP} (e), T_1^{Pi} (f), M_R^{Pi} (g), and P_i-to-ATP flux (h) show greater robustness to CK spillover error. Dotted lines indicate true value of each parameter used for simulation.

In conclusion, we have demonstrated a first step in quantitative spectroscopic measurements of ATPase metabolism using the MRF framework. This work used a novel encoding method of magnetization transfer and combined it with an unconventional sampling method to efficiently measure metabolite exchange kinetics. Using these methods, spectroscopic MT-MRF was able to significantly increase measurement efficiency while retaining robustness to various measurement errors compared to the conventional MT-IR method. This may be leveraged in the future as either improved measurement accuracy for equivalent experimental time, or reduced experimental time with equivalent measurement accuracy, and may enable for new applications for ^{31}P studies on tissue metabolism.

Chapter 6. Conclusions and Future Directions

Conclusions

The ultimate goal in this thesis was to increase measurement efficiency of ^{31}P based metabolic measurements. The hypothesis that novel ^{31}P methods designed in the MRF framework would lead to accurate and more efficient measurements as compared to conventional methods was investigated in three settings. By taking advantage of the flexibility proffered by the MRF framework, high SNR acquisition designs was combined with effective signal encoding techniques to successfully improve the speed and robustness of measurements.

In Chapter 3, the hypothesis that an MRF approach would be able to accurately and more efficiently measure both T_1 relaxation time and relative concentration of multiple ^{31}P metabolites, in the absence of active metabolism, as compared to conventional methods was examined. Simulation experiments showed that the ^{31}P-MRF method, using bSSFP-type acquisitions using ramped flip angles and constant TR, was reliable for quantification of T_1 and M_0 in simulation. Further experiments showed the robustness of the ^{31}P-MRF method to potential experimental conditions. *In vitro* studies confirmed this potential for measurement accuracy, and also demonstrated higher measurement efficiency as compared to conventional ^{31}P IR, for examined metabolites. Despite these promising results, magnetization (MT) effects via chemical exchange were not specifically encoded.

As a result, the developed method could not be validated *in vivo* where the presence of phosphorus metabolism would have interfered with T_1 measurements. However, the results suggest that the ^{31}P-MRF pulse sequence was both SNR efficient and robust to important experimental conditions. Moreover, its blocked design was conducive to the incorporation of additional encoding schemes, with great potential for sensitive measurement of other tissue properties.

In Chapter 4, the hypothesis that specific adaption of the ^{31}P MRF method for CK metabolic measurement would enable accurate and more time efficient measurements of CK metabolism as compared to conventional methods was examined. CK encoding was added to a bSSFP-type pulse sequence successfully to reduce CK rate measurement time while increasing measurement robustness to noise compared to previous methods. The developed CK-MRF method was tested against conventional MT-MRS method in rat skeletal muscle for measurement accuracy under baseline and post ischemia/reperfusion (IR) conditions. Both CK-MRF and MT-MRS methods detected a significant increase in measured CK rate after IR of 13 and 11%, respectively. Measurements for CK rate constant by CK-MRF showed a small but significant bias of -3.6% as compared to conventional MT-MRS method through paired t-test and Bland-Altman analysis. No significant biases were found for the other measured parameters. Reproducibility assessment performed on rat skeletal muscle under resting baseline conditions showed significantly higher reproducibility in measurements for all CK metabolism related parameters using CK-MRF as

compared to MT-MRS and FAST methods. These results showed that CK-MRF was able to more robustly assess CK metabolic rates, perturbations to CK metabolism, showed minimal bias compared to conventional methods, while requiring potentially 7.5x less experimental time as compared to conventional methods. While these results are promising, further studies will necessary to determine if similar results can be achieved in other physiological and pathological conditions. Furthermore, the method will require significant adaptation before being compatible with the lower B_0 field strengths associated with clinically used hardware.

In Chapter 5, the hypothesis that expansion of the previously developed ^{31}P MRF methods to be sensitive to ATPase mediated metabolism would enable accurate and more efficient quantification of ATPase related tissue properties was examined. ATPase encoding was added to the bSSFP-type pulse sequence to simultaneously measure both CK and ATPase related metabolism in the MT-MRF method. Simulation results showed the potential for accurate and significantly more robust measurements for ATPase related metabolism as compared to conventional MT-IR method, while retaining accurate CK related metabolic measurements. Simulation studies showed an approximate ~50% improved coefficient of variation in metabolic rate constant measurement as compared to conventional methods given equal experiment time. These improvements were smaller than those obtained by the CK-MRF method in Chapter 4 for CK metabolism measurement, but were still consistent with our hypothesis. *In vivo*

studies using MT-MRF showed no significant biases in measurements related to ATPase metabolism, and showed smaller variability in measurements as compared to conventional MT-IR. However, this improvement in variability was not significant. The obtained results suggested that in theory, the developed MT-MRF method had the potential to improve measurement efficiency, however both simulation and *in* vivo results suggested the improvements were likely marginal for the assessed experimental conditions.

Several experimental limitations contributed to the difficulty of conclusive investigation. While theoretically, a larger sample size could have been used to confirm the significance of the improvement to measurement robustness, inter-animal physiological variation also contributed to measurement variability. Previously, to mitigate the potential of confounding effect during CK-MRF assessment, a repeated measurement reproducibility study was used to separate these potential effects. However, this study design not feasible to examine MT-MRF due to the limitations of anesthesia duration. Therefore, while *in vivo* were consistent with simulation results, demonstration of improved measurement efficiency was not possible on the available hardware and physiology. Additionally, the 50% improvement predicted by simulation experiments would not have been sufficient to enable robust *in vivo* assessment of potential metabolic perturbations under the restrictions of the available SNR and experimental time limits for rat skeletal muscle.

Overall, the work presented in this thesis represents only the first step in accelerating ^{31}P based measurements of metabolism. The methods presented in this work may be tuned to improve particular aspects of pulse sequence performance. While the improvements to ATPase related metabolic measurements were promising, future development may seek to optimize measurement of CK and ATPase related metabolism by use of separate acquisitions. For instance, CK-MRF could be used to specifically measure the parameters k_f^{CK}, M_R^{PCr}, T_1^{PCr} and ω^{PCr}. These measured parameters could then be used as fixed parameters during the estimation process of a separate acquisition of MT-MRF to estimate k_f^{ATP}, M_R^{Pi}, T_1^{Pi}, and ω^{Pi}. In this way, no compromises would inherently be necessary to the accuracy of any of the measured parameters, and the search space during parameter estimation for any given acquisition is reduced. The disadvantage of this approach is the marginal time necessary to obtain data for two different acquisitions. However, due to the inherently large difference in flux rates of metabolism between CK and ATPase enzymes, and the large number of signal averages likely necessary for any ATPase related measurement, this marginal time cost is small compared to the potential benefits. Furthermore, regardless of the measurement of either CK or ATPase metabolism, the acquisition parameters must be selected with the goals of the application in mind. The pulse sequence parameters selected in the current work were designed for the ^{31}P spin and metabolic parameters of the skeletal muscle in rat leg at 9.4 T. Other applications may require adjustment for other applications or experimental settings.

Future Directions

While further optimizations of the methods developed in the current work may yield marginal improvements to measurement accuracy or robustness, the current methods are already sufficiently optimized to enable the study of previously difficult to observe physiology questions. In this final chapter, preliminary work on two innovative applications using the methods developed in this thesis will be discussed.

Previously, the metabolic response over time to a metabolic insult was difficult to assess. Studies were restricted to single snapshot measurements of a dynamic process due to the time required to perform a measurement. Here we will present a preliminary study that makes use of rapid and repeated measurements to perform continuous monitoring of metabolism with high temporal resolution.

It was also difficult to robustly combine spatial gradients with available MT-MRS methods to perform localization of metabolic rates. Studies desiring spatial localization were restricted to single voxel methods, or averaging across large spatial ROIs. Here we will also present a preliminary study, combining the CK-MRF method with a simple spatial localization scheme, to perform metabolic imaging of the rat leg.

Continuous Monitoring of Metabolism with 20 s Temporal Resolution

One potential use of highly efficient, short acquisitions is the ability to continuously monitor a metabolic process, by performing temporally resolved repeated measurements during a metabolic perturbation. In Chapter 4, the CK-MRF method was able to achieve robust measurement of CK metabolism in 20 seconds. By repeating these CK-MRF measurements, the response of metabolism to a physiological insult such as ischemia may be observed as they occur.

To this end, a study was conducted to assess the potential of the CK-MRF to perform continuous metabolic measurement of rat skeletal muscle during transient ischemia and reperfusion. 14 animals, divided into two groups, underwent two cycles of 17 minute cuff induced ischemia followed by 17 minute reperfusion periods. During each IR cycle, either CK-MRF method measurements, or conventional ^{31}P spectra were repeatedly acquired. Figure 6.1 outlines the acquisition and experimental protocol.

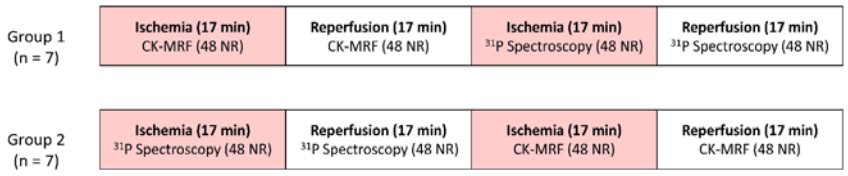

Figure 6.1. Acquisition protocol and timings for continuous metabolism monitoring during ischemia/reperfusion protocol.

For each cycle of IR, either CK-MRF or ^{31}P Spectroscopy was continuously acquired using 20 s temporal resolution. CK-MRF method was performed as described in Chapter 4. ^{31}P spectra were acquired using 55° hard pulse excitation with 2 s TR and 10 signal averages per measurement. This resulted in 48 measurements during each round of ischemia and each round of perfusion by either the CK-MRF or the ^{31}P spectroscopy method. Animals were randomly assigned into two groups (n=7 per group). Depending on the group, CK-MRF used to measure either the first or second cycle of IR, and ^{31}P spectroscopy was used to measure the other.

CK-MRF processing and parameter estimation, described in Chapter 4, quantified each 20 s measurement for PCr-to-ATP metabolite ratio (M_R^{PCr}) and creatine kinase forward rate constant (k_f^{CK}). Each conventional ^{31}P spectra acquired also at 20 s temporal resolution was used to quantify for M_R^{PCr} and intracellular pH. These two properties were used to derive the free intracellular ADP concentration was derived from ^{31}P spectra using the CK equilibrium equation [3]:

$$[ADP] = \left(\frac{TCr}{PCr} - 1\right)\frac{[ATP]K_{eq}}{[H^+]} \qquad [6.1]$$

Where total creatine concentration, TCr, is the sum of creatine and phosphocreatine concentrations, K_{eq} is the CK equilibrium constant, and H^+ is the proton concentration derived from pH value. Values of 43 mM, 8 mM and $5.8\text{x}10^{10}$ for TCr concentration, ATP concentration, and CK equilibrium constants, respectively, were taken from literature [3].

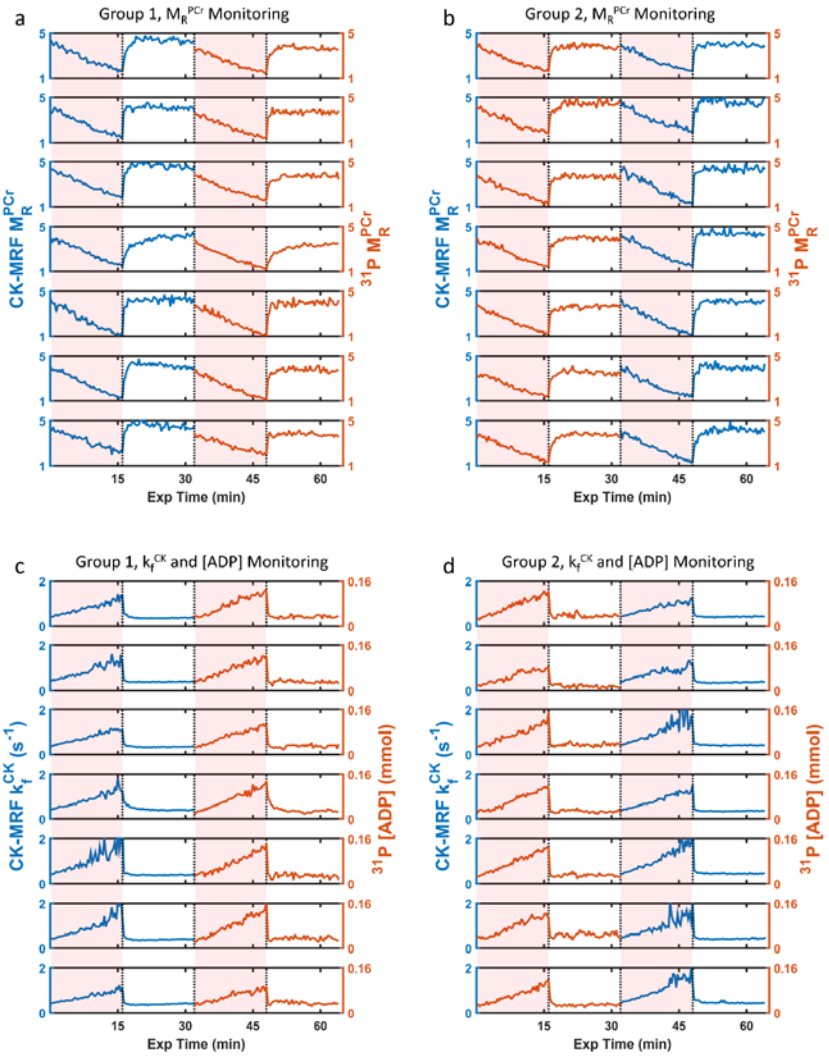
a
Group 1, M_R^{PCr} Monitoring
b
Group 2, M_R^{PCr} Monitoring
CK-MRF M_R^{PCr}
^{31}P M_R^{PCr}
Exp Time (min)
c
Group 1, k_f^{CK} and [ADP] Monitoring
d
Group 2, k_f^{CK} and [ADP] Monitoring
CK-MRF k_f^{CK} (s^{-1})
^{31}P [ADP] (mmol)

Figure 6.2. Measurement traces from each animal during two cycles of ischemia reperfusion. CK-MRF measurements (blue line/axis) and ^{31}P MRS measurements (red line/axis) are shown on the same axis. Ischemia periods are indicated by pink backgrounds. (**a**,**c**) Group 1 animals performed measurements using CK-MRF during first IR cycle and using ^{31}P MRS during the second IR cycle. (**b**,**d**) Group 2 animals performed measurements with ^{31}P MRS during first IR cycle and CK-MRF during the second IR cycle. Measurements are presented for M_R^{PCr} (a and b) and either k_f^{CK} or [ADP] (c and d).

Results from each animal during IR protocol are shown in Figure 6.2. M_R^{PCr} consistently and steadily decreased during ischemia, and rapid restored to baseline during reperfusion. This effect rate and size appeared consistent between both measurement methods and both first and the second cycles of IR. This response is consistent with CK's role in buffering ATP during situations of mismatches between ATP supply and demand. Also observed was a steady increase in [ADP] during ischemia that rapidly restored to baseline during reperfusion. k_f^{CK} response was similar to that of [ADP]. Despite the two measurements being derived from independent methods and signal generation phenomena, this is consistent with the current understanding of CK enzyme regulation[3]. The meaning of these measurements and what they elucidate of the underlying physiological processes are topics of further investigation.

Metabolic Imaging

The ability to perform spatial mapping of metabolism may have many future applications. Even in homogenous skeletal muscle, there is reason to believe that there are regional differences in metabolism. Previously, Parasoglou et. al.

observed differences in human CK metabolic rates in the tibialis anterior muscle compared to other muscles in the calf[41]. Parasoglou et. al. postulated this was a result of different muscle preference for glycolytic vs oxidative metabolism. In rats, muscle preference for glycolytic metabolism has been measured previously, using biochemical methods by Armstrong et. al., and the results of that study are reproduced in Figure 6.3.

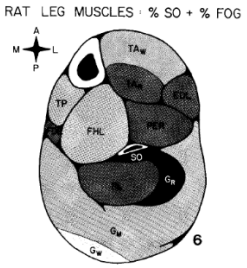

Figure 6.3. Cross sectional anatomical representation of the muscle within a rat leg. The shading in each muscle is proportional to the percent of fibers of high-oxidative type. Figure is reproduced from literature[77].

To assess the possibility of observing regional differences in CK metabolism in the rat leg, a simple gradient imaging approach was added to the CK-MRF method. Within each FID acquisition window of the CK-MRF method, a balanced 2D single-shot spiral-in-spiral-out gradient waveform was added. The implemented trajectory was designed to fully sample an axial imaging slice with 40x40 mm FOV with 2.5 mm resolution. Hyperbolic secant inversion pulses, performed at the end of each saturation block, were added to perform outer volume suppression in the proximal-distal direction of the leg, to result in a 10 mm imaging slab, resulting in

a voxel volume of 62.5 µL. Maps, performed using 480 signal averages requiring a total of 160 minutes, from two rats are presented in Figure 6.4.

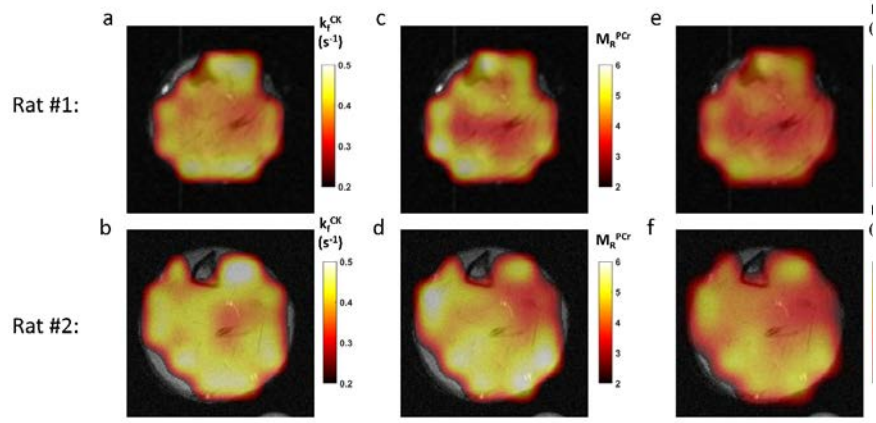

Figure 6.4. CK metabolism maps from the hindlimb of two rats, acquired using a spatially localized CK-MRF method. Maps, superimposed on ^{1}H reference image, are shown for k_f^{CK} (a,b), M_R^{PCr} (c,d), and CK flux (e,f). CK-MRF derived maps were interpolated to the same resolution as ^{1}H reference image.

CK metabolism maps appear to exhibit regional differences consistent across both rats, particular for k_f^{CK}. Interestingly, Parasoglou et. al. measured a significantly lower k_f^{CK} value in the tibialis anterior compared to other muscles. In rats, the opposite trend was observed. This trend reversal is consistent with the difference in oxidative capacity of the tibialis anterior in rodents as compared to humans[78]. These results affirm the potential and utility of metabolic mapping using ^{31}P MRF based methods.

Appendix A: Discrete Two-Pool Bloch-McConnell Simulation

Signal evolutions in response to a pulse sequence for two exchanging metabolite pools were simulated using the Bloch-McConnell equations[14,34]. The matrix form of the Bloch-McConnell equations can be expressed as:

$$\frac{d}{dt}M = AM + C \qquad \text{[A1]}$$

where M is a vector that describes the evolution of the transverse and longitudinal magnetization. For two exchanging species PCr and γATP, M is defined as:

$$M = \left[M_x^{\mathrm{PCr}}\ M_y^{\mathrm{PCr}}\ M_z^{\mathrm{PCr}}\ M_x^{\gamma\mathrm{ATP}}\ M_y^{\gamma\mathrm{ATP}}\ M_z^{\gamma\mathrm{ATP}}\right]^T \qquad \text{[A2]}$$

C is a vector that describes the steady-state magnetization weighted by the longitudinal relaxation, i.e.,

$$C = \left[0\quad 0\quad \frac{M_0^{\mathrm{PCr}}}{T_1^{\mathrm{PCr}}}\quad 0\quad 0\quad \frac{M_0^{\gamma\mathrm{ATP}}}{T_1^{\gamma\mathrm{ATP}}}\right]^T \qquad \text{[A3]}$$

where M_0^{PCr} and $M_0^{\gamma\mathrm{ATP}}$ are the steady-state magnetization and T_1^{PCr} and $T_1^{\gamma\mathrm{ATP}}$ are the longitudinal relaxation time for PCr and γATP, respectively. A is a matrix that describes the precession, relaxation, and magnetization exchange between PCr and γATP. For PCr and γATP with resonance frequencies $\omega^{\mathrm{PCr}}$and $\omega^{\gamma\mathrm{ATP}}$ observed in a rotating frame of frequency ω, A matrix can be expressed as:

$$A = \begin{bmatrix} -\frac{1}{T_2^{\mathrm{PCr}}} - k_f^{\mathrm{CK}} & \Delta\omega^{\mathrm{PCr}} + \Delta\omega_0 & k_r^{\mathrm{CK}} & & & \\ -\Delta\omega^{\mathrm{PCr}} - \Delta\omega_0 & -\frac{1}{T_2^{\mathrm{PCr}}} - k_f^{\mathrm{CK}} & & k_r^{\mathrm{CK}} & & \\ & & -\frac{1}{T_1^{\mathrm{PCr}}} - k_f^{\mathrm{CK}} & & & k_r^{\mathrm{CK}} \\ k_f^{\mathrm{CK}} & & & -\frac{1}{T_2^{\gamma ATP}} - k_r^{CK} & \Delta\omega^{\gamma\mathrm{ATP}} + \Delta\omega_0 & \\ & k_f^{\mathrm{CK}} & & -\Delta\omega^{\gamma\mathrm{ATP}} - \Delta\omega_0 & -\frac{1}{T_2^{\gamma\mathrm{ATP}}} - k_r^{\mathrm{CK}} & \\ & & k_f^{\mathrm{CK}} & & & -\frac{1}{T_1^{\gamma\mathrm{ATP}}} - k_r^{\mathrm{CK}} \end{bmatrix}$$

[A4]

where T_2^{PCr} and $T_2^{\gamma\mathrm{ATP}}$ are the transverse relaxation time of PCr and γATP, respectively. $\Delta\omega^{\mathrm{PCr}}$ and $\Delta\omega^{\gamma\mathrm{ATP}}$ are the difference between the resonance frequency of PCr (ω^{PCr}) and γATP ($\omega^{\gamma\mathrm{ATP}}$) from the frequency of the rotating frame (ω.), i.e., $\Delta\omega^{\mathrm{PCr}} = \omega^{\mathrm{PCr}} - \omega$ and $\Delta\omega^{\gamma\mathrm{ATP}} = \omega^{\gamma\mathrm{ATP}} - \omega$. $\Delta\omega_0$ is the frequency dispersion term used to account for B_0 field inhomogeneity. k_f^{CK} and k_r^{CK} are the forward and reverse exchange rate from PCr to γATP, respectively. Chemical equilibrium was assumed for all simulations such that:

$$k_r^{\mathrm{CK}} = k_f^{\mathrm{CK}} \frac{M_0^{\mathrm{PCr}}}{M_0^{\gamma\mathrm{ATP}}} \qquad [A5]$$

Starting from a fully relaxed spin system, signal evolutions in response to a pulse sequence were simulated by iteratively solving for M in discrete time steps (Δt) using the discrete time solution for Equation A1:

$$M^{N+1} = e^{A\Delta t} M^N + (e^{A\Delta t} - I)A^{-1}C \qquad [A6]$$

where M^N and M^{N+1} are magnetization vectors before and after an iteration.

RF pulses were modeled as discretized instantaneous rotations about the x- and y-axis of the rotating frame:

$$M^+ = R_x(\alpha_x)R_y(\alpha_y)M^- \quad \text{[A7]}$$

where M^- and M^+ are the magnetization vector before and after the RF pulse, and $R_x(\alpha_x)$ and $R_y(\alpha_y)$ are the rotation matrix about the x- and y-axis with flip angles α_x and α_y, respectively, i.e.,

$$R_x(\alpha_x) = \begin{bmatrix} 1 & & & & & \\ & \cos\alpha_x & -\sin\alpha_x & & & \\ & \sin\alpha_x & \cos\alpha_x & & & \\ & & & 1 & & \\ & & & & \cos\alpha_x & -\sin\alpha_x \\ & & & & \sin\alpha_x & \cos\alpha_x \end{bmatrix} \quad \text{[A8]}$$

$$R_y(\alpha_y) = \begin{bmatrix} \cos\alpha_y & & -\sin\alpha_y & & & \\ & 1 & & & & \\ \sin\alpha_y & & \cos\alpha_y & & & \\ & & & \cos\alpha_y & & -\sin\alpha_y \\ & & & & 1 & \\ & & & \sin\alpha_y & & \cos\alpha_y \end{bmatrix} \quad \text{[A9]}$$

Once M is solved, the FID signal, i.e., the transverse magnetization $M_\perp$, was computed as

$$M_\perp = \begin{bmatrix} M_\perp^{\mathrm{PCr}} \\ M_\perp^{\gamma\,\mathrm{ATP}} \end{bmatrix} = \begin{bmatrix} M_x^{\mathrm{PCr}} + iM_y^{\mathrm{PCr}} \\ M_x^{\gamma\,\mathrm{ATP}} + iM_y^{\gamma\,\mathrm{ATP}} \end{bmatrix} \quad \text{[A10]}$$

To account for the effects of B_0 inhomogeneity, simulations were repeated with 51 different values of $\Delta\omega_0$ ranging from -75 to 75 Hz with a uniform resolution of 3 Hz. The total signal, $S(t)$, was calculated as the weighted sum of 51 simulations:

$$S(t) = \sum_{\Delta\omega_0} W(\Delta\omega_0)M_\perp(t, \Delta\omega_0) \quad \text{[A11]}$$

where $W(\Delta\omega_0)$ is the corresponding weight for a frequency component derived from a Lorentzian lineshape with a linewidth LW:

$$W(\Delta\omega_0) = \frac{\mathrm{LW}^2}{(\Delta\omega_0)^2 + \mathrm{LW}^2} \qquad \text{[A12]}$$

Appendix B: Discrete Three-Pool Bloch-McConnell Simulation

Three-pool exchange simulations, involving PCr, γATP, and P_i, were performed by expanding the Bloch-McConnell equations from Appendix A to include the chemical exchange between P_i and ATP:

$$M = \left[M_x^{\mathrm{PCr}}\ M_y^{\mathrm{PCr}}\ M_z^{\mathrm{PCr}}\ M_x^{\gamma\mathrm{ATP}}\ M_y^{\gamma\mathrm{ATP}}\ M_z^{\gamma\mathrm{ATP}}\ M_x^{\mathrm{Pi}}\ M_y^{\mathrm{Pi}}\ M_z^{\mathrm{Pi}}\right]^T \quad \text{[B1]}$$

$$C = \left[0 \quad 0 \quad \frac{M_0^{\mathrm{PCr}}}{T_1^{\mathrm{PCr}}} \quad 0 \quad 0 \quad \frac{M_0^{\gamma\mathrm{ATP}}}{T_1^{\gamma\mathrm{ATP}}} \quad 0 \quad 0 \quad \frac{M_0^{\mathrm{Pi}}}{T_1^{\mathrm{Pi}}}\right]^T \quad \text{[B2]}$$

$$A = \begin{bmatrix}
-\frac{1}{T_2^{PCr}} - k_f^{CK} & \Delta\omega^{PCr} + \Delta\omega_0 & & k_r^{CK} & & & & & \\
-\Delta\omega^{PCr} - \Delta\omega_0 & -\frac{1}{T_2^{PCr}} - k_f^{CK} & & & k_r^{CK} & & & & \\
& & -\frac{1}{T_1^{PCr}} - k_f^{CK} & & & k_r^{CK} & & & \\
k_f^{CK} & & & -\frac{1}{T_2^{\gamma ATP}} - k_r^{CK} - k_r^{Pi} & \Delta\omega^{\gamma ATP} + \Delta\omega_0 & & k_f^{Pi} & & \\
& k_f^{CK} & & -\Delta\omega^{\gamma ATP} - \Delta\omega_0 & -\frac{1}{T_2^{\gamma ATP}} - k_r^{CK} - k_r^{Pi} & & & k_f^{Pi} & \\
& & k_f^{CK} & & & -\frac{1}{T_1^{\gamma ATP}} - k_r^{CK} - k_r^{Pi} & & & k_f^{Pi} \\
& & & k_r^{Pi} & & & -\frac{1}{T_2^{Pi}} - k_f^{Pi} & \Delta\omega^{Pi} + \Delta\omega_0 & \\
& & & & k_r^{Pi} & & \Delta\omega^{Pi} + \Delta\omega_0 & -\frac{1}{T_2^{Pi}} - k_f^{Pi} & \\
& & & & & k_r^{Pi} & & & -\frac{1}{T_1^{Pi}} - k_f^{Pi}
\end{bmatrix} \quad \text{[B3]}$$

where T_1^{Pi} and T_2^{Pi} are the longitudinal and transverse relaxation time constants of P_i, respectively. $\Delta\omega^{\mathrm{Pi}}$ is the difference between the resonance frequency of P_i (ω^{Pi}) and the frequency of the rotating frame (ω). k_f^{Pi} and k_r^{Pi} are the forward and reverse exchange rate from P_i to γATP, respectively. Chemical equilibrium was also assumed such that

$$k_r^{\mathrm{Pi}} = k_f^{\mathrm{Pi}} \frac{M_0^{\mathrm{Pi}}}{M_0^{\gamma\mathrm{ATP}}} \quad \text{[B4]}$$

Appendix C: Discrete Two-Pool Bloch-McConnell Simulation with Continuous Wave RF Selective Saturation

To predict the effects of continuous wave RF saturation pulses during two-pool exchange generated, a rotation term (ω_s) was added to the Bloch-McConnell equations from Appendix A, such that:

$$A = \begin{bmatrix} -\frac{1}{T_2^{PCr}} - k_f^{CK} & \Delta\omega^{PCr} + \Delta\omega_0 & & k_r^{CK} & & \\ -\Delta\omega^{PCr} - \Delta\omega_0 & -\frac{1}{T_2^{PCr}} - k_f^{CK} & \omega_s & & k_r^{CK} & \\ & -\omega_s & -\frac{1}{T_1^{PCr}} - k_f^{CK} & & & k_r^{CK} \\ k_f^{CK} & & & -\frac{1}{T_2^{\gamma ATP}} - k_r^{CK} & \Delta\omega^{\gamma ATP} + \Delta\omega_0 & \\ & k_f^{CK} & & -\Delta\omega^{\gamma ATP} - \Delta\omega_0 & -\frac{1}{T_2^{\gamma ATP}} - k_r^{CK} & \omega_s \\ & & k_f^{CK} & & -\omega_s & -\frac{1}{T_1^{\gamma ATP}} - k_r^{CK} \end{bmatrix} \quad [C1]$$

where ω_s is the Lamor frequency determined by the power (B_1) of the saturation pulse. During the simulation of selective saturation, the frequency of the rotating frame ω was set equal to the carrier frequency of the saturation pulse.

Appendix D: Decoupled Three-Pool Bloch-McConnell Simulation

An alternative method for three-pool Bloch-McConnell simulation was developed to reduce computation time. The evolution of both the Bloch-McConnell equations, previously described in Appendix B in matrix form, can also be expressed as the following equations:

$$\frac{dM_z^{\mathrm{PCr}}(t)}{dt} = \frac{M_0^{\mathrm{PCr}} - M_z^{\mathrm{PCr}}(t)}{T_1^{\mathrm{PCr}}} - k_f^{\mathrm{CK}} M_z^{\mathrm{PCr}}(t) + k_r^{\mathrm{CK}} M_z^{\mathrm{ATP}}(t) \quad [D1]$$

$$\frac{dM_z^{\mathrm{ATP}}(t)}{dt} = \frac{M_0^{\mathrm{ATP}} - M_z^{\mathrm{ATP}}(t)}{T_1^{\mathrm{ATP}}} + k_f^{\mathrm{CK}} M_z^{\mathrm{PCr}}(t) + k_f^{\mathrm{ATP}} M_{z,Pi}(t) - (k_r^{\mathrm{CK}} + k_r^{\mathrm{ATP}}) M_z^{\mathrm{ATP}}(t) \quad [D2]$$

$$\frac{dM_z^{\mathrm{Pi}}(t)}{dt} = \frac{M_0^{\mathrm{Pi}} - M_z^{\mathrm{Pi}}(t)}{T_1^{\mathrm{Pi}}} - k_f^{\mathrm{ATP}} M_z^{\mathrm{Pi}}(t) + k_r^{\mathrm{ATP}} M_z^{\mathrm{ATP}}(t) \quad [D3]$$

where M_0^{X} and T_1^{X} are the equilibrium magnetization and the longitudinal relaxation time of metabolite X, respectively. k_f^{CK} is the forward rate constant of ATP synthesis through creatine kinase, and k_f^{ATP} is the forward rate constant of ATP synthesis from P_i. Finally, k_r^{CK} and k_r^{ATP} are the respective reverse rate constants.

At chemical equilibrium, the forward and reverse reaction rates are related by their corresponding steady-state metabolite concentrations as:

$$k_r^{\mathrm{CK}} = k_f^{\mathrm{CK}} \frac{M_0^{\mathrm{PCr}}}{M_0^{\mathrm{ATP}}} \quad \text{and} \quad k_r^{\mathrm{ATP}} = k_f^{\mathrm{ATP}} \frac{M_0^{\mathrm{Pi}}}{M_0^{\mathrm{ATP}}}$$

Hence, Eqs. D1-3 can be rewritten as:

$$\frac{dM_z^{\mathrm{PCr}}(t)}{dt} = \frac{M_0^{\mathrm{PCr}} - M_z^{\mathrm{PCr}}(t)}{T_1^{\mathrm{PCr}}} - k_f^{\mathrm{CK}} M_0^{\mathrm{PCr}} \left[\frac{M_z^{\mathrm{PCr}}(t)}{M_0^{\mathrm{PCr}}} - \frac{M_z^{\mathrm{ATP}}(t)}{M_0^{\mathrm{ATP}}}\right] \quad [D4]$$

$$\frac{dM_z^{\mathrm{ATP}}(t)}{dt} = \frac{M_0^{\mathrm{ATP}} - M_z^{\mathrm{ATP}}(t)}{T_1^{\mathrm{ATP}}} + k_f^{\mathrm{CK}}\, M_0^{\mathrm{PCr}} \left[\frac{M_z^{\mathrm{PCr}}(t)}{M_0^{\mathrm{PCr}}} - \frac{M_z^{\mathrm{ATP}}(t)}{M_0^{\mathrm{ATP}}}\right] + k_f^{\mathrm{ATP}}\, M_0^{\mathrm{Pi}} \left[\frac{M_z^{\mathrm{Pi}}(t)}{M_0^{\mathrm{Pi}}} - \frac{M_z^{\mathrm{ATP}}(t)}{M_0^{\mathrm{ATP}}}\right] \quad [D5]$$

$$\frac{dM_z^{\mathrm{Pi}}(t)}{dt} = \frac{M_0^{\mathrm{Pi}} - M_z^{\mathrm{Pi}}(t)}{T_1^{\mathrm{Pi}}} - k_f^{\mathrm{ATP}}\, M_0^{\mathrm{Pi}} \left[\frac{M_z^{\mathrm{Pi}}(t)}{M_0^{\mathrm{Pi}}} - \frac{M_z^{\mathrm{ATP}}(t)}{M_0^{\mathrm{ATP}}}\right] \quad [D6]$$

Eqs. D4-6 can be simplified by expressing $M_z^{\mathrm{PCr}}(t)$, $M_z^{\mathrm{ATP}}(t)$, and $M_z^{\mathrm{Pi}}(t)$ in their corresponding M_0-normalized forms:

$$\frac{dM_z^{\mathrm{PCr}}(t)}{dt} = \frac{1 - M_z^{\mathrm{PCr}}(t)}{T_1^{\mathrm{PCr}}} - k_f^{\mathrm{CK}}[M_z^{\mathrm{PCr}}(t) - M_z^{\mathrm{ATP}}(t) \quad [D7]$$

$$\frac{dM_z^{\mathrm{ATP}}(t)}{dt} = \frac{1 - M_z^{\mathrm{ATP}}(t)}{T_1^{\mathrm{ATP}}} + k_f^{\mathrm{CK}}\, M_R^{\mathrm{PCr}} \left[M_z^{\mathrm{PCr}}(t) - M_z^{\mathrm{ATP}}(t)\right] + k_f^{\mathrm{ATP}}\, M_R^{\mathrm{Pi}}[M_z^{\mathrm{Pi}}(t) - M_z^{\mathrm{ATP}}(t)] \quad [D8]$$

$$\frac{dM_z^{\mathrm{Pi}}(t)}{dt} = \frac{1 - M_z^{\mathrm{Pi}}(t)}{T_1^{\mathrm{Pi}}} - k_f^{\mathrm{ATP}}[M_z^{\mathrm{Pi}}(t) - M_z^{\mathrm{ATP}}(t)] \quad [D9]$$

Note that $M_z^{\mathrm{X}}(t)$ in Eqs. D7-9 is the magnetization of a metabolite at time t, normalized by its equilibrium magnetization M_0^{X}. M_R^{PCr} and M_R^{Pi} are the ratios of M_0^{PCr} to M_0^{ATP}, and M_0^{Pi} to M_0^{ATP}, respectively.

The evolution of the M_0–normalized transverse magnetization, $M_\perp^{\mathrm{PCr}}(t)$, $M_\perp^{\mathrm{ATP}}(t)$, and $M_\perp^{\mathrm{Pi}}(t)$, can be derived in a similar way:

$$\frac{dM_\perp^{\mathrm{PCr}}(t)}{dt} = -\left(\frac{1}{T_2^{\mathrm{PCr}}} - i\omega^{\mathrm{PCr}}\right) M_\perp^{\mathrm{PCr}}(t) - k_f^{\mathrm{CK}}[M_\perp^{\mathrm{PCr}}(t) - M_\perp^{\mathrm{ATP}}(t)] \quad [D10]$$

$$\frac{dM_\perp^{\mathrm{ATP}}(t)}{dt} = -\left(\frac{1}{T_2^{\mathrm{ATP}}} - i\omega^{\mathrm{ATP}}\right) M_\perp^{\mathrm{ATP}}(t) + k_f^{\mathrm{CK}}\, M_R^{\mathrm{PCr}} \left[M_\perp^{\mathrm{PCr}}(t) - M_\perp^{\mathrm{ATP}}(t)\right] + k_f^{\mathrm{ATP}} M_R^{\mathrm{Pi}} \left[M_\perp^{\mathrm{Pi}}(t) - M_\perp^{\mathrm{ATP}}(t)\right] \quad [D11]$$

$$\frac{dM_{\perp,Pi}}{dt} = -\left(\frac{1}{T_2^{\mathrm{Pi}}} - i\omega^{\mathrm{Pi}}\right) M_\perp^{\mathrm{Pi}}(t) - k_f^{\mathrm{ATP}} \left[M_\perp^{\mathrm{Pi}}(t) - M_\perp^{\mathrm{ATP}}(t)\right] \quad [D12]$$

where T_2^{X} and ω^{X} are the transverse relaxation time and resonance frequency (chemical shift) of metabolite X, respectively.

Bibliography

1. Dutta P, Martinez G V, Gillies RJ. A New Horizon of DNP technology: Application to In-vivo (13)C Magnetic Resonance Spectroscopy and Imaging. *Biophys Rev*. 2013;5(3):271-281. doi:10.1007/s12551-012-0099-2.
2. Lu M, Zhang Y, Ugurbil K, Chen W, Zhu X-H. In vitro and in vivo studies of 17O NMR sensitivity at 9.4 and 16.4 T. *Magn Reson Med*. 2013;69(6):1523-1527. doi:10.1002/mrm.24386.
3. Kemp GJ, Ahmad RE, Nicolay K, Prompers JJ. Quantification of skeletal muscle mitochondrial function by 31P magnetic resonance spectroscopy techniques: a quantitative review. *Acta Physiol (Oxf)*. 2015;213(1):107-144. doi:10.1111/apha.12307.
4. Wu F, Zhang EY, Zhang J, Bache RJ, Beard DA. Phosphate metabolite concentrations and ATP hydrolysis potential in normal and ischaemic hearts. *J Physiol*. 2008;586(17):4193-4208. doi:10.1113/jphysiol.2008.154732.
5. Neubauer S, Horn M, Cramer M, et al. Myocardial phosphocreatine-to-ATP ratio is a predictor of mortality in patients with dilated cardiomyopathy. *Circulation*. 1997;96(7):2190-2196. http://www.ncbi.nlm.nih.gov/pubmed/9337189.
6. Ma D, Gulani V, Seiberlich N, et al. Magnetic resonance fingerprinting. *Nature*. 2013;495(7440):187-192. doi:10.1038/nature11971.
7. Jiang Y, Ma D, Seiberlich N, Gulani V, Griswold M a. MR fingerprinting using fast imaging with steady state precession (FISP) with spiral readout. *Magn Reson Med*. 2015;74(6):1621-1631. doi:10.1002/mrm.25559.
8. Chen Y, Jiang Y, Pahwa S, et al. MR Fingerprinting for Rapid Quantitative Abdominal Imaging. *Radiology*. 2016;279(1):278-286. doi:10.1148/radiol.2016152037.
9. Hamilton JI, Jiang Y, Chen Y, et al. MR fingerprinting for rapid quantification of myocardial T1, T2, and proton spin density. *Magn Reson Med*. 2016;0. doi:10.1002/mrm.26216.
10. Horn M. Cardiac magnetic resonance spectroscopy: a window for studying physiology. *Methods Mol Med*. 2006;124:225-248. http://www.ncbi.nlm.nih.gov/pubmed/16506424.
11. Martin WRW. MR spectroscopy in neurodegenerative disease. *Mol Imaging Biol*. 2007;9(4):196-203. doi:10.1007/s11307-007-0087-2.
12. Perry CGR, Kane DA, Lanza IR, Neufer PD. Methods for assessing mitochondrial function in diabetes. *Diabetes*. 2013;62(4):1041-1053. doi:10.2337/db12-1219.
13. Ingwall JS. Phosphorus nuclear magnetic resonance spectroscopy of

cardiac and skeletal muscles. *Am J Physiol*. 1982;242(5):H729-44.

14. Bottomley PA, Ouwerkerk R, Lee RF, Weiss RG. Four-angle saturation transfer (FAST) method for measuring creatine kinase reaction rates in vivo. *Magn Reson Med*. 2002;47(5):850-863. doi:10.1002/mrm.10130.

15. Lu M, Chen W, Zhu X. Field dependence study of in vivo brain (31) P MRS up to 16.4 T. *NMR Biomed*. 2014;27(9):1135-1141. doi:10.1002/nbm.3167.

16. Xiong Q, Du F, Zhu X, et al. ATP production rate via creatine kinase or ATP synthase in vivo: a novel superfast magnetization saturation transfer method. *Circ Res*. 2011;108(6):653-663. doi:10.1161/CIRCRESAHA.110.231456.

17. Bieri O, Scheffler K. Fundamentals of balanced steady state free precession MRI. *J Magn Reson Imaging*. 2013;38(1):2-11. doi:10.1002/jmri.24163.

18. Harris FJ. On the use of windows for harmonic analysis with the discrete Fourier transform. *Proc IEEE*. 1978;66(1):51-83. doi:10.1109/PROC.1978.10837.

19. El-Sharkawy A-MM, Gabr RE, Schär M, Weiss RG, Bottomley PA. Quantification of human high-energy phosphate metabolite concentrations at 3 T with partial volume and sensitivity corrections. *NMR Biomed*. 2013;26(11):1363-1371. doi:10.1002/nbm.2961.

20. Gabr RE, Ouwerkerk R, Bottomley P a. Quantifying in vivo MR spectra with circles. *J Magn Reson*. 2006;179(1):152-163. doi:10.1016/j.jmr.2005.11.004.

21. Makhoul J. Linear prediction: A tutorial review. *Proc IEEE*. 1975;63(4):561-580. doi:10.1109/PROC.1975.9792.

22. Koehl P. Linear prediction spectral analysis of NMR data. *Prog NMR Spectrosc*. 1999;34:257-299.

23. Leibfritz D, Dreher W. Magnetization transfer MRS. *NMR Biomed*. 2001;14(2):65-76. doi:10.1002/nbm.681.

24. Befroy DE, Rothman DL, Petersen KF, Shulman GI. ^{31}P-magnetization transfer magnetic resonance spectroscopy measurements of in vivo metabolism. *Diabetes*. 2012;61(11):2669-2678. doi:10.2337/db12-0558.

25. Balaban RS, Kantor HL, Ferretti JA. In vivo flux between phosphocreatine and adenosine triphosphate determined by two-dimensional phosphorous NMR. *J Biol Chem*. 1983;258(21):12787-12789. http://www.ncbi.nlm.nih.gov/pubmed/6630206.

26. Kingsley-Hickman PB, Sako EY, Mohanakrishnan P, et al. 31P NMR studies of ATP synthesis and hydrolysis kinetics in the intact myocardium. *Biochemistry*. 1987;26(23):7501-7510. http://www.ncbi.nlm.nih.gov/pubmed/3427090.

27. Robitaille PM, Merkle H, Sako E, et al. Measurement of ATP synthesis rates by 31P-NMR spectroscopy in the intact myocardium in vivo. *Magn Reson Med*. 1990;15(1):8-24. http://www.ncbi.nlm.nih.gov/pubmed/2374502.

28. Kingsley-Hickman PB, Sako EY, Uğurbil K, From AH, Foker JE. 31P NMR measurement of mitochondrial uncoupling in isolated rat hearts. *J Biol Chem*. 1990;265(3):1545-1550. http://www.ncbi.nlm.nih.gov/pubmed/2136855.

29. Lei H, Zhu X, Zhang X, Ugurbil K, Chen W. In vivo 31P magnetic resonance spectroscopy of human brain at 7 T: an initial experience. *Magn Reson Med*. 2003;49(2):199-205. doi:10.1002/mrm.10379.

30. Schär M, El-Sharkawy A-MM, Weiss RG, Bottomley PA. Triple repetition time saturation transfer (TRiST) 31P spectroscopy for measuring human creatine kinase reaction kinetics. *Magn Reson Med*. 2010;63(6):1493-1501. doi:10.1002/mrm.22347.

31. Schär M, Gabr RE, El-Sharkawy A-MM, Steinberg A, Bottomley PA, Weiss RG. Two repetition time saturation transfer (TwiST) with spill-over correction to measure creatine kinase reaction rates in human hearts. *J Cardiovasc Magn Reson*. 2015;17(1):70. doi:10.1186/s12968-015-0175-4.

32. Speck O, Scheffler K, Hennig J. Fast 31P chemical shift imaging using SSFP methods. *Magn Reson Med*. 2002;48(4):633-639. doi:10.1002/mrm.10279.

33. Deshpande VS, Chung Y-C, Zhang Q, Shea SM, Li D. Reduction of transient signal oscillations in true-FISP using a linear flip angle series magnetization preparation. *Magn Reson Med*. 2003;49(1):151-157. doi:10.1002/mrm.10337.

34. Deoni SCL, Rutt BK, Jones DK. Investigating exchange and multicomponent relaxation in fully-balanced steady-state free precession imaging. *J Magn Reson Imaging*. 2008;27(6):1421-1429. doi:10.1002/jmri.21079.

35. Nabuurs C, Huijbregts B, Wieringa B, Hilbers CW, Heerschap A. 31P saturation transfer spectroscopy predicts differential intracellular macromolecular association of ATP and ADP in skeletal muscle. *J Biol Chem*. 2010;285(51):39588-39596. doi:10.1074/jbc.M110.164665.

36. Ren J, Yang B, Sherry a. D, Malloy CR. Exchange kinetics by inversion transfer: integrated analysis of the phosphorus metabolite kinetic exchanges in resting human skeletal muscle at 7 T. *Magn Reson Med*. 2015;73(4):1359-1369. doi:10.1002/mrm.25256.

37. Bashir A, Gropler R. Reproducibility of creatine kinase reaction kinetics in human heart: a (31) P time-dependent saturation transfer spectroscopy study. *NMR Biomed*. 2014;27(6):663-671. doi:10.1002/nbm.3103.

38. Kingsley PB, Monahan WG. Corrections for off-resonance effects and incomplete saturation in conventional (two-site) saturation-transfer kinetic

measurements. *Magn Reson Med*. 2000;43(6):810-819. doi:10.1002/1522-2594(200006)43:6<810::AID-MRM6>3.0.CO;2-J.

39. Liu Y, Mei X, Li J, Lai N, Yu X. Mitochondrial function assessed by 31P MRS and BOLD MRI in non-obese type 2 diabetic rats. *Physiol Rep*. 2016;4(15):e12890. doi:10.14814/phy2.12890.

40. van den Broek NM, Ciapaite J, Nicolay K, Prompers JJ. Comparison of in vivo postexercise phosphocreatine recovery and resting ATP synthesis flux for the assessment of skeletal muscle mitochondrial function. *AJP Cell Physiol*. 2010;299(5):C1136-C1143. doi:10.1152/ajpcell.00200.2010.

41. Parasoglou P, Xia D, Chang G, Convit A, Regatte RR. Three-dimensional mapping of the creatine kinase enzyme reaction rate in muscles of the lower leg. *NMR Biomed*. 2013;26(9):1142-1151. doi:10.1002/nbm.2928.

42. Shoubridge EA, Bland JL, Radda GK. Regulation of creatine kinase during steady-state isometric twitch contraction in rat skeletal muscle. *BBA - Mol Cell Res*. 1984;805(1):72-78. doi:10.1016/0167-4889(84)90038-7.

43. Pang CY, Neligan P, Xu H, et al. Role of ATP-sensitive K+ channels in ischemic preconditioning of skeletal muscle against infarction. *Am J Physiol*. 1997;273(1 Pt 2):H44-51. http://www.ncbi.nlm.nih.gov/pubmed/9249473.

44. McFarland EW, Kushmerick MJ, Moerland TS. Activity of creatine kinase in a contracting mammalian muscle of uniform fiber type. *Biophys J*. 1994;67(5):1912-1924. doi:10.1016/S0006-3495(94)80674-5.

45. Morrison JF, Cleland WW. Isotope exchange studies of the mechanism of the reaction catalyzed by adenosine triphosphate: creatine phosphotransferase. *J Biol Chem*. 1966;241(3):673-683. http://www.ncbi.nlm.nih.gov/pubmed/5908134.

46. Schimerlik MI, Cleland WW. Inhibition of creatine kinase by chromium nucleotides. *J Biol Chem*. 1973;248(24):8418-8423. http://www.ncbi.nlm.nih.gov/pubmed/4797017.

47. Neubauer S, Hamman BL, Perry SB, Bittl JA, Ingwall JS. Velocity of the creatine kinase reaction decreases in postischemic myocardium: a 31P-NMR magnetization transfer study of the isolated ferret heart. *Circ Res*. 1988;63(1):1-15. doi:10.1161/01.RES.63.1.1.

48. Bittl JA, Balschi JA, Ingwall JS. Contractile failure and high-energy phosphate turnover during hypoxia: 31P-NMR surface coil studies in living rat. *Circ Res*. 1987;60(6):871-878. http://www.ncbi.nlm.nih.gov/pubmed/2954720.

49. Bogner W, Chmelik M, Schmid AI, Moser E, Trattnig S, Gruber S. Assessment of (31)P relaxation times in the human calf muscle: a comparison between 3 T and 7 T in vivo. *Magn Reson Med*. 2009;62(3):574-582. doi:10.1002/mrm.22057.

50. Kingsley PB, Monahan WG. Correcting for Incomplete Saturation and Off-Resonance Effects in Multiple-Site Saturation-Transfer Kinetic Measurements. *J Magn Reson*. 2000;146(1):100-109. doi:10.1006/jmre.2000.2124.

51. Luo Y, de Graaf RA, DelaBarre L, Tannús A, Garwood M. BISTRO: an outer-volume suppression method that tolerates RF field inhomogeneity. *Magn Reson Med*. 2001;45(6):1095-1102. http://www.ncbi.nlm.nih.gov/pubmed/11378888.

52. Balaban RS, Koretsky AP. Interpretation of ^{31}P NMR saturation transfer experiments: what you can't see might confuse you. Focus on "Standard magnetic resonance-based measurements of the Pi→ATP rate do not index the rate of oxidative phosphorylation in cardiac and skeletal muscles. *Am J Physiol Cell Physiol*. 2011;301(1):C12-5. doi:10.1152/ajpcell.00100.2011.

53. Xiong Q, Li Q, Mansoor A, et al. Novel strategy for measuring creatine kinase reaction rate in the in vivo heart. *Am J Physiol Heart Circ Physiol*. 2009;297(3):H1010-9. doi:10.1152/ajpheart.01195.2008.

54. Brown TR, Ugurbil K, Shulman RG. 31P nuclear magnetic resonance measurements of ATPase kinetics in aerobic Escherichia coli cells. *Proc Natl Acad Sci U S A*. 1977;74(12):5551-5553.

55. Alger JR, den Hollander JA, Shulman RG. In vivo phosphorus-31 nuclear magnetic resonance saturation transfer studies of adenosinetriphosphatase kinetics in Saccharomyces cerevisiae. *Biochemistry*. 1982;21(12):2957-2963.

56. Matthews PM, Bland JL, Gadian DG, Radda GK. The steady-state rate of ATP synthesis in the perfused rat heart measured by 31P NMR saturation transfer. *Biochem Biophys Res Commun*. 1981;103(3):1052-1059.

57. Degani H, Laughlin M, Campbell S, Shulman RG. Kinetics of creatine kinase in heart: a 31P NMR saturation- and inversion-transfer study. *Biochemistry*. 1985;24(20):5510-5516.

58. Thoma WJ, Uğurbil K. Saturation-transfer studies of ATP-Pi exchange in isolated perfused rat liver. *Biochim Biophys Acta*. 1987;893(2):225-231.

59. Shoubridge EA, Briggs RW, Radda GK. 31p NMR saturation transfer measurements of the steady state rates of creatine kinase and ATP synthetase in the rat brain. *FEBS Lett*. 1982;140(2):289-292.

60. Brindle KM, Blackledge MJ, Challiss RA, Radda GK. 31P NMR magnetization-transfer measurements of ATP turnover during steady-state isometric muscle contraction in the rat hind limb in vivo. *Biochemistry*. 1989;28(11):4887-4893. doi:10.1021/bi00437a054.

61. Portman MA. Measurement of unidirectional P(i)-->ATP flux in lamb myocardium in vivo. *Biochim Biophys Acta*. 1994;1185(2):221-227.

62. Jucker BM, Ren J, Dufour S, et al. 13C/31P NMR assessment of mitochondrial energy coupling in skeletal muscle of awake fed and fasted rats. Relationship with uncoupling protein 3 expression. *J Biol Chem*. 2000;275(50):39279-39286. doi:10.1074/jbc.M007760200.

63. Choi CS, Befroy DE, Codella R, et al. Paradoxical effects of increased expression of PGC-1alpha on muscle mitochondrial function and insulin-stimulated muscle glucose metabolism. *Proc Natl Acad Sci U S A*. 2008;105(50):19926-19931. doi:10.1073/pnas.0810339105.

64. Lebon V, Dufour S, Petersen KF, et al. Effect of triiodothyronine on mitochondrial energy coupling in human skeletal muscle. *J Clin Invest*. 2001;108(5):733-737. doi:10.1172/JCI11775.

65. Petersen KF, Befroy D, Dufour S, et al. Mitochondrial dysfunction in the elderly: possible role in insulin resistance. *Science*. 2003;300(5622):1140-1142. doi:10.1126/science.1082889.

66. Petersen KF, Dufour S, Befroy D, Garcia R, Shulman GI. Impaired mitochondrial activity in the insulin-resistant offspring of patients with type 2 diabetes. *N Engl J Med*. 2004;350(7):664-671. doi:10.1056/NEJMoa031314.

67. Befroy DE, Petersen KF, Dufour S, et al. Impaired mitochondrial substrate oxidation in muscle of insulin-resistant offspring of type 2 diabetic patients. *Diabetes*. 2007;56(5):1376-1381. doi:10.2337/db06-0783.

68. Befroy DE, Petersen KF, Dufour S, Mason GF, Rothman DL, Shulman GI. Increased substrate oxidation and mitochondrial uncoupling in skeletal muscle of endurance-trained individuals. *Proc Natl Acad Sci U S A*. 2008;105(43):16701-16706. doi:10.1073/pnas.0808889105.

69. Chen&Ugurbil-CKActivation-MRM97.pdf.

70. Lei H, Ugurbil K, Chen W. Measurement of unidirectional P i to ATP flux in human visual cortex at 7 T by using in vivo P magnetic resonance spectroscopy. 2003;100(24).

71. Schär M, El-Sharkawy A-MM, Weiss RG, Bottomley PA. Triple repetition time saturation transfer (TRiST) 31P spectroscopy for measuring human creatine kinase reaction kinetics. *Magn Reson Med*. 2010;63(6):1493-1501. doi:10.1002/mrm.22347.

72. Kemp GJ, Brindle KM. What do magnetic resonance-based measurements of Pi→ATP flux tell us about skeletal muscle metabolism? *Diabetes*. 2012;61(8):1927-1934. doi:10.2337/db11-1725.

73. Yerby B, Deacon R, Beaulieu V, Liang J, Gao J, Laurent D. Insulin-stimulated mitochondrial adenosine triphosphate synthesis is blunted in skeletal muscles of high-fat-fed rats. *Metabolism*. 2008;57(11):1584-1590. doi:10.1016/j.metabol.2008.06.015.

74. Bresnen A, Duong TQ. Brain high-energy phosphates and creatine kinase

synthesis rate under graded isoflurane anesthesia: An in vivo 31 P magnetization transfer study at 11.7 tesla. *Magn Reson Med*. 2015;73(2):726-730. doi:10.1002/mrm.25136.

75. Buonincontri G, Sawiak S. Three-dimensional MR fingerprinting with simultaneous B1 estimation. *MRM_submitted*. 2015;0:1-9. doi:10.1002/mrm.26009.

76. Kingsley PB, Monahan WG. Effects of Off-Resonance Irradiation, Cross-Relaxation, and Chemical Exchange on Steady-State Magnetization and Effective Spin–Lattice Relaxation Times. *J Magn Reson*. 2000;143(2):360-375. doi:10.1006/jmre.2000.2018.

77. Armstrong RB, Phelps RO. Muscle fiber type composition of the rat hindlimb. *Am J Anat*. 1984;171(3):259-272. doi:10.1002/aja.1001710303.

78. Johnson MA, Polgar J, Weightman D, Appleton D. Data on the distribution of fibre types in thirty-six human muscles. An autopsy study. *J Neurol Sci*. 1973;18(1):111-129. doi:10.1016/0022-510X(73)90023-3.